UNIVERSITY OF ÇUKUROVA
INSTITUTE OF NATURAL AND APPLIED SCIENCES

PhD THESIS

Mehmet VERGİLİ

SEACRH FOR DARK MATTER AND LARGE EXTRA DIMENSIONS IN MONOJET EVENTS IN pp COLLISIONS AT $\sqrt{s}$=7 TeV

DEPARTMENT OF PHYSICS

ADANA, 2012

UNIVERSITY OF ÇUKUROVA
INSTITUTE OF NATURAL AND APPLIED SCIENCES

SEACRH FOR DARK MATTER AND LARGE EXTRA DIMENSIONS IN MONOJET EVENTS IN pp COLLISIONS AT $\sqrt{s}$=7 TeV

Mehmet VERGİLİ

PhD THESIS

DEPARTMENT OF PHYSICS

We certify that the thesis titled above was reviewed and approved for the award of degree of the PhD of Science by the board of jury on ../../....

....	....	....
Prof.İsa DUMANOĞLU	Prof. Eda EŞKUT	Prof.Aysel Kayış TOPAKSU
ADVISOR	MEMBER	MEMBER

....	....
Prof. Sefa ERTÜRK	Assist. Prof. Bayram TALİ
MEMBER	MEMBER

This PhD Thesis is performed in Physics Department of the Institute of Natural and Applied Science of Cukurova University
Registration Number:

Prof. Selahattin SERİN
Director
The Institute of Natural and Applied Science

To my Daughter Zeynep

ABSTRACT

PhD THESIS

SEACRH FOR DARK MATTER AND LARGE EXTRA DIMENSIONS IN MONOJET EVENTS IN pp COLLISIONS AT $\sqrt{s}$=7 TeV

Mehmet VERGİLİ

DEPARTMENT OF PHYSICS
INSTITUTE OF NATURAL AND APPLIED SCIENCES
UNIVERSITY OF ÇUKUROVA

Supervisor: Prof. İsa DUMANOĞLU
Year: 2012, Pages: 100
Jury: Prof. İsa DUMANOĞLU
Prof. Eda EŞKUT
Prof. Aysel KAYIŞ TOPAKSU
Prof. Sefa ERTÜRK
Assist. Prof. Bayram TALİ

A search has been made for events containing an energetic jet and an imbalance in transverse momentum using a data sample of pp collisions at a center-of-mass energy of 7 TeV. This signature is common to both dark matter and extra dimensions models. The data were collected by the CMS detector at the LHC and correspond to an integrated luminosity of 5.0 fb^{-1} . The number of observed events is consistent with the standard model expectation. Constraints on the dark matter-nucleon scattering cross sections are determined for both spin-independent and spin-dependent interaction models. For the spin-independent model, these are the most constraining limits for a dark matter particle with mass below 3.5 GeV/c^2, a region unexplored by direct detection experiments. For the spin-dependent model, these are the most stringent constraints over the 0.1–200 GeV/c^2 mass range. The constraints on the Arkani-Hamed, Dimopoulos, and Dvali (ADD) model parameter M_D determined as a function of the number of extra dimensions are also an improvement over the previous results.

Key Words: Dark Matter, Extra Dimension, ADD Model, LHC, CMS, Mono-Jet.

ÖZ

DOKTORA TEZİ

$\sqrt{s}$=7 TeV pp CARPIŞMASINDA TEK-JET OLAYLARINDA KARANLIK MADDE VE EKSTRA BOYUT ARAŞTIRMALARI

Mehmet VERGİLİ

ÇUKUROVA ÜNİVERSİTESİ
FEN BİLİMLERİ ENSTİTÜSÜ
FİZİK BÖLÜMÜ

Danışman: Prof. İsa DUMANOĞLU
Yıl: 2012, Sayfa: 100
Jüri: Prof. İsa DUMANOĞLU
Prof. Eda EŞKUT
Prof. Aysel KAYIŞ TOPAKSU
Prof. Sefa ERTÜRK
Assist. Prof. Bayram TALİ

Bu tezde 7 TeV kütle merkezi enerjisinde pp çarpışmalarından alınan veri ile yüksek enerjili bir jet ve bunu dengeleyen dik momentum içeren olaylar araştırılmıştır. Karanlık madde ve extra boyut araştırmalarında bu tür olaylar beklenmektedir. Araştırma yapılırken kullanılan veri LHC deneyindeki CMS dedektöründen alınmıştır ve toplam ışıklılık değeri 5.0 fb^{-1}'dır. Gözlemlenen olay sayısı Standart Model'den beklenen zemin ile uyum içerisindedir. Karanlık madde araştırmasında karanlık maddenin nükleon ile etkileşim tesir kesiti spin bağımlı ve spin bağımsız durumlar için ayrı ayrı incelenmiştir. Spin bağımsız durum, karanlık madde kütlesinin 3.5 GeV/c^2'den küçük olduğu zaman şu ana kadar yapılmış bütün deneylerden daha iyi sonuç vermiştir. Spin bağımlı durum için ise karanlık madde kütlesi için 0.1-200 GeV/c^2 aralığında bulunan sonuç bütün deneylerden daha iyidir. Extra boyut araştırmalarında Arkani-Hamed, Dimopoulos ve Dvali'nin önerdiği ADD model, M_D parametresi ekstra boyut sayısının fonksiyonu olarak incelenmiş ve bulunan sonuçlar CMS'in daha onceki sonuçlarını geliştirmiştir.

Anahtar Kelimeler: Karanlık Madde, Eksta Boyut, ADD Model, LHC, CMS, Tek-Jet.

ACKNOWLEDGEMENTS

I wish to thank my advisor, İsa DUMANOĞLU, for his encouragement and guidance during my PhD. program.

I sincerely thank my thesis committee Eda EŞKUT, Aysel Kayış TOPAKSU, Sefa ERTÜRK, Bayram TALİ for their precious suggestions.

I thank the mono-jet group members especially Suichi KUNORI, Steven WORM, and Anwar BHATTI for their suggestions.

Finally I thank my dear family for their love.

CONTENTS **PAGE**

LIST OF TABLES **PAGE**

LIST OF FIGURES **PAGE**

ABBREVIATIONS

ADC : Analog Digital Converter

ADD Model : Arkani-Hamed Dimopoulos Dvali’s Model

ALEPH : Apparatus for LEP Physics

ALICE : A Large Ion Collider Experiment

ATLAS : A Toroidal LHC ApparatuS

CDF : Collider Detector at Fermilab

CERN : Conceil Europeenne pour la Recherche Nucleaire

CMS : Compact Muon Solenoid

CSC : Cathode Strip Chambers

DAQ : Data Acqusition

DELPHI : Detector with Lepton, Photon and Hadron Identification

DT : Drift Tube

EB : Electromagnetic Barrel

EE : Electromagnetic Endcap

ECAL : Electromagnetic Calorimeter

HB : Hadronic Barrel

HE : Hadronic Endcap

HF : Hadronic Forward

HCAL : Hadronic Calorimeter JES : Jet Energy Scale

KK : Kaluza-Klein

L3 : High Energy Physics Experiment at the LEP collider

LED : Large Extra Dimension

LEP : Large Electron Positron Collider

LHC : Large Hadron Collider

LHC-b : Large Hadron Collider Beauty Experiment

MVA : Multi Variate Analysis

PS : Proton Synchrotron

1. LHC MACHINE AND CMS DETECTOR

The Large Hadron Collider (LHC) is the world's largest, most powerful particle accelerator. Since the LHC have collisions of such high energy, the hope is that it will solve the most fundamental questions of physics and advance the understanding of the deepest laws of nature. Any results from the LHC collisions should have a major impact on our understanding of physics, either confirming or refuting the projections from the Standard Model of particle physics.

The LHC has been built at CERN (European Organization for Nuclear Research) in the already existent 27 km circular LEP (Large Electron Proton Collider) tunnel. It provides the highest energy ever explored with particle accelerators. This synchrotron is designed to collide opposing particle beams of protons at an energy of 7 teraelectronvolts (7 TeV or 1.12 microjoules) per particle, or lead nuclei at an energy of 574 TeV (92.0 microjoules) per nucleus.

The protons acceleration are starting a small linear accelerator then protons are transfering to PS (Positron Synchrotron). PS accelerate the protons up to 26 GeV then transver to SPS (Super Positron Synchrotron). SPS accelerate the protons up to 450 GeV and finally transfer the LHC (Figure 1.1). One of the critical aspects in accelerating the protons up to an energy of 7 TeV is the required bending magnetic field which, for the LHC bending radius (R $\sim$ 2780 m) is about 8.4 T. 1232 LHC superconducting 14.2 m long dipole magnets will create this magnetic field; they are placed in the eight curved sections which connect the straight sections of the LHC ring. The super-conducting magnets use a Ni-Ti conductor, cooled down to 1.9 K by means of super-fluid Helium. (BAYATIAN, 2006)

1.1 The CMS Detector

The Compact Muon Solenoid (CMS) experiment uses a general-purpose detector to investigate a wide range of physics, including the search for the Higgs boson, extra dimensions, and particles that could make up dark matter. Detectors built on

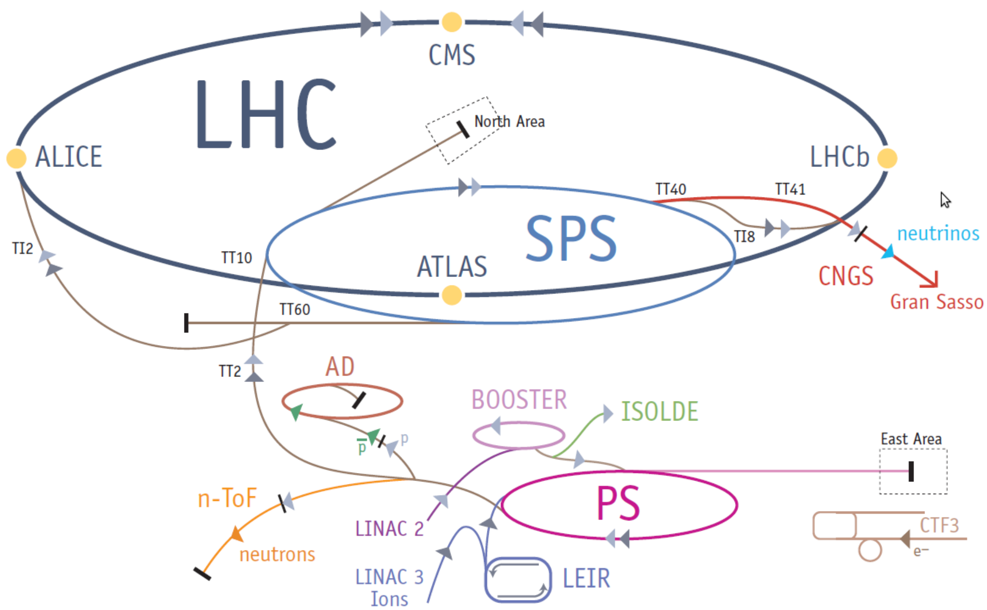

Figure 1.1 Shematic view of CERN Accelerator setup.

the proton-proton collider LHC at CERN. Although it has the same scientific goals as the ATLAS experiment, it uses different technical solutions and design of its detector magnet system to achieve these.

One of the outstanding features of the CMS detector is its strong solenoid magnet. It provides 3.8 Tesla axial magnetic field to measure the charged particles momentum. The bore of the solenoid is instrumented with various particle detection systems, including (from innermost to outermost part): a silicon pixel and strip tracker, an electromagnetic calorimeter (ECAL) and a hadronic calorimeter (HCAL). The steel return yoke outside the solenoid is instrumented with gas detectors which are used to identify muons. In addition to the barrel and endcap detectors, CMS has extensive forward calorimetry.

Figure 1.2 shows CMS coordinate system, the polar angle θ is measured from the positive z-axis and the azimuthal angle ϕ is measured in the xy-plane. The pseudorapidity η is defined as $\eta = -\log[\tan(\theta/2)]$. 'Transverse' quantities refer to the component in the xy-plane perpendicular to the beam axis. (BAYATIAN, 2006) After the interaction, the inner tracker quantify charged particle trajectories

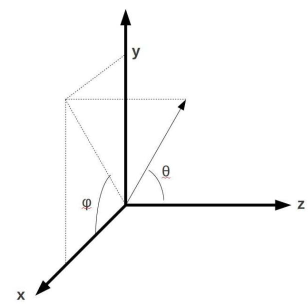

Figure 1.2 CMS detector coordinate system.

in the $|\eta| < 2.5$. It is developed by 1,440 silicon pixel and 15,148 silicon strip detector modules. It provides an impact parameter resolution about 15 μm and a transverse momentum (p_T) resolution better then 1%, for charged particles with p_T above 40 GeV. The ECAL consists of nearly 76,000 lead tungstate crystals which provide coverage $|\eta| <1.479$ in the barrel region (EB) and $1.479 < |\eta| < 3.0$ in the two endcap regions (EE). A preshower detector consisting of two planes of silicon sensors interleaved with a total of 3 radiation lenghth of lead is located in front of the EE. The ECAL has an ultimate energy resolution better than 0.5% for unconverted photons and better than 3% for electrons, in the energy above 100 GeV. The hadronic calorimeter is a sampling device with brass/scintillator as a passive/active material. The HCAL and ECAL cells are grouped into towers projecting radially outward from the origin. In the region $|\eta| <1.74$ these calorimeters have width $\Delta\eta = \Delta\phi = 0.087$; the η and ϕ widths increase at higher values of η. ECAL and HCAL cell energies above noise suppression thresholds are summed within each projective tower to define the calorimeter tower energy. When combined together, HCAL and ECAL measure jets with a resolution $\Delta E/E \simeq 100\%/\sqrt{E} \oplus 5\%$. The energy E and momentum $\vec{p}$ of a jet are defined as the scalar sum and vector sums, respectively, of the calorimeter cell energies associated with the jets.

The detector is nearly hermetic, allowing for energy balance measurements in the plane transverse to the beam directions.

Muons are detected in the window $|\eta| <2.4$, with detection planes based on drift tubes, cathode strip chambers, and resistive plate chambers. A high-p_T muon originating from the interaction point produces track segments in typically 3-4 muon stations. Matching these segments to tracks measured in the inner tracker results in a p_T resolution between 1% and 5% for p_T values up to 100 GeV (CHATRCHYAN, 2008).

Figure 1.3 shows interaction of particles with detector materials.

- Jets which consist of hadrons, can leave very weak signal in tracker or ECAL. However, most of jets energy deposit in the HCAL calorimeter.
- High energetic photons can not interact any detector part until they decay into a pair of electron positron in ECAL.
- Muons can leave very weak energy in calorimeters but in many cases they only interact in muon chamber.
- Single track of electrons point the part of ECAL and their enery deposit in the ECAL calorimeter.
- Neutrinos or any weakly interacting particles can not leave any signal on detector. If those particles exist in any decay the algorithm will calculate missing momentum which is imbalance with the jets.

The main characteristics of CMS detectors are;

- CMS muon detector allows to identify muons with a high momentum resolution in very wide energy and angular range. These features allows to measure dimuon mass system with good resolution.
- CMS electromagnetic calorimeter has good energy resolution. The mass of dielectron and diphoton systems have good resolution. Good π^0 granularity for rejection. Good isolated electron and photon identification.
- Good charged particle momentum resolution and reconstruction efficiency due to very efficient inner tracker.

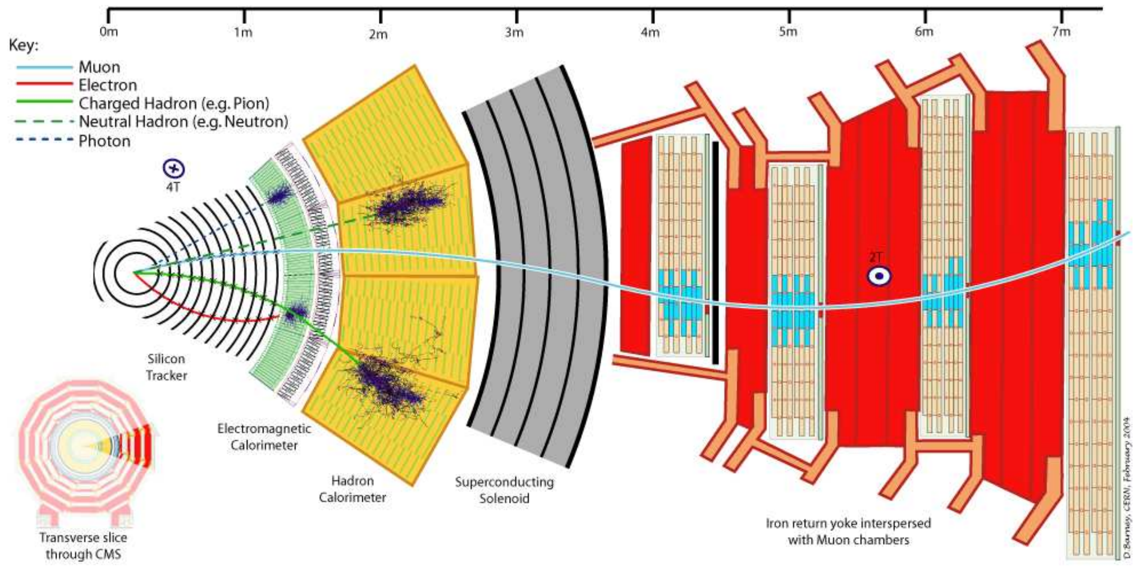

Figure 1.3 Interaction of particles with CMS detector materials.

- Good missing transverse energy and dijet mass resolution. Very large geometric coverage of hadronic calorimeter allows a very efficient measurements of the missing energy. This measurements are very important for the beyond standart models.

The first level (L1) of the CMS trigger system, composed of custom hardware processors, is designed to select the most interesting events using informations from the calorimeters and muon system. The High Level Trigger (HLT) processor farm exploits the informations from all subsystems and further decreases the event rate to a few hundred Hz, before data storage.

1.2 The Tracking System

The CMS tracking system is designed to reconstruct high energy charged particles with high momentum resolution and efficiency. The tracker is the subdetector closer to the interaction point, placed in the superconductive solenoid; it is designed to determine the interaction vertex, measure the momentum of the charged particles with good accuracy and identify the presence of secondary vertexes. It has a diam-

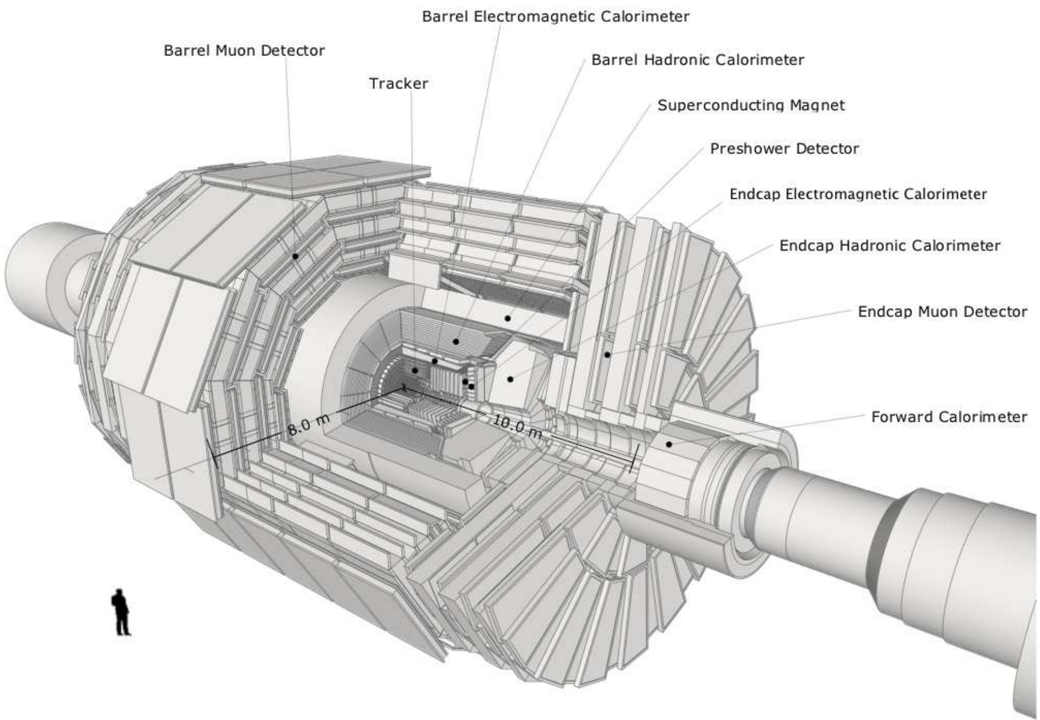

Figure 1.4 A schematic view of the CMS detector (Sakuma, 2012).

eter of 2.5 m and a length of 5.8 m. Over the tracker, 4 T magnetic field is provided homogeneously by the CMS solenoid magnet. The tracker must be able to operate without degrading its performances in the hard radiation environment of LHC and it has to comply with severe material budget (see Figure 1.5) constraints, in order not to degrade the excellent energy resolution of the electromagnetic calorimeter. The tracker consists of two parts. One is the silicon pixel detector and the other

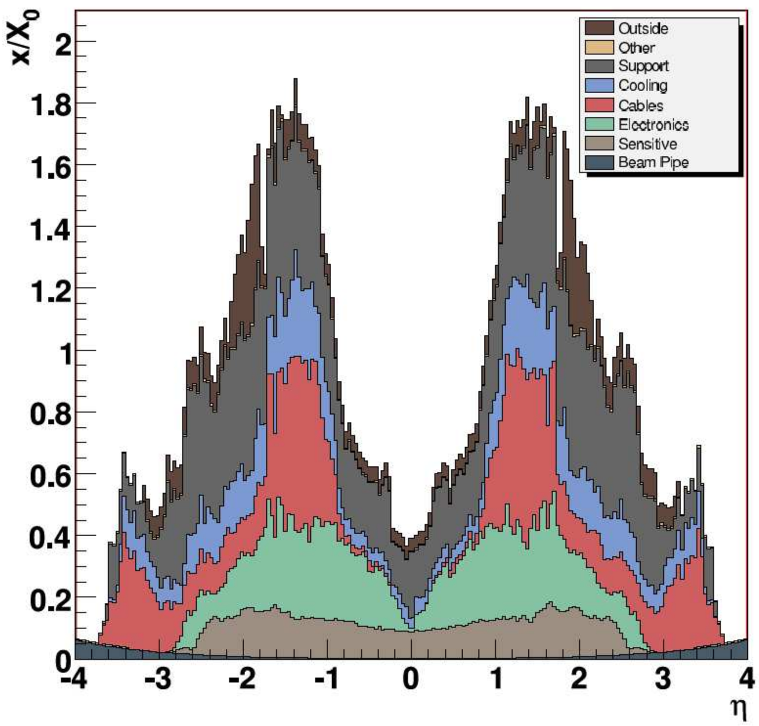

Figure 1.5 Material budget as a function of η. The thickness is expressed in terms of radiation length (X_0). The peak around =1.5 corresponds to the cables and services of the tracker.

is the silicon strip detector. Strip tracker: the barrel region is divided into 2 parts TIB (Tracker Inner Barrel) and TOB (Tracker Outer Barrel). The TIB is made of 4 layers and covers up to $|z| < 65$ cm, using silicon sensor with a thickness of 320 μm and a strip pitch which varies from 80 to 120 μm. The TOB comprises 6 layers with a half- length of $|z| < 110$ cm. As the radiation levels are smal in this region, thicker silicon sensors (500 μm) can be used to maintain a good S/N ratio for longer strip length and wider pitch. The strip pitch varies from 120 to 180 μm. The endcaps are divided into the TEC (Tracker End Cap) and TID (Tracker Inner Disk). Each

TEC comprises 9 disks that extend into the region 120 cm $< |z| <$ 280 cm, and each TID comprises 3 small disks that fill the gap between the TIB and the TEC Pixel Tracker: The pixel detector consists of three barrel layers with two endcap disks on each side of them. The three barrel layers are located at mean radii of 4.4 cm, 7.3 cm and 10.2 cm, and have a length of 53 cm. The two end disk, extending from 6 to 15 cm in radius, are placed on each side at $|z| = 34.5$ cm and 46.5 cm. It can be seen shematic view of CMS traking system in Figure 1.6 (BAYATIAN, 2006).

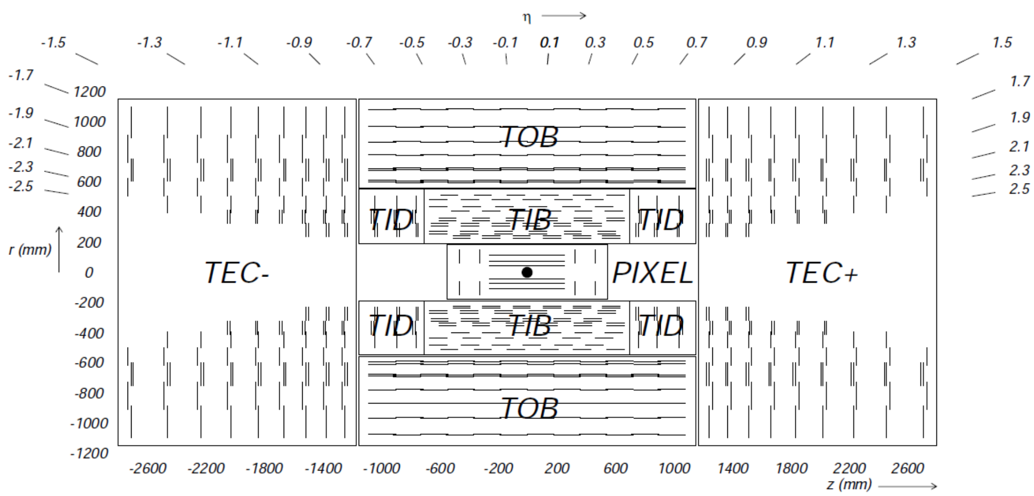

Figure 1.6 Schematic cross section through the CMS tracker. Each line represents a detector module. Double lines indicate back-to-back modules which deliver stereo hits.

1.3 Calorimeters

A calorimeter measure the energy of particles which interact with material of calorimeter and deposit their energy. The CMS calorimeters measure energy of photons, electrons and hadrons (jets). The CMS calorimeter has two parts: electro-magnetic calorimeter and hadronic calorimeter and these calorimeters is divided into central, endcap and forward region. The ECAL calorimeter measures the energy of particles interacting electromagnetically (photons and electrons). The HCAL calorimeter measures the energy of strongly interacting particles, hadrons (e.g. π^+, π^0, K etc.). Figure 1.7 shows that quadrant of CMS calorimeter system with tracker (BAYATIAN, 2006).

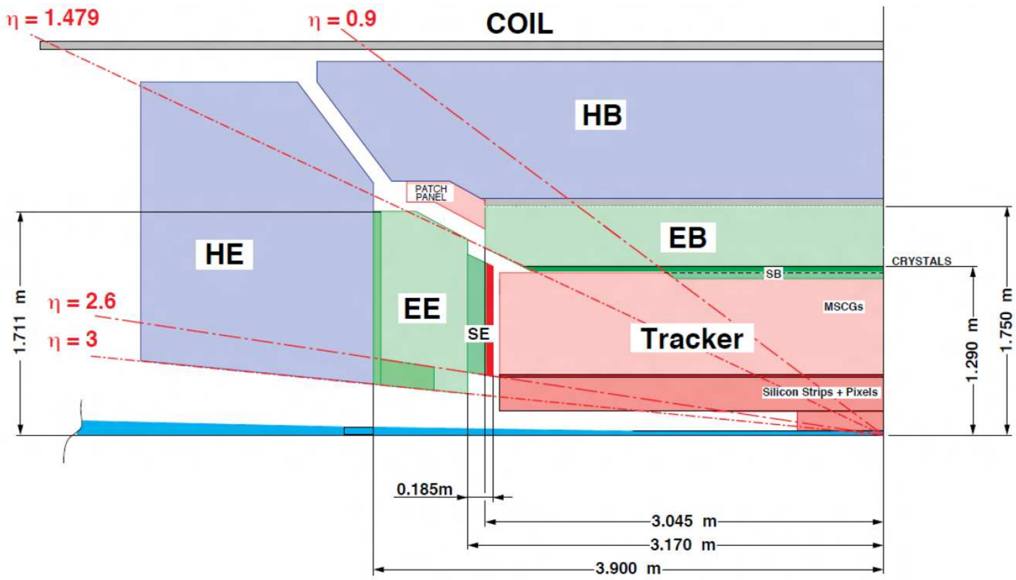

Figure 1.7 A shematic view of quadrant of CMS calorimeters.

1.3.1 The Electromagnetic Calorimeter (ECAL)

The electromagnetic calorimeter (ECAL) is placed around the tracker. It is aimed at the measurement of the energy of electromagnetic objects such as electrons and photons including electromagnetic component of hadronic and τ-jets. The design of the CMS ECAL was driven by the requirements imposed by the search of the Higgs boson in the channel $H \to \gamma\gamma$, where a peak in the di-photon invariant mass placed at the Higgs mass has to be distinguished from a continuous background. A good resolution and a fine granularity are therefore required: both of them improve the invariant mass resolution on the di-photon system by improving respectively the energy and the angle measurement of the two photons. The fine granularity also helps to obtain a good π^0/γ separation.

The ECAL is a hermetic homogeneous calorimeter made of 61200 lead tungstate $(PbWO_4)$ crystals in the barrel part $(EB, |\eta| < 1.48)$ and closed by 7324 crystals in each of two endcaps $(EE, 1.5 < |\eta| < 3.0)$ (BAYATIAN, 2006). The

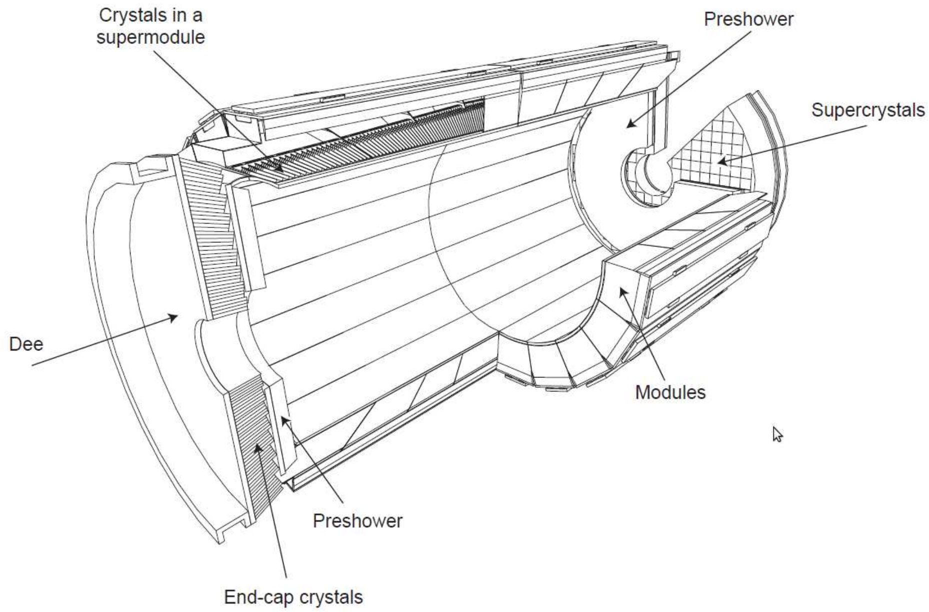

Figure 1.8 Shematic view of the CMS electromagnetic calorimeter.

Barrel section (EB) has an inner radius of 129 cm. It is structured as 36 identical ”supermodules” each covering half the barrel length and corresponding to a pseudorapidity interval of $0 < |\eta| < 1.479$. The crystals are quasi-projective (the axes are tilted at 3^o with respect to the line from the nominal vertex position) and cover 0.0174 (i.e. 1^o) in $\triangle\phi$ and $\triangle\eta$.

The endcaps (EE), at a distance of 314 cm from the interaction vertex and covering a pseudorapidity range of $1.479 < |\eta| < 3.0$, are each structured as two ”Dees”, consisting of semi-circular aluminium plates from which are cantilevered structural units of 5×5 crystals, known as ”supercrystal”.

One of the relevant issue in evaluating the performances of the electromagnetic calorimeter is its energy resolution. In the relevant energy range between 25 GeV and 500 GeV, the energy resolution is usually parametrized as the sum in quadrature of three different terms:

$$\frac{\sigma(E)}{E} = \frac{a}{\sqrt{E}} \oplus \frac{b}{E} \oplus c \tag{1.1}$$

where a, b and c are named respectively stochastic, noise and constant term, and E is the energy expressed in GeV. The target values for CMS are 2.7% for a, 200

MeV when adding the signal of 5×5 crystals for b, and 0.5% for c. Their relative contributions are reported in the plot of Figure 1.9. It can be noticed that above 50 GeV the resolution is dominated by the constant term. Different effects contribute to the different terms in Eq. (1.1).

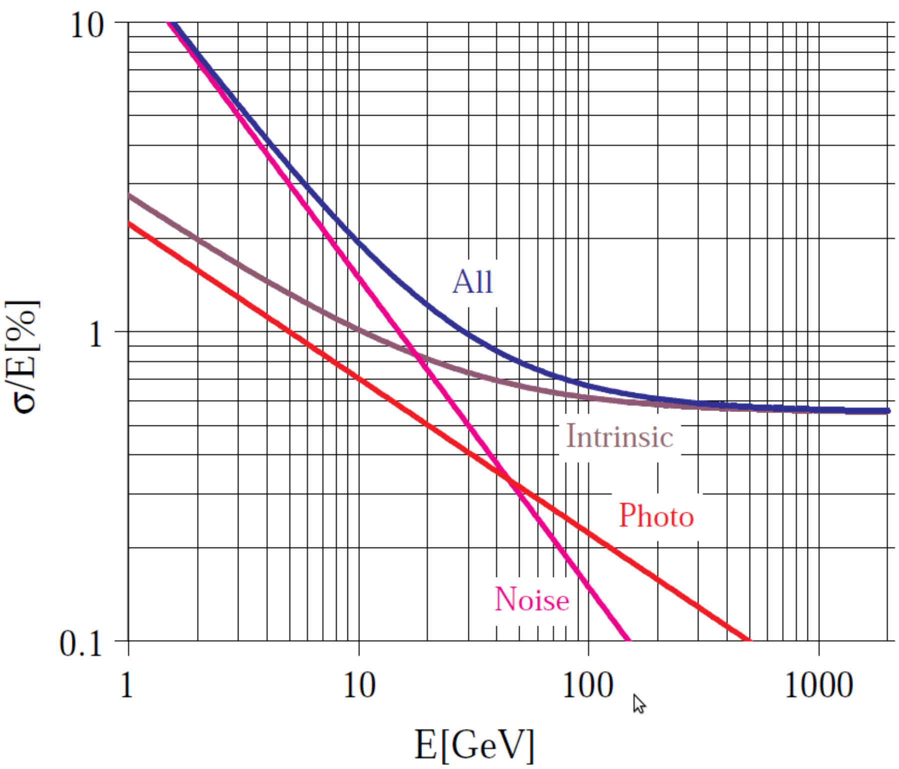

Figure 1.9 The expected ECAL energy resolution versus the energy of the impacting electron. The different contributions are superimposed separately. The term ”Intrinsic” includes the shower containment and a constant term (0.55%).

- The stochastic term a receives a contribution from the fluctuations in the number of electrons which reaches the preamplifier (ne). These fluctuations are proportional to $\sqrt{ne}$ and therefore proportional to the square root of the deposited energy. Contributions to this term come from the light yield of the crystals, from the efficiency in collecting light onto the photodetector surface and from the quantum efficiency of the photodetector (CHATRCHYAN, 2008).

- The noise term b accounts for all the effects that can alter the measurements of the energy deposit independently of the energy itself. This term receives contributions from the electronic noise and from the pile-up events, whose contribution are different in the barrel and in the endcaps and can vary with the luminosity of LHC. The target values for the barrel (at η=0) and the end-caps (at η=2) in the low luminosity running are respectively 155 MeV and 205 MeV while in the high luminosity running they are 210 MeV and 245 MeV.

- The constant term determines the energy resolution at high energy. Many different effects contribute to this term: the stability of the operating conditions such as the temperature and the high voltage of the photodetectors; the electromagnetic shower containment and the presence of the dead material of the supporting structure between the crystals; the light collection uniformity along the crystal axis; the intercalibration between the channels which contributes almost directly to the overall energy resolution since the most of the energy is contained into few crystals; the radiation damage of the $PbWO_4$ crystals.

1.3.2 Hadronic Calorimeter

The design of the hadron calorimeter (HCAL) is strongly influenced by the choice of magnet parameters since most of the CMS calorimetry is located inside the magnet coil and surrounds the ECAL system. An important requirement of HCAL is to minimize the non-Gaussian tails in the energy resolution and to provide good containment and hermeticity for the E_T^{miss} measurement. Hence, the HCAL design maximizes material inside the magnet coil in terms of interaction lengths. This is complemented by an additional layer of scintillators, referred to as the hadron outer (HO) detector, lining the outside of the coil.

The Hadron Barrel (HB) part of HCAL consist of 32 towers covering the pseudorapidity region $-1.4 < \eta < 1.4$, resulting in 2304 towers with a segmentation $\triangle\eta \times \triangle\phi = 0.087 \times 0.087$. The HB is constructed in two half barrels.

The Hadron Outer (HO) detector contains scintilators with a thickness of 10 mm, which line the outside of the outer vacuum tank of the coil and cover the region $-1.26 < \eta < 1.26$. The tiles are grouped in 30^o sectors, matching the ϕ segmentation of the drift tube chambers. They sample the energy from penetrating hadron showers leaking through the rear of the calorimeters and so serve as a "tail-catcher" after the magnet coil. They increase the effective thickness of the hadron calorimeter to over 10 interaction lengths, thus reducing the tails in the energy resolution function. The HO also improves the E_T^{miss} resolution of calorimeter. The

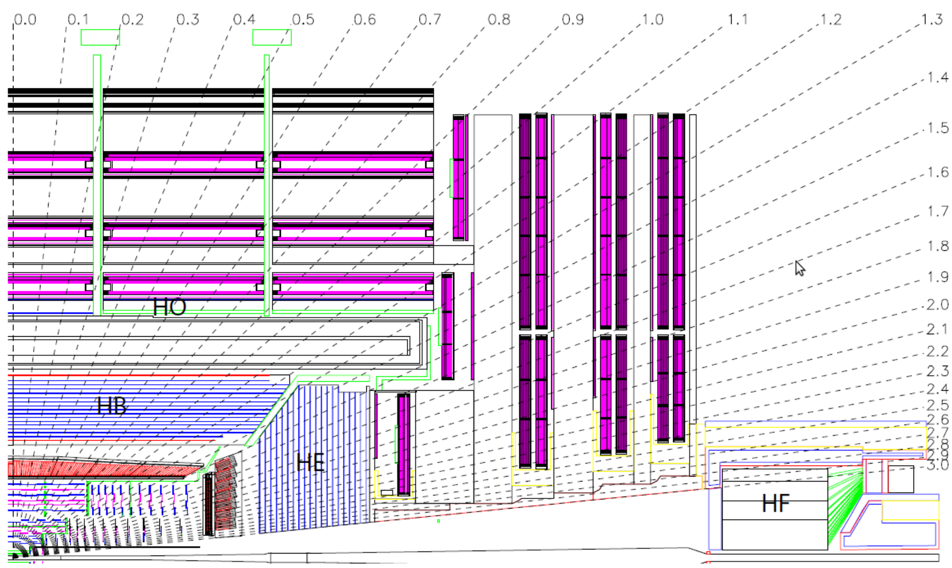

Figure 1.10 Longitudinal view of the CMS detector showing the locations of the hadron barrel (HB), endcap (HE), outer (HO) and forward (HF) calorimeters.

Hadron Endcap (HE) consists of 13 η towers with 5^o ϕ segmentation, covering the pseudorapidity region $1.3 < |\eta| < 3.0$. For the five outermost towers (at smaller η) the ϕ segmentation is 5^o and the η segmentation is 0.087. For the eight high η the ϕ segmentation is 10^o, whilst the η segmentation varies from 0.09 to 0.35 at the highest η. The total number of HE towers is 2304.

The Hadron Forward (HF) covers the region $3.0 < |\eta| < 5.19$ and it has 13 towers in η. All towers size are given by $\triangle\eta \approx 0.175$, except for the lowest-$\eta$ tower with $\triangle\eta \approx 0.1$ and the highest-η tower with $\triangle\eta \approx 0.3$. The ϕ segmentation of all towers is 10^o, except for the highest-η one which has $\triangle\phi = 20^o$. This leads to 900 towers and 1800 channels in the two HF modules.

If we calculate the hadron calorimeter η rings we will find 84 according to above introduction. However hadron calorimeter is divided 82 η region because HE and HB overlap in the region $1.305 < |\eta| < 1.392$.

1.4 Magnet

At the heart of CMS sits a 13-m-long, 5.9 m inner diameter, 12,000 ton, 4 T superconducting solenoid. The CMS magnet system consists of a superconducting coil, the magnet yoke (barrel and endcap), a vacuum tank and ancillaries such as cryogenics, power supplies and process controls. Inside the bore of the magnet sit the inner tracker and the calorimetry, while outside is the flux return system and muon detection.

In order to achieve good momentum resolution with a compact spectrometer it is necessary to have a combination of a high magnetic field and high precision on the spatial resolution and alignment of the detectors. The momentum measurement of charged particles in the detector is based on the bending of their trajectories. The 4T magnetic field also bring benefits for calorimetry - it enables the detection of many isolated electrons produced by the decays of Ws, Zs and b quarks. Using these electrons, the CMS crystal electromagnetic calorimeter can be calibrated to an accuracy of a fraction of a percent.

The magnetic flux is returned via a 1.5 m thick saturated iron yoke instrumented with four stations of muon chambers. The CMS magnet can be seen in Figure 1.11 (CHATRCHYAN, 2008).

1.5 Muon Chamber

Muons are expected to provide clean signatures for a wide range of physics processes.

The return field of the solenoid is large enough to saturate 1.5 m of iron, allowing

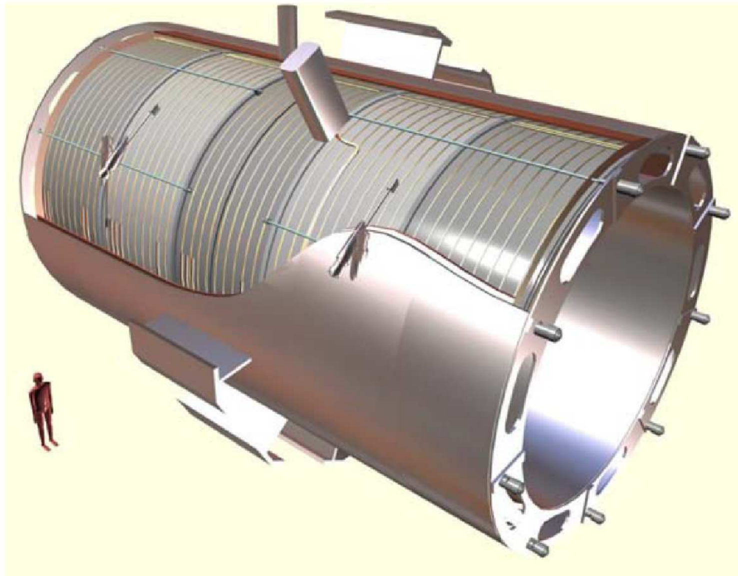

Figure 1.11 General viev of CMS Superconducting Magnet.

4 muon ”stations” to be interleaved with the iron return yoke plates of the magnet system. This provides a muon system with reconstruction efficiency better than 98% over the full pseudorapidity range.

Each muon station consists of several layers of aluminium drift tubes (DT) in the barrel region and cathode strip chambers (CSCs) in the endcap region, complemented by resistive plate chambers (RPCs). The muon detectors are arranged in concentric cylinders around the beam line in the barrel region, and in disks perpendicular to the beam line in the endcaps. Muon identification is ensured by the large thickness of the absorber material (iron), which cannot be traversed by particles other than neutrinos and muons. The DT and CSC detectors are used to obtain a precise measurement of the position and thus the momentum of the muons, whereas the RPC chambers are dedicated to providing fast information for the Level-1 trigger (see Figure 1.12). Muon measurements taken in the muon stations outside the solenoid are used for fast triggering and standalone muon reconstruction, but can also be combined with information from the inner tracking detectors for more precise reconstruction and momentum measurement.

Centrally produced muons are measured 3 times: in the inner tracker, after the

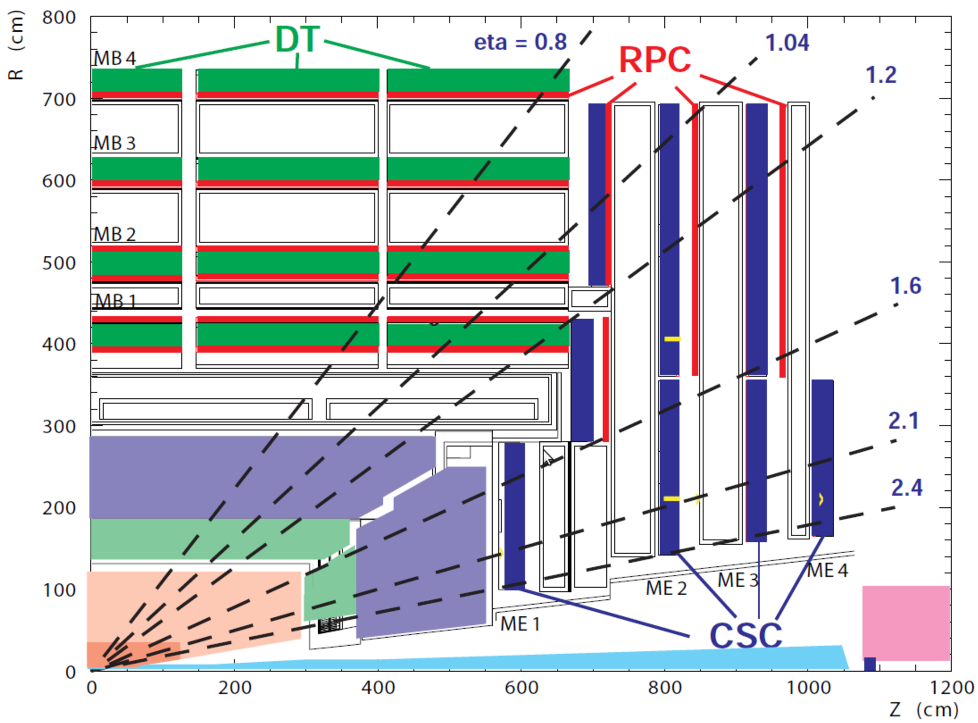

Figure 1.12 Layout of one quarter of the CMS muon system for initial low luminosity running. The RPC system is limited to $|\eta| < 1.6$ in the endcap, and for the CSC system only the inner ring of the ME4 chambers have been deployed.

coil, and in the return flux. Measurement of the momentum of muons using only the muon system is essentially determined by the muon bending angle at the exit of the 4 T coil, taking the interaction point (which will be known to $\approx 20\mu m$) as the origin of the muon. The resolution of this measurement (labelled ”muon system only” in Figure 1.13) is dominated by multiple scattering in the material before the first muon station up to p_T values of 200 GeV/c, when the chamber spatial resolution starts to dominate. For low-momentum muons, the best momentum resolution (by an order of magnitude) is given by the resolution obtained in the silicon tracker (”inner tracker only” in Figure 1.13). However, the muon trajectory beyond the return yoke extrapolates back to the beam-line due to the compensation of the bend before and after the coil when multiple scattering and energy loss can be neglected. This fact can be used to improve the muon momentum resolution at high momentum when combining the inner tracker and muon detector measurements (”full system” in Figure 1.13). Three types of gaseous detectors are used to identify and measure

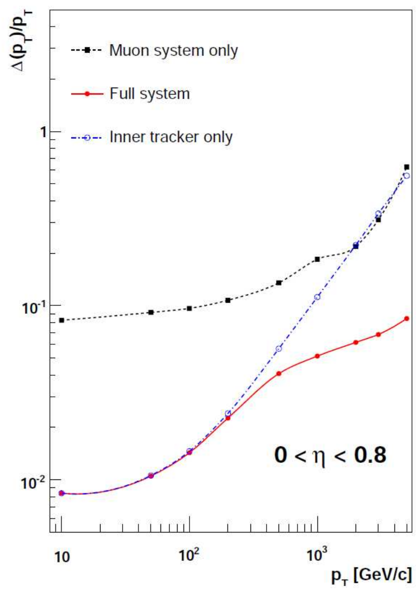

Figure 1.13 The muon transverse-momentum resolution as a function of the transverse-momentum (p_T) using the muon system only, the inner tracking only, and both. Left panel: $0 < |\eta| < 0.8$, right panel: $1.2 < |\eta| < 2.4$.

muons. The choice of the detector technologies has been driven by the very large surface to be covered and by the different radiation environments. In the barrel region ($|\eta| < 1.2$), where the neutron induced background is small, the muon rate is low and the residual magnetic field in the chambers is low, drift tube (DT) chambers are used. In the two endcaps, where the muon rate as well as the neutron induced background rate is high, and the magnetic field is also high, cathode strip chambers (CSC) are deployed and cover the region up to $|\eta| < 2.4$. In addition to this, resistive plate chambers (RPC) are used in both the barrel and the endcap regions. These RPCs are operated in avalanche mode to ensure good operation at high rates (up to 10 kHz/cm^2) and have double gaps with a gas gap of 2 mm. A change from the Muon TDR has been the coating of the inner bakelite surfaces of the RPC with linseed oil for good noise performance. RPCs provide a fast response with good time resolution but with a coarser position resolution than the DTs or CSCs. RPCs can therefore identify unambiguously the correct bunch crossing (CHATRCHYAN, 2008).

The DTs or CSCs and the RPCs operate within the first level trigger system, providing two independent and complementary sources of information. The complete system results in a robust, precise and flexible trigger device. In the initial stages of the experiment, the RPC system will cover the region $|\eta| < 1.6$. The coverage will be extended to $|\eta| < 2.1$ later. In the Muon Barrel (MB) region, four stations of detectors are arranged in cylinders interleaved with the iron yoke. The segmentation along the beam direction follows the five wheels of the yoke (labeled YB-2 for the farthest wheel in -z, and YB+2 for the farthest is +z). In each of the endcaps, the CSCs and RPCs are arranged in four disks perpendicular to the beam, and in concentric rings, three rings in the innermost station, and two in the others. In total, the muon system contains of order 25 000 m^2 of active detection planes, and nearly 1 million electronic channels.

2. LARGE EXTRA DIMENSION WITH ADD MODEL

2.1 The ADD Model

2.1.1 Introduction

Most part of this section comes from refference (GIUDICE, 2000). One of the most popular theoretical scenarios that predicts the monojet signal is Large Extra Dimensions (LED) in the framework of the ADD model (ARKANI-HAMED, 1998).

The model aims to solve the hierarchy problem between the electroweak and Planck scales by introducing a number δ of extra spatial dimensions, which in the simplest scenario are compactified over a torus and all have the same radius R. In this framework, the SM particles and gauge interactions are confined to the ordinary $3+1$ space-time dimensions, whereas gravity is free to propagate through the entire multidimensional space. The strength of the gravitational force is therefore effectively diluted and the fundamental scale of this (4+n) dimensional theory M_D is related to the apparent 4-dimensional Planck scale M_{Pl} according to the formula $M_{Pl}^2 \approx M_D^{\delta+2} R^{\delta}$. The present analysis sets lower limits on the fundamental Planck scale M_D for scenarios where the number of extra dimensions is varied from 2 to 6.

The monojet plus missing energy signature in the context of the ADD model can arise from the production of a real Graviton G balanced by an energetic hadronic jet via the $q\bar{q} \rightarrow gG$, $qg \rightarrow qG$, and $gg \rightarrow gG$ processes.

Current experimental constraints allow a scenario with $\delta \geq 2$, corresponding to extra dimensions sizes below 0.1 mm if the fundamental scale M_D is of the order of 1 TeV. At that scale, gravity can become stronger than in ordinary space and light Kaluza-Klein gravitons could be directly produced. Since gravitons are free to propagate in the extra dimensions, they escape the detector and can only be inferred from the amount of missing energy. The large size of the extra dimensions gives rise to dense Kaluza-Klein mass modes which for the collider phenomenology appear as a continuous graviton mass spectrum. Due to the large number of contributing mass states, graviton processes as the real emission, can obtain sufficiently large cross sections to be observed at the LHC.

2.1.2 Kaluza-Klein (KK) theories

KK theory is a model that unifies electromagnetism and gravitation by starting from a theory of Einstein gravity in five dimensions. The theory was first published in 1921 by Theodor Kaluza and extended in 1926 by Oscar Klein. Theodor Kaluza extended general relativity to five dimensional space-time. The outcome is sum of three different sets, one of which is equivalent to Einstein field equations, the second set equivalent to Maxwell's equations for the electromagnetic field and the third set an extra scalar field.

Extra dimensions that are identified by KK has to be cylindrically compactified with radius L. For instance, one extra dimension can be circle with radius L. This space could be a manifold like high dimensional sphere, torus, .. etc for more than one extra dimensions. As general, the total D-dimensional space can be written:

$$K = M^{3+1} \times X^{\delta}, \delta = D - 4 \tag{2.1}$$

where M is the Minkowski spacetime and X are the compact manifold of extra dimensions.

The KK aproach claims that D dimensional space-time has certain dynamics that gives rise to preferential compactification of the extra $(D-4)$-dimensions leaving four Minkowskian dimensions intact. The geometry $M^{3+1} \times X^{\delta}$ should be a solution of D-dimensional Einstein equations.

If L is approximately equal to distance scales, new dimensions can be visible. This means that new extra dimension is not visible, if L is much smaller than distance scale.

We start with simplest example of a real scalar field in 5-dimensional space time to understand the theory. The manifold X is assumed to be a 1-dimensional circle S^1 with radius L. The coordinate system is $X_A = (x_\mu, y)$ and a positive metric $[-++++..]$ is used. The Lagrangian density is:

$$\mathcal{L} = -\frac{1}{2}\partial_A \Phi \partial^A \Phi, \quad A = 0,1,2,3,5. \tag{2.2}$$

In this equation scalar field represented by $\Phi(t,\vec{x},y) \equiv \Phi(x_\mu,y)$, $\mu = 0,1,2,3$, and depends on both four dimensional coordinate x_μ and extra coordinate y. It is assumed that extra dimensions are compactified on a circle S^1 of radius L. Thus, the five-dimensional space-time has a geometry of $M^4 \times S^1$. According to new five dimensional space, scalar field should be periodic that means $y \to y + 2\pi L$:

$$\Phi(x,y) = \Phi(x, y + 2\pi L). \tag{2.3}$$

if we extend this field in the harmonics on a circle

$$\Phi(x,y) = \sum_{n=-\infty}^{+\infty} \phi_n(x)\, e^{iny/L}, \phi_n^*(x) = \phi_{-n}(x) \tag{2.4}$$

the Lagrangian density can be rewritten as follows;

$$\mathcal{L} = -\frac{1}{2}\sum_{n,m=-\infty}^{+\infty}\left(\partial_\mu \phi_n \partial^\mu \phi_m - \frac{nm}{L^2}\phi_n \phi_m\right) e^{i(n+m)y/L}, \tag{2.5}$$

and the action becomes:

$$S = \int d^4x \int_0^{2\pi L} dy \mathcal{L} = -\frac{2\pi L}{2}\int d^4x \sum_{n=-\infty}^{+\infty}\left(\partial_\mu \phi_n \partial^\mu \phi_n^* + \frac{n^2}{L^2}\phi_n \phi_n^*\right). \tag{2.6}$$

If it is integrated over the extra dimension coordinate y, it can be seen that the action is composed by infinite number of fields $\phi_n(x)$. Making the substitution $\varphi_n \equiv \sqrt{2\pi L}\phi_n$

$$S = \int d^4x \left[-\frac{1}{2}\partial_\mu \varphi_0 \partial^\mu \varphi_0\right] - \int d^4x \sum_{k=1}^{+\infty}\left(\partial_\mu \phi_k \partial^\mu \phi_k^* + \frac{k^2}{L^2}\phi_k \phi_k^*\right) \tag{2.7}$$

it can be seen that the compactification transformed the 5-dimensional scalar field in:

- A single real massless scalar field, called a *zero-mode*, φ_0;
- An infinite number of massive complex scalar fields with masses inversely proportional to the compactification radius, $m_k^2 = k^2/L^2$.

It can be summarized what explained above, Kaluza and Klein developed a compactified theory which include single massless and infinite number of massive complex scalar fields and a massless gauge field, the so called KK modes. For the masses hold the relation $m_k^2 = k^2/L^2 (k = 0, 1, 2, ...)$ the KK tower of massive gravitons. At low energies only the zero mode is essential, for high energies, $E > 1/L$ all the KK modes become important. The compactification yields a quantisation of the momentum corresponding to the compactified coordinate.

2.1.3 ADD Framework

ADD model evolved from equation (2.1) for $M_D \sim M_{EW}$. In this case, gravitational potential changes at small scales due to extra dimensional manifold compactified on a $M_D \sim M_{EW}$. We can write gravitational potential with Gauss Law, if we assume that δ-dimensions have a scale ≈ R (ARKANI-HAMED, 1998);

$$V(r) \sim \frac{1}{M_D^{\delta+2}} \frac{m_1 m_2}{r^{\delta+1}}, (r \ll R) \tag{2.8}$$

It can be seen the general potential behavior $1/r^{-1}$ for $(r \gg R)$.

$$V(r) \sim \frac{1}{M_D^{\delta+2} R^{\delta}} \frac{m_1 m_2}{r}, (r \gg R) \tag{2.9}$$

if we use $M_{Pl}^2 \sim M_D^{\delta+2} R^{\delta}$

$$V(r) \sim \frac{1}{M_{Pl}^2} \frac{m_1 m_2}{r} \tag{2.10}$$

Equation (2.10) shows that the ratio between Fundamental scale and Plank scale relates to the extension of extra dimensions and the number of extra dimensions. With this simple relationship it is also possible to retrieve the δ-dimensions order of magnitude, given the two fundamental parameters. For example $M_D \sim M_{EW}$

$$R \sim 10^{\frac{30}{\delta} - 17} cm \times \left(\frac{1TeV}{M_{EW}} \right)^{1+\frac{2}{\delta}} \tag{2.11}$$

Because deviation was not found in the motions of planets on a $a \sim 10^{13}$ cm scale by solar system gravitational measurements, the δ=1 case is excluded. SM fields are restricted on a 3-dimensional brane, that is called braneworld, with thickness $\sim$ M_{EW}. The SM fields' space has also almost flat geometry. The space X is called bulk, and it is presumed that just gravitons can propagate in it. A more detailed study can be found in (DVALI G. and SHIFMAN M.). An example of localization of a fermionic field is discussed here. The most common mechanism to constrain fields on a brane uses topological defects. A scalar theory with a double well potential is investigated to explain the mechanism of constrain fields (Figure 2.1).

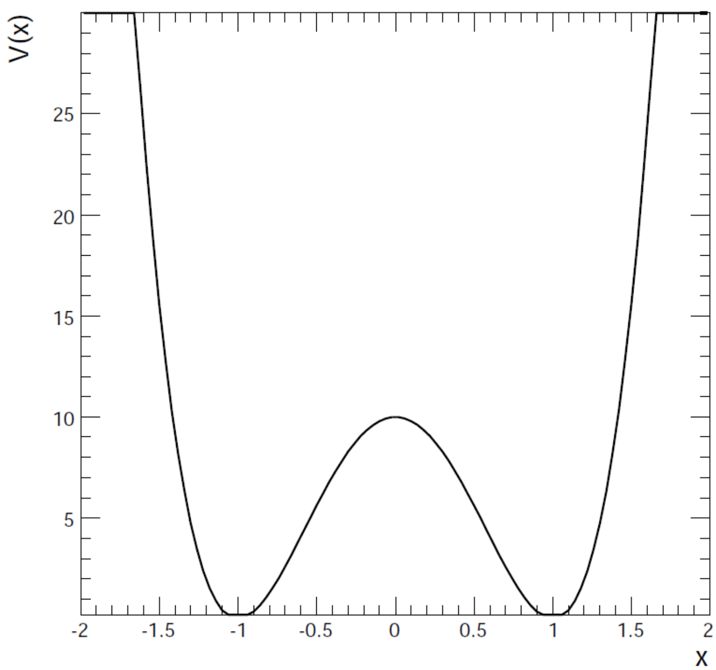

Figure 2.1 The double well potential.

$$S = \int d^4xdy \left[\frac{1}{2}(\partial_{A\varphi} - V(\varphi))\right] \tag{2.12}$$

$$V(\varphi) = -\frac{\lambda}{4}\left[\varphi^2(y) - \frac{\mu^2}{\lambda}\right]^2 \tag{2.13}$$

The solution depends on the y coordinate;

$$\varphi_e(y) \propto tanh\left(\frac{\mu}{\sqrt{2}}y\right) \tag{2.14}$$

This solution is asymptotic to the classical vacua's of the model:

$$\varphi(\pm\infty) = \pm v = \pm\frac{\mu}{\sqrt{\lambda}} \tag{2.15}$$

It can be seen from Eq. (2.15) that the results break the translational invariance along the fifth dimension, leaving 4-dimensional Poincare invariance intact. The solution is called kink which is shown in Figure 2.2. Let us describe a fermionic field coupled with Yukawa interaction for the scalar field.

$$S = \int d^4xdz\left(i\Psi\Gamma^A\partial_A\Psi - h\varphi\Psi\Psi\right) \tag{2.16}$$

with the 5-dimensional gamma-matrices defined as:

$$\Gamma^\mu = \gamma^\mu, \mu = 0,1,2,3 \tag{2.17}$$

$$\Gamma^y = -i\gamma^5 \tag{2.18}$$

The equation of motion of the kink (2.14) is described by:

$$i\Gamma^A\partial_A\Psi - h\varphi_c z\Psi = 0 \tag{2.19}$$

Due to Poincare invariance, a 4-dimensional momentum $p_\mu p^\mu = m^2$ can be defined. The solution for $m = 0$ is called zero mode (JACKIW, 1976). In this case $\gamma^\mu p_\mu \Psi_0$ is equal zero and Dirac equation becomes;

$$\gamma_5\partial_y\Psi_0 = h\varphi_c(y)\Psi_0 \tag{2.20}$$

The zero mode is left handed from the 4-dimensional view point because $\gamma^5\gamma^5 = -1$ and takes form:

$$\Psi_0 = e^{\int_0^y dy' h\varphi_c(y')}\psi_L(p) \tag{2.21}$$

$\psi_L(p)$ represents 4-dimensional Weyl equation. Eq. (2.21) shows that the zero mode is localized near $y = 0$ and exponentially large y. In these modes, matter can freely travel in the braneworld in the direction of x_1, x_2, x_3 but it is not moving through to y direction. At high energies a continuum of modes would appear leaving the fermions unbounded from braneworld and y disappearing from our world.

Consequently, we can mention about few results of ADD model. Accelerated gauge coupling unification: Altough the renormalization group for running coupling constants is logarithmic in 4-dimensional theories, this behaviour changes in

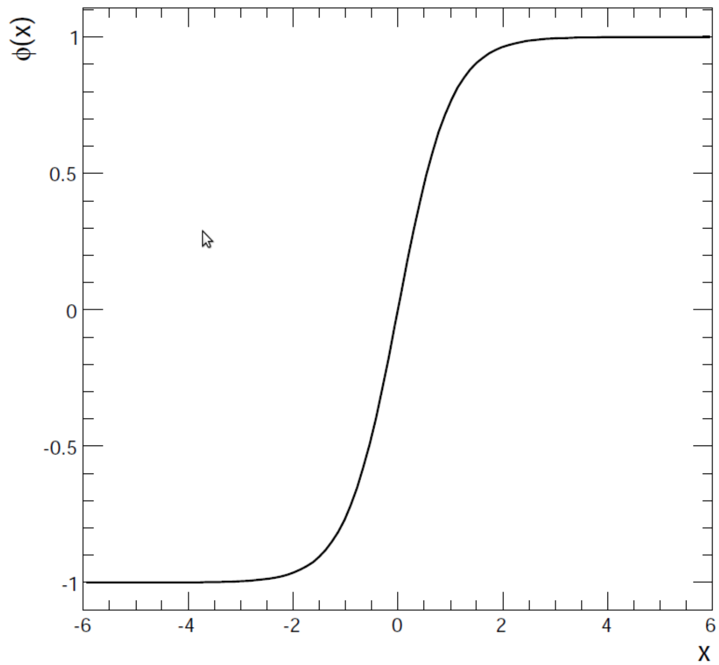

Figure 2.2 The kink solution.

higher dimensions (TAYLOR, 1988). It was shown that this gives rise to an accelerated unification at energy $\sim M_D$ for strong, electromagnetic and weak forces. Excess of missing energy in collider experiments: The SM particles disappearing phenomenon would lead to an excess of missing energy in collider experiments, provided that the particle energy is enough. This effect can be also given by the direct production of KK gravitons.

2.1.4 The KK Excitations of the Graviton

In this section, we discuss the equations that characterize the Kaluza-Klein excitation of the graviton and describe the physical degrees of freedom in the effective theory. The equation of motion can be written as the Einstein equation in $D = 4 + \delta$ dimension, at low energy and small curvature, (GIUDICE, 2000).

$$\mathcal{G}_{AB} \equiv \mathcal{R}_{AB} - \frac{1}{2} g_{AB} \mathcal{R} = -\frac{T_{AB}}{\bar{M}_D^{2+\delta}} \qquad A, B = 1, \ldots, D, \tag{2.22}$$

where $\bar{M}_D$ is the reduced Planck mass of the D-dimensional theory.

Generally, the brane on which we live creates a non-trivial D-dimensional metric background. But, it is quite reasonable to assume that brane surface tension does not exceed the fundamental scale M_D^4. Thus, the metric g_{AB} will be flat, when the distance from brane gets much bigger than $1/M_D$. After definition of assumptions, the metric tensor can be written as:

$$g_{AB} = \eta_{AB} + 2\bar{M}_D^{-1-\delta/2} h_{AB} \tag{2.23}$$

where η_{AB} the D-dimensional Minkowski metric. If we keep only the first power of h_{AB}, Eq. (2.22) becomes

$$\begin{aligned} \bar{M}_D^{1+\delta/2} \mathcal{G}_{AB} &= \Box h_{AB} - \partial_A \partial^C h_{CB} - \partial_B \partial^C h_{CA} + \partial_A \partial_B h_C^C \\ &- \eta_{AB} \Box h_C^C + \eta_{AB} \partial^C \partial^D h_{CD} = -\bar{M}_D^{-1-\delta/2} T_{AB}, \end{aligned} \tag{2.24}$$

A point in the D-dimensional space is described by the set of coordinates $z = (z_1, \ldots, z_D)$. With this information, we can separate the ordinary four-dimensional coordinates from the Minkowski ones:

$$z = (x, y) \qquad x = (x_0, \vec{x}),\ y = (y_1, \ldots, y_\delta), \quad \delta = D - 4. \tag{2.25}$$

We want periodicity of the fields under the following translation in the compactified space

$$y_j \to y_j + 2\pi R \quad j = 1, \ldots, \delta, \tag{2.26}$$

where R is the compactification radius. For convenience we presume that the compactified space is a torus, but our considerations are valid for different compact spaces. Equation (2.26) emphasizes

$$h_{AB}(z) = \sum_{n_1=-\infty}^{+\infty} \cdots \sum_{n_\delta=-\infty}^{+\infty} \frac{h^{(n)}{}_{AB}(x)}{\sqrt{V_\delta}} e^{i\frac{n^j y_j}{R}}, \tag{2.27}$$

where $n = (n_1, \ldots, n_\delta)$ and V_δ is the volume of the compactified space,

$$V_\delta = (2\pi R)^\delta. \tag{2.28}$$

The tensor $h(z)$ is broken up an infinite sum of KK modes on the 4-dimensional space. It is assumed that SM is confined in the braneworld in the limit of weak gravitational field, the energy-momentum tensor becomes;

$$T_{AB}(z) = \eta_A^\mu \eta_B^\nu T_{\mu\nu}(x)\delta(y) \quad \mu,\nu = 0,\ldots,3. \tag{2.29}$$

The singularity of the δ function in Eq. (2.29) will assumably be smoothed by effects of the finite brane-size in the transverse direction. On the other hand, these effects are important only in the short-distance regime. Eq. (2.29) shows that the Kaluza-Klein modes of the energy-momentum tensor are independent of n, in the low-energy region, where n is smaller than $\bar{M}_D R$. This result is important for this analysis, because it requires a universal coupling of all relevant Kaluza-Klein gravitons to ordinary matter, hence provide us to make definite predictions on their production cross-sections. Notice that Eq. (2.29) can more formally be obtained via the induced metric $\hat{g}_{\mu\nu}$ on the brane

$$\hat{g}_{\mu\nu}(x) = g_{AB}[Y(x)]\partial_\mu Y^A(x)\partial_\nu Y^B(x) \tag{2.30}$$

Y^A represents the background fields defining the position of the brane. The metric $\hat{g}$ measures distances on the brane and should be used to write a covariant action. In the static gauge ($Y^\mu = x^\mu$ for $\mu = 0,\ldots,3$ and $Y_i = 0$ for $i = 4,\ldots,D-1$) one simply has $\hat{g}_{\mu\nu} = g_{\mu\nu}$, and the above coupling to bulk (μ,ν) gravitons follows. We should remember that there might also be couplings to (i,j) gravitons (polarized orthogonal to the brane). Above all, if the fields Y^i is dynamical, the field couple to gravitons via $h_{ij}\partial_\mu Y^i \partial_\nu Y^j \eta^{\mu\nu}$. Furthermore, in the case of D-branes there are also fermions (the partners of Y^i) that couple to the perpendicularly polarized gravitons h_{ij}, while gauge bosons obviously cannot. The coupling to h_{ij} is evidently model dependent, and it does not seem incompatible to presume that it vanishes for the Standard Model degrees of freedom. Our analysis established in this assumption on the basis of Eq. (2.29).

Emission and absorption of gravitons by the brane, is studied by Klebanov and Gubser, in the context of D branes (KLEBANOV, 1997 and GUBSER, 1997). In this case, if $\sqrt{s}$ is larger than the string scale, one can even perform the calculation in the high-energy region, using string theory. It is worth pointing out that the low-energy (soft gravitons) limit of that calculation agrees with the result obtained by an effective theory, where the bulk gravitons propagate in a flat background and couple to the fields on the brane via the induced metric (HASHIMOTO, 1996). If we go back to the equations of motion, we get the following set of equations, after multiplying both sides of the Kaluza-Klein expansion of Eq. (2.24) by $e^{-i\frac{n'}{R}\cdot y}$ and integrating over the extra-dimensional coordinates:

$$\begin{aligned} \mathcal{G}^{(n)}{}_{\mu\nu}(x) &\equiv (\Box+\hat{n}^2)h^{(n)}{}_{\mu\nu} - \left[\partial_\mu\partial_\lambda h^{(n)}{}^{\lambda}_{\nu} + i\hat{n}_j\partial_\mu h^{(n)}{}^{j}_{\nu} + (\mu\leftrightarrow\nu)\right] + \\ &\left[\partial_\mu\partial_\nu - \eta_{\mu\nu}(\Box+\hat{n}^2)\right]\left[h^{(n)}{}^{\lambda}_{\lambda} + h^{(n)}{}^{j}_{j}\right] + \\ &\eta_{\mu\nu}\left[\partial^\lambda\partial^\sigma h^{(n)}{}_{\lambda\sigma} + 2i\hat{n}_j\partial^\lambda h^{(n)}{}^{j}_{\lambda} - \hat{n}^j\hat{n}^k h^{(n)}{}_{jk}\right] = -\frac{T_{\mu\nu}}{M_P}, \end{aligned} \quad (2.31)$$

$$\begin{aligned} \mathcal{G}^{(n)}{}_{\mu j}(x) &\equiv (\Box+\hat{n}^2)h^{(n)}{}_{\mu j} - \partial_\mu\partial_\nu h^{(n)}{}^{\nu}_{j} - i\hat{n}_k\partial_\mu h^{(n)}{}^{k}_{j} - i\hat{n}_j\partial_\nu h^{(n)}{}^{\nu}_{\mu} \\ &+\hat{n}_j\hat{n}_k h^{(n)}{}^{k}_{\mu} + i\hat{n}_j\partial_\mu\left[h^{(n)}{}^{\nu}_{\nu} + h^{(n)}{}^{k}_{k}\right] = 0, \end{aligned} \quad (2.32)$$

$$\begin{aligned} \mathcal{G}^{(n)}{}_{jk}(x) &\equiv (\Box+\hat{n}^2)h^{(n)}{}_{jk} - \left[i\hat{n}_j\partial_\mu h^{(n)}{}^{\mu}_{k} - \hat{n}_j\hat{n}_\ell h^{(n)}{}^{\ell}_{k} + (j\leftrightarrow k)\right] \\ &-\left[\hat{n}_j\hat{n}_k + \eta_{jk}(\Box+\hat{n}^2)\right]\left[h^{(n)}{}^{\mu}_{\mu} + h^{(n)}{}^{\ell}_{\ell}\right] + \\ &\eta_{jk}\left[\partial^\mu\partial^\nu h^{(n)}{}_{\mu\nu} + 2i\hat{n}_\ell\partial^\mu h^{(n)}{}^{\ell}_{\mu} - \hat{n}^\ell\hat{n}^m h^{(n)}{}_{\ell m}\right] = 0. \end{aligned} \quad (2.33)$$

Here the D'Alambertian operator ($\Box = \partial^\mu\partial_\mu$) acts on the four-dimensional space, and we have defined[1] $\hat{n} \equiv n/R$, $\hat{n}^2 \equiv -\hat{n}^j\hat{n}_j = \sum_{j=1}^{\delta}|\hat{n}_j|^2$. We are able to rewrite the quantity.

$$\bar{M}_P \equiv \sqrt{V_\delta}\bar{M}_D^{1+\delta/2} = (2\pi R)^{\delta/2}\bar{M}_D^{1+\delta/2} \equiv R^{\delta/2}M_D^{1+\delta/2} \quad (2.34)$$

as the ordinary reduced Planck mass, $\bar{M}_P = M_P/\sqrt{8\pi} = 2.4\times 10^{18}$ GeV. It is also described the D-dimensional Planck mass, relevant to the reduced Planck mass, by the equation $M_D = (2\pi)^{\delta/(2+\delta)}\bar{M}_D$ for future convenience. Starting from

[1] In conventions, the flat metric is $\eta_{\mu\nu} = \mathrm{diag}(+,-,-,-)$ and $\eta_{jk} = -\delta_{jk}$.

Eq. (2.34) and using the point of view of general relativity, we have obtained the relation, (ARKANI-HAMED, 1998) between M_P and M_D previously obtained in ref. (LYKKEN, 1996). In order to solve the system of coupled differential equations it is useful to rewrite them in terms of the following new dynamical variables:

$$\begin{aligned}
G^{(n)}{}_{\mu\nu} &\equiv h^{(n)}{}_{\mu\nu} + \frac{\kappa}{3}\left(\eta_{\mu\nu} + \frac{\partial_\mu\partial_\nu}{\hat{n}^2}\right) H^{(\vec{n})} - \partial_\mu\partial_\nu P^{(n)} + \\
&\quad \partial_\mu Q^{(n)}_\nu + \partial_\nu Q^{(n)}_\mu \qquad (2.35)\\
V^{(n)}{}_{\mu j} &\equiv \frac{1}{\sqrt{2}}\left[ih^{(n)}{}_{\mu j} - \partial_\mu P^{(n)}{}_j - \hat{n}_j Q^{(n)}{}_\mu\right] \qquad (2.36)\\
S^{(n)}{}_{jk} &\equiv h^{(n)}{}_{jk} - \frac{\kappa}{\delta-1}\left(\eta_{jk} + \frac{\hat{n}_j\hat{n}_k}{\hat{n}^2}\right) H^{(\vec{n})} + \hat{n}_j P^{(n)}_k + \\
&\quad \hat{n}_k P^{(n)}_j - \hat{n}_j\hat{n}_k P^{(n)} \qquad (2.37)\\
H^{(\vec{n})} &\equiv \frac{1}{\kappa}\left[h^{(n)}{}^j_j + \hat{n}^2 P^{(n)}\right] \qquad (2.38)\\
Q^{(n)}{}_\mu &\equiv -i\frac{\hat{n}_j}{\hat{n}^2} h^{(n)}{}^j_\mu \qquad (2.39)\\
P^{(n)}{}_j &\equiv \frac{\hat{n}_k}{\hat{n}^2} h^{(n)}{}^k_j + \hat{n}_j P^{(n)} \qquad (2.40)\\
P^{(n)} &\equiv \frac{\hat{n}^j\hat{n}^k}{\hat{n}^4} h^{(n)}{}_{jk}. \qquad (2.41)
\end{aligned}$$

The degrees of freedom contained in $G^{(n)}{}_{\mu\nu}, V^{(n)}{}_{\mu j}, S^{(n)}{}_{jk}, H^{(\vec{n})}, Q^{(n)}{}_\mu, P^{(n)}{}_j, P^{(n)}$ correctly match the number of degrees of freedom in h_{AB} without giving a redundant description, because of the identities $\hat{n}^j V^{(n)}{}_{\mu j} = 0$, $\hat{n}^j S^{(n)}{}_{jk} = 0$, $S^{(n)}{}^j_j = 0$, $\hat{n}^j P^{(n)}{}_j = 0$. For convenience, we choose

$$\kappa = \sqrt{\frac{3(\delta-1)}{\delta+2}}, \qquad (2.42)$$

in order to have a canonical normalization of the field $H^{(\vec{n})}$. Notice that, for $\delta = 1$, our parametrization is singular, since the fields $P^{(n)}{}_j$, $P^{(n)}$, and $H^{(\vec{n})}$ are no longer independent. However, we will be interested only in the case $\delta > 1$.

By agreeing the free indices of eqs. (2.31)–(2.33) either with the flat metric tensor or with ∂^μ and $\hat{n}^j$ $(j = 1, \ldots, \delta)$, it is obtained three constraints[2] on the

[2] The constraints come from the equations $\mathcal{G}^{(n)}{}^\mu_\mu = -T^\mu_\mu/\bar{M}_P$, $\partial^\mu \mathcal{G}^{(n)}{}_{\mu\nu} = 0$, and $\hat{n}^j \mathcal{G}^{(n)}{}_{jk} = 0$. Notice that the conditions $\hat{n}^j \mathcal{G}^{(n)}{}_{\mu j} = 0$ and $\partial^\mu \mathcal{G}^{(n)}{}_{\mu j} = 0$ do not provide further constraints because they identically follow from the previous equations and energy-momentum conservation in D dimensions. Finally the information of the equation $\mathcal{G}^{(n)}{}^j_j = 0$ is directly contained in the equations of motion.

Kaluza-Klein components of the tensor h ($n \neq 0$):

$$\partial^\mu G^{(n)}{}_{\mu\nu} = \frac{\partial_\nu T^\mu_\mu}{3\hat{n}^2 M_P} \tag{2.43}$$

$$G^{(n)\mu}{}_\mu = \frac{T^\mu_\mu}{3\hat{n}^2 M_P} \tag{2.44}$$

$$\partial^\mu V^{(n)}{}_{\mu j} = 0. \tag{2.45}$$

Replacing in eqs. (2.31)–(2.33) the constraints given in eqs. (2.43)–(2.45), we can rewrite the equations of motion for each of the Kaluza-Klein modes $n \neq 0$ as

$$\left(\Box + \hat{n}^2\right) \quad G^{(n)}{}_{\mu\nu} = \frac{1}{M_P}\left[-T_{\mu\nu} + \left(\frac{\partial_\mu \partial_\nu}{\hat{n}^2} + \eta_{\mu\nu}\right)\frac{T^\lambda_\lambda}{3}\right] \tag{2.46}$$

$$\left(\Box + \hat{n}^2\right) \quad V^{(n)}{}_{\mu j} = 0 \tag{2.47}$$

$$\left(\Box + \hat{n}^2\right) \quad S^{(n)}{}_{jk} = 0 \tag{2.48}$$

$$\left(\Box + \hat{n}^2\right) \quad H^{(\vec{n})} = \frac{\kappa}{3M_P} T^\mu_\mu. \tag{2.49}$$

These equations show that only $G^{(n)}{}_{\mu\nu}, V^{(n)}{}_{\mu j}, S^{(n)}{}_{jk}, H^{(\vec{n})}$ describe propagating particles, while $Q^{(n)}{}_\mu, P^{(n)}{}_j, P^{(n)}$ do not appear in the equations of motions. This result can be understood by studying the transformation properties of the different fields under coordinate reparametrization. Let us consider a general coordinate transformation

$$z_A \to z'_A = z_A + \varepsilon_A(z), \tag{2.50}$$

where $\partial_B \varepsilon_A$ is at most of the same order of magnitude as h_{AB}. This transformation induces a variation of the metric such that

$$\delta_\varepsilon h_{AB} = -\partial_A \varepsilon_B - \partial_B \varepsilon_A. \tag{2.51}$$

Using a Kaluza-Klein mode expansion for the gauge parameter ε

$$\varepsilon_A(z) = \sum_{n_1=-\infty}^{+\infty} \cdots \sum_{n_\delta=-\infty}^{+\infty} \varepsilon^{(n)}{}_A(x) e^{i\frac{n^j y_j}{R}}, \tag{2.52}$$

the diffeomorphism in Eq. (2.51) induces the following transformation laws for the fields defined in eqs. (2.35)–(2.41),

$$\delta_\varepsilon G^{(n)}{}_{\mu\nu} = 0, \quad \delta_\varepsilon V^{(n)}{}_{\mu j} = 0, \quad \delta_\varepsilon S^{(n)}{}_{jk} = 0, \quad \delta_\varepsilon H^{(\vec{n})} = 0, \tag{2.53}$$

$$\delta_\varepsilon Q^{(n)}{}_\mu = \frac{1}{2}\partial_\mu \delta_\varepsilon P^{(n)} + \varepsilon^{(n)}{}_\mu \quad (2.54)$$

$$\delta_\varepsilon P^{(n)}{}_j = -\frac{1}{2}\hat{n}_j \delta P^{(n)} - i\varepsilon^{(n)}{}_j \quad (2.55)$$

$$\delta_\varepsilon P^{(n)} = 2i\frac{\hat{n}_j}{\hat{n}^2}\varepsilon^{(n)j}. \quad (2.56)$$

Thus, while $G^{(n)}{}_{\mu\nu}, V^{(n)}{}_{\mu j}, S^{(n)}{}_{jk}, H^{(\vec{n})}$ are gauge-invariant fields, $Q^{(n)}{}_\mu, P^{(n)}{}_j, P^{(n)}$ are gauge-dependent and do not describe physical particles. In particular, they can all be simultaneously set to zero at any four-dimensional space-time point for any $n \neq 0$. We will refer to the gauge choice in which $Q^{(n)}{}_\mu = 0$, $P^{(n)}{}_j = 0$, $P^{(n)} = 0$ as the unitary gauge.

We now want to identify the physical content of the gauge-invariant fields. The free propagation of $G^{(n)}{}_{\mu\nu}$ is given by eqs. (2.43) and (2.46) in the limit $T_{\mu\nu} = 0$,

$$\left(\Box + \hat{n}^2\right) G^{(n)}{}_{\mu\nu} = 0 \quad (2.57)$$

$$\partial^\mu G^{(n)}{}_{\mu\nu} = 0 \quad (2.58)$$

$$G^{(n)\mu}{}_\mu = 0. \quad (2.59)$$

Equation (2.57) describes the free propagation of the bosonic modes $G^{(n)}{}_{\mu\nu}$ having squared masses equal to $\hat{n}^2$. For any given n, the constraints in eqs. (2.58)–(2.59) eliminate 5 degrees of freedom out of the 10 contained in the symmetric tensor $G^{(n)}{}_{\mu\nu}$. This leaves 5 propagating modes corresponding to the physical degrees of freedom of a massive spin-two particle, the n-th Kaluza-Klein excitation of the graviton. The condition of the unitary gauge corresponds to eliminating the spin-zero ($P^{(n)}$) and spin-one ($Q^{(n)}{}_\mu$) particles eaten by the massless graviton to form a spin-two massive multiplet.

The fields $V^{(n)}{}_{\mu j}$ (satisfying $\hat{n}^j V^{(n)}{}_{\mu j} = 0$) describe $\delta - 1$ spin-one particles which form massive multiplets by absorbing the fields $P^{(n)}{}_j$. These vector particles satisfy the Lorentz condition, see Eq. (2.45), and each contains three physical degrees of freedom. They are not coupled to the energy-momentum tensor in the weak-field limit, see Eq. (2.47), and therefore will play no role in this analysis of collider experiments. Next, for $\delta \geq 2$, there are $(\delta^2 - \delta - 2)/2$ massive real scalars described by the symmetric tensor $S^{(n)}{}_{jk}$, which satisfies the relations $\hat{n}^j S^{(n)}{}_{jk} = 0$, $S^{(n)}{}_j^j = 0$. These scalars are also not coupled to matter, see Eq. (2.48). Finally, there is the scalar $H^{(\vec{n})}$ which is coupled only to the trace of the energy-momentum tensor, see Eq. (2.49). If we impose the equations of motion, T^{μ}_{μ} vanishes for conformally-invariant theories. Thus $H^{(\vec{n})}$ does not participate in any tree-level process involving massless matter field. The scalar $H^{(\vec{n})}$ can only couple to ordinary particles at tree level proportionally to their masses. These couplings give effective interactions at best of order M_Z^2/M_D^2, which are negligible for our considerations. Indeed one may worry about the existence of a massless mode associated with $H^{(\vec{n})}$, which would lead to unwanted violations of the Equivalence Principle (a difference in Newton's constant characterizing the coupling to photons and to non-relativistic matter). The mode in question corresponds to a fluctuation, named radion in ref. (ARKANI-HAMED, 1998), of the volume of the δ compactified dimensions. Thus, whatever mechanism stabilizes the radius of the extra dimensions, it will give a mass to the radion. In ref. (ARKANI-HAMED, 1998) several mechanisms of radius stabilization were described and it was shown that it is not difficult to give the radion a mass larger than $(1\ \text{mm})^{-1} \sim 2 \times 10^{-4}$ eV. This is sufficient to satisfy the present experimental bounds. Such a tiny mass for $H^{(\vec{n})}$ affects our previous analysis only for the lowest Kaluza-Klein modes. As a final remark, the radion corresponds to the zero mode of h^j_j. Since $n = 0$, this mode cannot be gauged away even in the special case of $\delta = 1$, in which the radion Kaluza-Klein excitations are eaten by the massive spin-2 graviton.

Adding the numbers of physical degrees of freedom for $G^{(n)}{}_{\mu\nu}$, $V^{(n)}{}_{\mu j}$, $S^{(n)}{}_{jk}$, and $H^{(\vec{n})}$ we obtain a total of $(4+\delta)(1+\delta)/2$. It is interesting to do the same counting from the point of view of the D-dimensional theory. The symmetric tensor h_{AB} contains $D(D+1)/2$ massless components. In order to compute the physical degrees of freedom, we first need to fix the gauge, say by the harmonic condition $\partial_A h^A_B = \frac{1}{2}\partial_B h^A_A$. Analogously to the case of QED, we then discover that, for a massless graviton, we still have residual freedom to make gauge transformations with gauge parameters ε_A subject to the condition $\Box\varepsilon_A = 0$. In total we eliminate $2D$ components from h_{AB}, leaving $D(D-3)/2$ physical states. For $D = 4$ we find the 2 degrees of freedom of a massless graviton, and for $D = 4+\delta$ we recover the same result previously obtained from a four-dimensional Kaluza-Klein point of view.

2.2 Graviton Production Processes

In this thesis it is consider to observe monojet ($jet + MET$) signature. To observe this signal in pp collision there are 3 ADD model production process which are shown in (Figure 2.3). In addition to those process it is considered $photon + MET$ signature to compare results with $jet + MET$ signature.

- $g + g \rightarrow g + G$
- $g + q \rightarrow q + G$
- $q + \bar{q} \rightarrow g + G$
- $q + \bar{q} \rightarrow \gamma + G$

where G is tensor field $G^{(n)}_{\mu\nu}$ obtained in previous section. The graviton mass splits

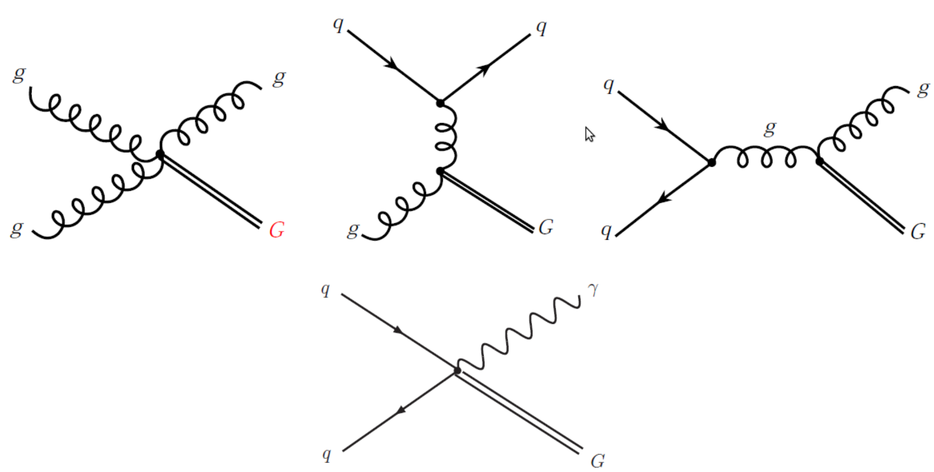

Figure 2.3 Production channels for the emission of a real graviton at the LHC

up for different excitation in Kaluza-Klein modes because masses are equal to $|n|/R$.

$$\Delta m \sim \frac{1}{R} = M_D \left(\frac{M_D}{M_P}\right)^{2/\delta} \sim \left(\frac{M_D}{\text{TeV}}\right)^{\frac{\delta+2}{2}} 10^{\frac{12\delta-31}{\delta}} \text{eV}. \tag{2.60}$$

It has been used relation between the effective Planck mass of D-dimensional theory M_D and the compactification radius R, Eq. (2.34). If M_D is to be defined as 1 TeV and $\delta = 4, 6, 8$, then Δm is equal to 20 keV, 7 MeV, and 0.1 GeV, respectively. Only for a large number of extra dimensions does the mass splitting become comparable with the experimental energy resolution. However, for large δ, only a small number of Kaluza-Klein modes can be produced and the total cross-section is negligible. We are interested in the case in which δ is not too large (say $\delta \lesssim 6$), where the enormous number of accessible Kaluza-Klein modes can compensate the $1/\bar{M}_P^2$ factor in the scattering amplitude.

For experimental applications, it can be explained the graviton production rate in terms of inclusive cross section, where the contributions of the different Kaluza-Klein modes have been summed up. If δ is not too large the mass splitting Δm is so small. So we can replace sum over the different Kaluza-Klein states by a continuous integration. The number of modes with Kaluza-Klein index between $|n|$ and $|n| + dn$ is given by

$$dN = S_{\delta-1} |n|^{\delta-1} dn, \qquad S_{\delta-1} = \frac{2\pi^{\delta/2}}{\Gamma(\delta/2)}, \tag{2.61}$$

where $S_{\delta-1}$ is the surface of a unit-radius sphere in δ dimensions[3] . Using Eq. (2.34) and the expression $m = |n|/R$ for the Kaluza-Klein excitation mass, we can rewrite the measure in Eq. (2.61) as

$$dN = S_{\delta-1} \frac{\bar{M}_P^2}{M_D^{2+\delta}} m^{\delta-1} \, dm. \tag{2.62}$$

Thus we explain the differential cross section for inclusive graviton production as

$$\frac{d^2\sigma}{dt \, dm} = S_{\delta-1} \frac{\bar{M}_P^2}{M_D^{2+\delta}} m^{\delta-1} \frac{d\sigma_m}{dt}, \tag{2.63}$$

[3] For $\delta = 2n$ and n integer, we find $S_{\delta-1} = 2\pi^n/(n-1)!$ and, for $\delta = 2n+1$, we find $S_{\delta-1} = 2\pi^n/\Pi_{k=0}^{n-1}(k+\frac{1}{2})$.

where $d\sigma_m/dt$ is the differential cross-section for producing a single Kaluza-Klein graviton of mass m. Since the graviton interaction vertex is suppressed by $1/\bar{M}_P$ we can anticipate that $\sigma_m \propto \bar{M}_P^{-2}$, and the factor $\bar{M}_P^2$ appearing from the phase-space summation exactly cancels the Planck mass dependence in Eq. (2.63).

The same result can also be obtained from the point of view of the D-dimensional theory. Here, the canonically normalized graviton h_{AB} has a coupling to matter $\mathcal{L}_D = -T^{AB}h_{AB}/\bar{M}_D^{1+\delta/2}$. The graviton phase space is

$$d\Phi_G = \frac{d^{D-1}k_D}{(2\pi)^{D-1}2\sqrt{k_D\cdot k_D}} = \frac{d^\delta k_T}{(2\pi)^\delta}\times\frac{d^3k}{(2\pi)^3 2\sqrt{\vec{k}^2+m^2}}, \tag{2.64}$$

where we have decomposed k_D in the components k_T and k respectively orthogonal and parallel to the brane. Graviton emission from the brane is, in lowest order, independent of the orientation of k_T so we can trivially integrate on it: $d^\delta k_T = S_{\delta-1}m^{\delta-1}dm$. The cross section for an initial brane state $|p_1,p_2\rangle$ to go in a final brane state $|f\rangle$ plus a bulk graviton $|G\rangle$ is then

$$d\sigma = \frac{S_{\delta-1}m^{\delta-1}dm}{M_D^{2+\delta}}\left|\langle f,G|T^{\mu\nu}h_{\mu\nu}|p_1,p_2\rangle\right|^2(2\pi)^4\delta^4(P_i-P_f)\frac{d\Phi_f}{F(p_1,p_2)}, \tag{2.65}$$

where $d\Phi_f$ is the brane final state phase space, and $F(p_1,p_2)$ is just the usual flux factor for two particle collision. This equation agrees with Eq. (2.63).

We now give the differential cross-sections for producing a Kaluza-Klein graviton of mass m in processes which are relevant to the high-energy collider experiments. The cross-section for producing a graviton and a photon in a fermion-antifermion collision is

$$\frac{d\sigma_m}{dt}(f\bar{f}\to\gamma G) = \frac{\alpha Q_f^2}{16N_f}\,\frac{1}{s\bar{M}_P^2}\,F_1(t/s,m^2/s). \tag{2.66}$$

Here Q_f and N_f are the electric charge and number of colours of the fermion f, and F_1. The cross-sections for the parton processes relevant to graviton plus jet production in hadron collisions are

$$\frac{d\sigma_m}{dt}(q\bar{q}\to gG) = \frac{\alpha_s}{36}\,\frac{1}{s\bar{M}_P^2}\,F_1(t/s,m^2/s) \tag{2.67}$$

$$\frac{d\sigma_m}{dt}(qg\to qG) = \frac{\alpha_s}{96}\,\frac{1}{s\bar{M}_P^2}\,F_2(t/s,m^2/s) \tag{2.68}$$

$$\frac{d\sigma_m}{dt}(gg \to gG) = \frac{3\alpha_s}{16}\,\frac{1}{s\bar{M}_P^2}\,F_3(t/s, m^2/s) \tag{2.69}$$

We want to stress again that our calculation of graviton emission is based on an effective low-energy theory, valid below the scale M_D. Of course, we cannot determine the precise scale at which our effective low-energy theory breaks down. Nevertheless, we can use naive dimensional analysis to estimate the energy scale at which perturbation theory breaks down. If we analyse graviton loop corrections in D dimensions, we observe that the expansion parameter is (Donoghue, 1995)

$$\frac{S_{D-1}}{2(2\pi)^D}\left(\frac{E}{M_D}\right)^{D-2}. \tag{2.70}$$

Here, S_{D-1} is the surface of the D-sphere given in Eq. (2.61), and E is the relevant energy of the process. Requiring that the expansion parameter is less than unity, we obtain an estimate of the maximum energy at which we can trust a perturbative expansion in the effective theory

$$E_{\max} = [\Gamma(2+\delta/2)]^{\frac{1}{2+\delta}}\,(4\pi)^{\frac{4+\delta}{4+2\delta}}\,M_D. \tag{2.71}$$

Numerically, one finds always that $E_{\max} > 7.2M_D$. Although perturbativity can be trusted up to $E_{\max}$, new quantum-gravity effects may appear much sooner.

The total jet + nothing cross-section at the LHC integrated for all $E_{T,\mathrm{jet}} > E_{T,\mathrm{jet}}^{\min}$ with the requirement that $|\eta_{\mathrm{jet}}| < 3.0$ is shown in Figure 2.4. The Standard Model background is the dash-dotted line, and the signal is plotted as solid and dashed lines for fixed $M_D = 5\,\mathrm{TeV}$ with $\delta = 2$ and 4 extra dimensions. The **a** (**b**) lines are constructed by integrating the cross-section over $\hat{s} < M_D^2$

2.2.1 Current Collider Constraints for ADD Model

The current collider constraints are shown in Figure 2.5 from ATLAS (AAD, 2011), CDF (AALTONEN, 2008), D0 (ABAZOV, 2008) and LEP (HEISTER, 2003). In order to produce ADD model graviton in the detector there are several production process which are used in previous studies. Those are;

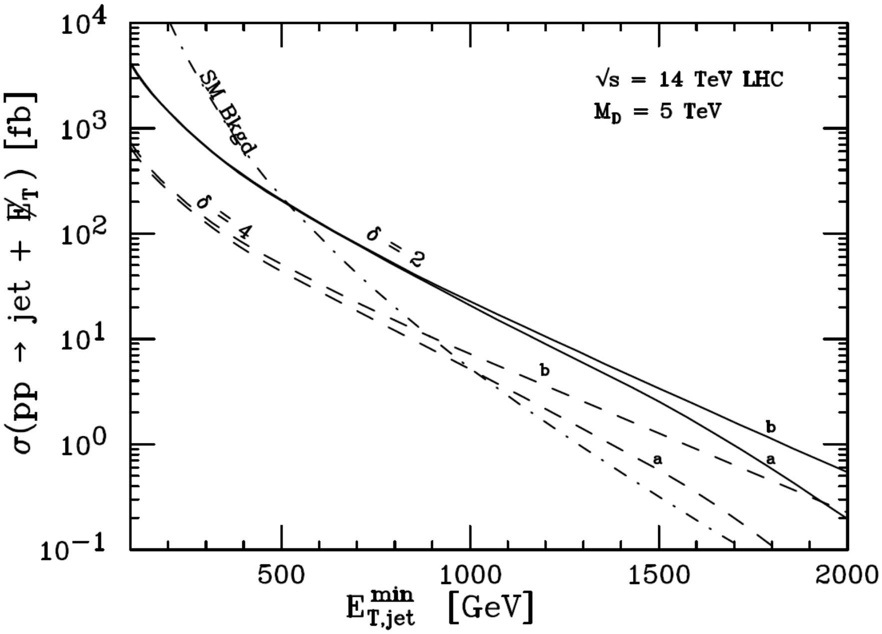

Figure 2.4 The total jet+nothing cross section at the LHC integrated for all the $E_T^{jet} > E_T^{min,jet}$ and $|\eta_{jet}| < 3$. The a (b) lines are constructed by integrating the cross section over $\hat{s} < M_D^2$ (Giudice, 2000).

- $e^- e^+ \longrightarrow \gamma G$
- $q\bar{q} \longrightarrow \gamma G$
- $q\bar{q} \longrightarrow gG, qg \longrightarrow qG, gg \longrightarrow gG$

Since graviton is very weakly interacting particle, it can not leaves any kind of signal in the detector in all production process. Instead it can be observed as missing transverse energy which is imbalanced with a photon or a jet. Those two kind of signal (a photon +Met and a jet + Met) are studied at $e^- e^+$, $p\bar{p}$ and pp colliders.

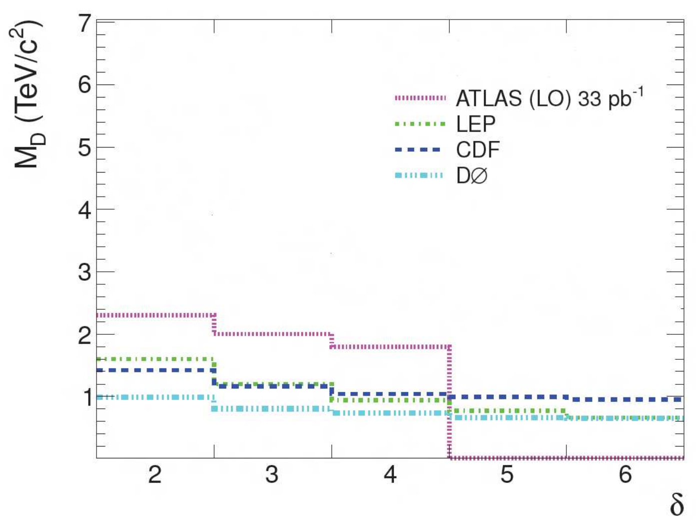

Figure 2.5 95% confidence level lower limit on fundamental mass scale M_D as a function of number of extra dimensions in ADD model (ATLAS, CDF, D0 and LEP).

3. DARK MATTER WITH MONOJET

3.1 Introduction

According to astrophysical and cosmological aspect, dark matter (DM) is a type of matter hypothesized to explain a large part of the total mass in the Universe.

Since it cannot emits or absorbs light or other electromagnetic radiation at any significant level DM cannot be seen directly like baryons with telescopes. Althought a small proportion of DM may be baryonic DM which emit little or no electromagnetic radiation, study of nucleosynthesis in the Big Bang produces an upper bound on the amount of baryonic matter in the Universe, (TRIMBLE, 1987) which indicates that the vast majority of DM in the Universe cannot be baryons. In astrophysical research, DM existence and properties are inferred from its gravitational effects on visible matter, radiation, and the large scale structure of the Universe. The current understanding of the Universe shows that about 23% of its mass is non-baryonic and non-relativistic DM, arround 73% of mass is in the form of dark energy and only a remaining fraction, below 4%, is ordinary baryonic matter with a very little amount of antimatter (BERTONE, 2005). The unknown dark energy and DM component is the most important missing piece in our understanding of the Universe.

Due to huge discrepancies between DM and normal matter such as stars, gas and dust, DM search comes to the attention of astrophysicists. It was first postulated by Jan Oort in 1932 to account for the orbital velocities of stars in the Milky Way and Fritz Zwicky in 1933 to account for evidence of ”missing mass” in the orbital velocities of galaxies in clusters. Subsequently, other observations have indicated the presence of DM in the Universe, including the rotational speeds of galaxies (see Figure 3.1), gravitational lensing of background (see Figure 3.2), objects by galaxy clusters such as the Bullet Cluster (see Figure 3.3), and the temperature distribution of hot gas in galaxies and clusters of galaxies.

According to consensus among cosmologists, DM is composed primarily of a new, not yet characterized, type of subatomic nonbaryonic particle. The search for this particle, by a variety of means, is one of the major efforts in particle physics today (BERTONE, 2005).

There are three prominent hypotheses on nonbaryonic DM particle, called Hot Dark Matter (HDM), Warm Dark Matter (WDM), and Cold Dark Matter (CDM); some combination of these is also possible. The most widely discussed models for nonbaryonic dark matter are based on the Cold Dark Matter hypothesis, and the corresponding particle is most commonly assumed to be a weakly interacting massive particle (WIMP). Hot dark matter might consist of (massive) neutrinos. The WIMPs when produced non-thermally could be candidates for warm dark matter such as axions. In general, however the thermally produced WIMPs are cold dark matter candidates.

Detection of WIMP have been considered in 3 nonastrophysical experiments classification which consider to observe DM-nucleon cross section (direct detection), anhilation products of DM (indirect detection) and production of DM (collider search).

In this thesis it considers to observe WIMPs at CMS detector with 2 models which produce monojet and balanced missing transverse energy in proton-proton collision.

3.2 Weakly Interacting Massive Particles (WIMPs)

Suppose that in addition to the SM particles, there is a particle which is undiscovered, stable (or long-lived) weakly interacting massive particle (WIMP). WIMPs are cold DM which is the simplest explanation for most cosmological observations. It is currently the area of greatest interest for DM research, as hot DM does not seem to be viable for galaxy and galaxy cluster formation, and most particle candidates become non-relativistic at very early times, hence are classified as cold.

At very early times DM mass less than temperatures ($m_\chi \ll T$), the equilibrium number density of such particles is $n_\chi \propto T^3$, but once Universe comes to low temper-

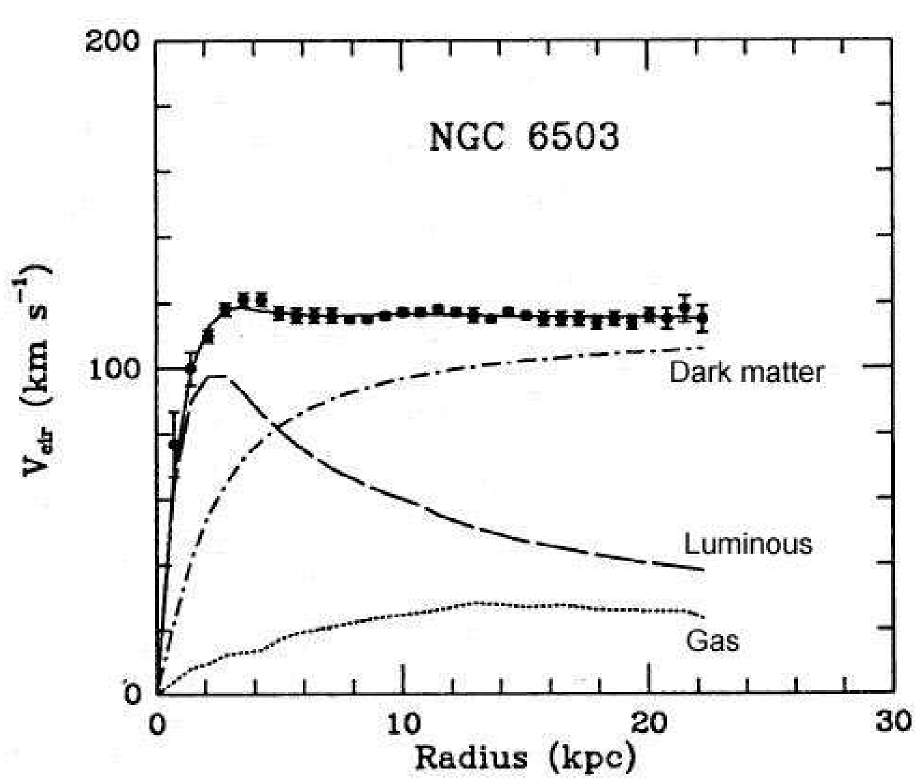

Figure 3.1 An example of a galaxy rotation curve. The solid line is the theoretical rotation curve and the dots with error bars the measured object speed. Also shown are the contributions made to the curve by gas, luminous matter and dark matter (BEGEMAN, 1991).

atures ($m_\chi \gg T$), the equilibrium density is exponentially suppressed $n_\chi \propto e^{-m_\chi/T}$. If thermal equilibrium was maintained, the number of WIMPs today would be infinitesimal. However, the Universe is not static, so today temperature of Universe is much lower than early times (GRIEST, 2000).

At high temperatures ($m_\chi \ll T$), the number density of DM's is very high and it is rapidly converting to lighter particles or lighter particles produce DM. Once temperature drops below DM mass ($m_\chi \gg T$), the number density of DM's drops exponentially and WIMPs cannot self-annihilate any more and they freeze-out from equilibrium, that is, their co-moving number density remains fixed. Under some simplifying assumptions (BERTONE, 2005), the relic abundance of WIMPs in the Universe (Ω_χ) can be simply expressed in terms of the self-annihilation cross-

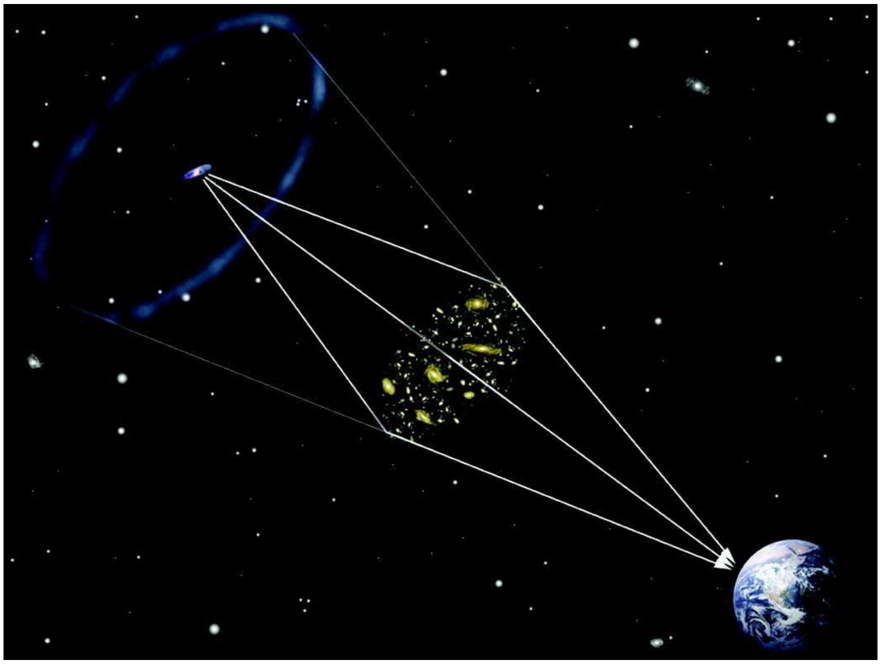

Figure 3.2 A cluster of galaxies with its huge mass of invisible dark matter makes an easily-identifiable gravitational lens, since it has so much mass that it bends light rays from other galaxies by about half a degree, producing a strong warp in their images. This artist's rendering of the process shows how multiple images of the same distant galaxy can be formed. This is often called "strong gravitational lensing. "A straight-through image, as well as several arrayed around an "Einstein ring" are formed. Note how the images of the source galaxy which appear around the Einstein ring are distorted stretched along the ring. This tangential distortion is readily visible in strong lensing, but it happens also in the general case where the lensing is so weak that it merely moves background galaxy images to a new place on the sky. In either case, computer analysis of the resulting background galaxy distortion patterns enables the mapping of the foreground mass concentrations (NASM).

section, $\sigma_A v$:

$$\Omega_\chi h^2 = \frac{m_\chi n_\chi}{\langle \sigma_A v \rangle} = \frac{3 \times 10^{-27} cm^3 s^{-1}}{\langle \sigma_A v \rangle} \tag{3.1}$$

where h is the Hubble parameter, which encodes the expansion rate of the Universe, the self-annihilation cross-section $\langle \sigma_A v \rangle = 3 \times 10^{-26} \mathrm{cm}^3 \mathrm{s}^{-1}$. Although in this simplified calculation the relic density does not depend strongly on the mass of the dark matter particle m_χ, the maximum and minimum annihilation cross-sections of the most common candidates do depend on it, therefore constraining the values of m_χ (in GeV) to the range $10 \leq m_\chi \leq 10^5$ (BERTONE, 2005).

Figure 3.4 shows numerical solutions to the Boltzmann equation which de-

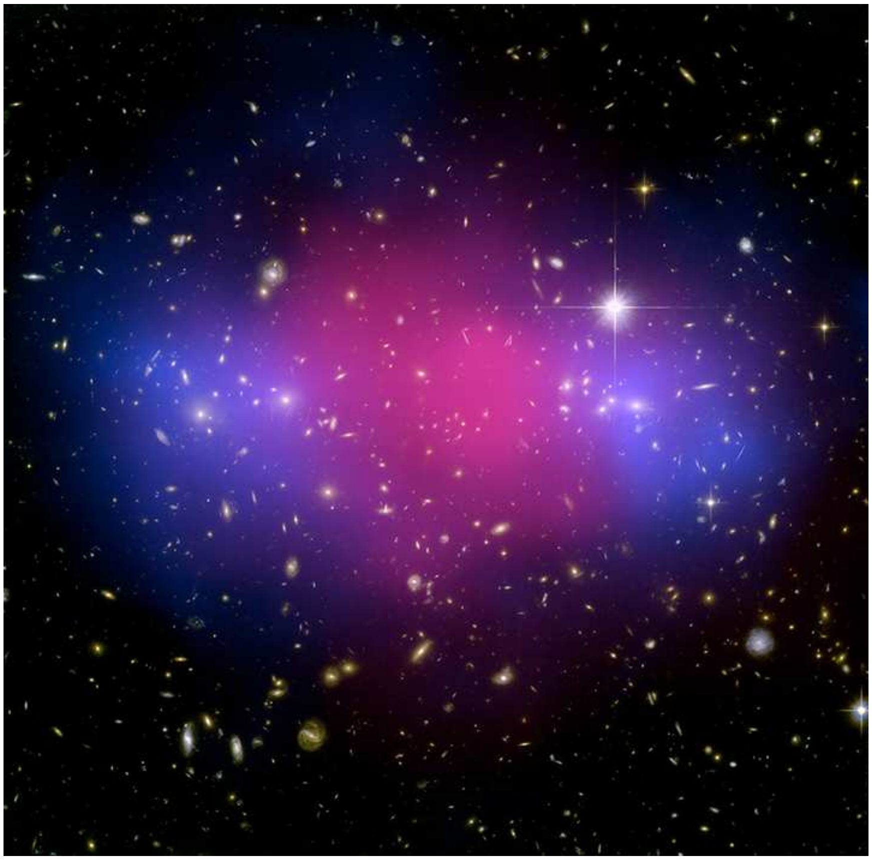

Figure 3.3 A powerful collision of galaxy clusters has been captured with NASA's Chandra X-ray Observatory and Hubble Space Telescope. Like its famous cousin, the so-called Bullet Cluster, this clash of clusters provides striking evidence for dark matter and insight into its properties. Like the Bullet Cluster, this newly studied cluster, officially known as MACSJ0025.4-1222, shows a clear separation between dark (blue) and ordinary matter (red). This helps answer a crucial question about whether dark matter interacts with itself in ways other than via gravitational forces (NASA-1, 2008).

termines the WIMP abundance. The equilibrium (solid line) and actual (dashed lines) abundances per comoving volume are plotted as a function of m_χ/T (which increases with increasing time). As the annihilation cross section is increased the WIMPs stay in equilibrium longer, and we are left with a smaller relic abundance.

Because WIMPs may only interact through gravitational and weak forces, they are extremely difficult to detect. However, there are many experiments underway to attempt to detect WIMPs both directly and indirectly. Although predicted scattering rates for WIMPs from nuclei are significant for large detector target masses, prediction that halo WIMPs may, as they pass through the Sun, interact with solar

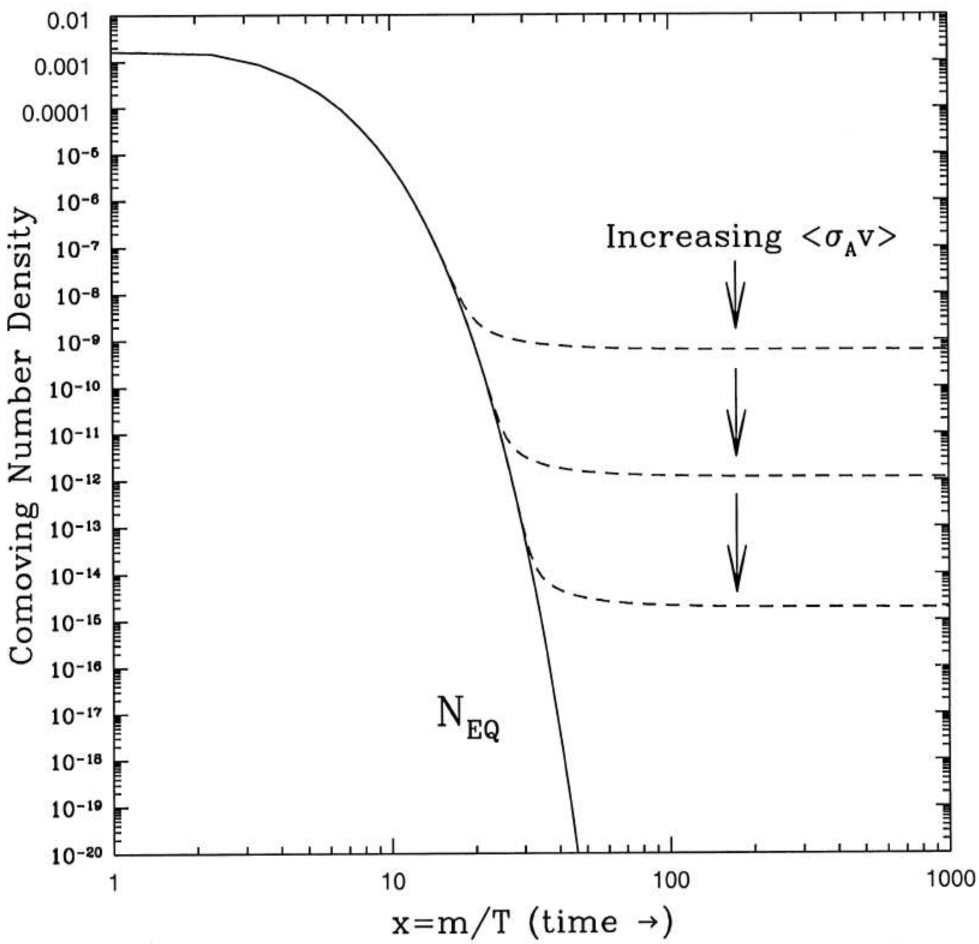

Figure 3.4 Comoving number density of a thermal relic WIMP in the early Universe. The dashed curves indicate the expected abundance, and the solid curve is the equilibrium abundance.

protons and helium nuclei. Such an interaction would cause a WIMP to lose energy and become ”captured” by the Sun. As more and more WIMPs thermalize inside the Sun, they begin to annihilate with each other, forming a variety of particles including high-energy neutrinos (BENVENUTI, 1975). These neutrinos may then travel to the Earth to be detected in one of the many neutrino telescopes, such as the Super-Kamiokande detector in Japan. The number of neutrino events detected per day at these detectors depends upon the properties of the WIMP, as well as on the mass of the Higgs boson. Similar experiments are underway to detect neutrinos from WIMP annihilations within the Earth (JUNGMAN, 1994) and from within the galactic center (REID, 1993).

Although the existence of WIMPs in nature is hypothetical at this point, it would resolve a number of astrophysical and cosmological problems related to dark matter. The main theoretical characteristics of a WIMP are:

Interaction only through the weak nuclear force and gravity, or at least with interaction cross-sections no higher than the weak scale;

Large mass compared to standard particles (WIMPs with sub-GeV masses may be considered to be light dark matter).

Because of their lack of interaction with normal matter, they would be dark and invisible through normal electromagnetic observations. Because of their large mass, they would be relatively moving slowly and therefore cold (ZACEK, 2007). As a result they would tend to remain clumpy. Simulations of a Universe full of cold dark matter produce galaxy distributions that are roughly similar to that which is observed (CONROY, 2006). WIMPs are considered one of the main candidates for cold dark matter, the others being massive compact halo objects (MACHOs) and axions. (These names were deliberately chosen for contrast, with MACHOs named later than WIMPs (GRIEST, 1991).) Also, in contrast to MACHOs, there are no known stable particles within the standard model of particle physics that have all the properties of WIMPs. The particles that have little weak interaction with normal matter, such as neutrinos, are all very light, and hence would be fast moving or hot. Hot dark matter would smear out the large-scale structure of galaxies and thus is not considered a viable cosmological model. WIMP-like particles are predicted by R-parity-conserving supersymmetry, a popular type of extension to the standard model, although none of the large number of new particles in supersymmetry have been observed.

3.3 Detection of WIMPs and Current Limits

To detect WIMPs there are many experiments which are classified with their detection methods.

Figure 3.5 shows that classification of those experiments to detect WIMPs. In all idea DM interact with SM particles.

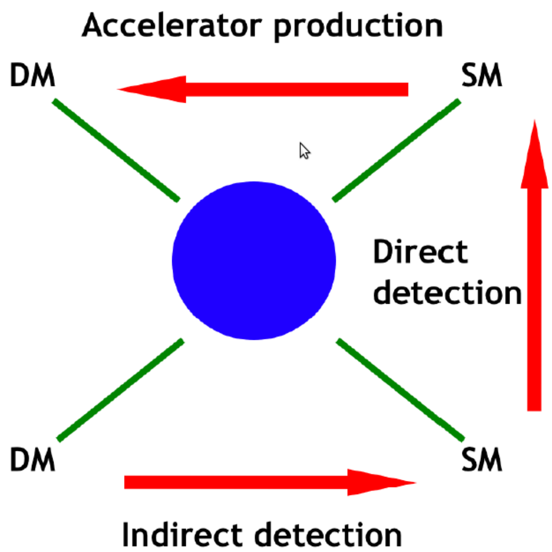

Figure 3.5 Feyman digaram of different ideas for DM particle detection. Depending on the direction of the time axis, different type of a search can be recognized. SM stands for the Standard Model particle, DM for the dark matter particle (MIJAKOWSKI, 2011).

3.3.1 Direct Detection

If WIMPs exist within our galaxy then many of WIMPs must pass through the Earth. The experimental idea of direct detection is based on the observation of WIMP scattering with nuclei. The expected recoils energy is depend on WIMP mass and type of nuclei which is used in the detector. Since the expected number of WIMP-nuclei scattering is very low the experiments is very sensitive to backgrounds which are mostly produced via cosmic rays and radioactivity. The experiments typically operate in deep underground laboratories to reduce the background from cosmic rays and natural radioactivity.

Figure 3.6 shows that various experimental methods which are using different detection techniques. Each techniques are using different nuclei to perform their best method. Figure 3.7 presents current results of various direct detection experiments.

Given the low velocity and subsequent momentum transfer in interations between the WIMPs and nuclei in a direct detection experiment, the dominant interaction mechanism is expected to be elastic scattering due to spin-independent interactions.

For spin-independent scattering, WIMP-nucleus cross section is approximately proportional to the WIMP-proton scattering cross-section. This relationship emphasizes the dependence of the interaction rate on the size of the nucleus A. Of course, one could consider other mechanisms that may contribute to the interaction cross-section such spin- dependent interaction terms. In that case, the dependence on the target's nuclear properties is proportional to the total spin J rather than A^2. All of the other factors relevant to calculating the interaction rate are unchanged (T.Saab, 2012).

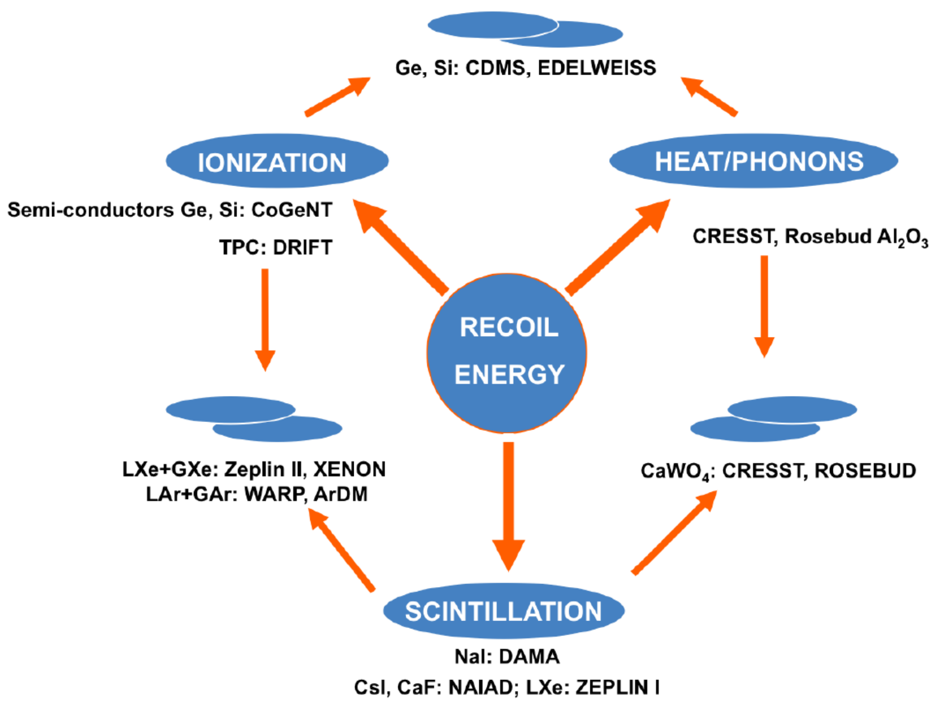

Figure 3.6 Shematic view of classification of various direct detection experiments methods to measure recoil energy (MIJAKOWSKI, 2011).

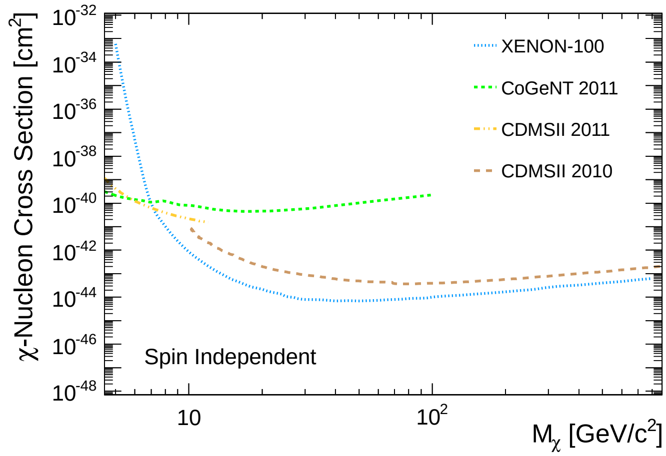

Figure 3.7 WIMP nucleon cross section vs Dark Matter mass for various direct detection experiments.

3.3.2 Indirect Detection

Indirect detection experiments search for the products of WIMP annihilation. In this search the value of DM self-annihilation cross section is constrained (MIJAKOWSKI, 2011). If WIMPs are Majorana particles (the particle and antiparticle are the same) colliding of two WIMPs could annihilate to produce gamma rays or particle-antiparticle pairs. This could produce a significant number of gamma rays, antiprotons or positrons in the galactic halo. The detection of such a signal is not conclusive evidence for dark matter, as the production of gamma rays from other sources are not fully understood. The most recent indirect detection experiment results from iceCube and Super-Kamiokande can be found at reference (ABBASI, 2012 and TANAKA, 2011).

3.3.3 Collider Detection

Recently, there has been considerable interest in searches for the production of dark matter at the LHC using one of the more model-independent signatures of a single energetic jet with large missing energy. In the present analysis, we have interpreted our results in the context of two models, (HARNIK, 2010) and

(BELTRAN, 2010). Both models work in the context of an effective field theory framework, assuming that the interactions between the dark matter and Standard Model particles are mediated by very heavy particles. Here, we consider models in which the dark matter particle χ is a Dirac fermion and set bounds on the production of dark matter with mass between 1 and 1000 GeV where the dark matter couplings are vector and axial-vector mediated interactions with up and down quarks. The following effective operators have been considered (HARNIK, 2010),

$$O_V = \frac{(\bar{\chi}\gamma_\mu\chi)(\bar{q}\gamma^\mu q)}{\Lambda^2}, \qquad \text{(vector, } s\text{-channel)} \tag{3.2}$$

$$O_{AV} = \frac{(\bar{\chi}\gamma_\mu\gamma_5\chi)(\bar{q}\gamma^\mu\gamma_5 q)}{\Lambda^2}, \qquad \text{(axial vector, } s\text{-channel)} \tag{3.3}$$

where $\Lambda = M/\sqrt{g_\chi g_q}$, with M denoting the mass of the mediator, g_χ and g_q its coupling to dark matter and Standard Model quarks respectively.

Previous collider searches in the monojet plus missing transverse momentum channel have been interpreted in (HARNIK, 2010) and translated into limits on the dark-matter nucleon scattering cross-section which can be compared with those from dedicated direct detection experiments. The LHC bounds were found to be the most powerful for low mass dark matter and spin dependent couplings with a heavy mediator.

The pair production of dark matter particles at a hadron collider can occur through a diagram like that in Figure 3.8, where the emission of a single jet in the initial state and the interpretation of the dark matter particles as missing energy would manifest itself as an excess of events in the monojet topology.

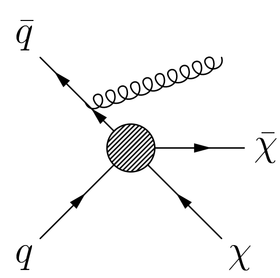

Figure 3.8 The pair production of dark matter particles in association with a single jet in a hadron collider.

We use MadGraph to evaluate the acceptance of the vector and axial-vector couplings to up and down quarks for our monojet event selection, setting the mediator mass to a very large value and varying the dark matter mass between 1 GeV and 1000 GeV. We present limits on the cross-section and show that these can be translated to bounds on Λ and the dark matter-nucleon scattering cross-section which can be compared to the direct detection limits.

4. THE SEARCH FOR MONOJET

This thesis describes a search for new physics in the missing energy plus single jet final state, with collisions at a centre-of-mass energy of 7 TeVprovided by the Large Hadron Collider (LHC) at CERN. The data were collected from March to November 2011 by the Compact Muon Solenoid (CMS) experiment, and correspond to an integrated luminosity of $5\,\mathrm{fb}^{-1}$.

The analysis is an update of previous work (CMS AN-11-024, 2011) and follows the same format as AN-11-024, beginning with trigger efficiency of data in Section 4.1, followed by details of the data, signal and background samples in Section 4.2. The trigger and offline selection are presented in Section 4.3 and the impact of the major systematic effects on signal is discussed in Section 4.5. A data-driven estimation of the most relevant backgrounds is made in Section 4.4. The results are interpreted in the context of new physics models in Section 4.6 and conclusions follow in Section 4.7.

Small changes have been made to the analysis from the previous result. These are described as follows:

- The threshold for the $E_{\mathrm{T}}^{\mathrm{miss}}$ in our trigger was increased from 80 GeV to 95 GeV in the latter half of data taking. However, the trigger is still almost fully efficient for our previous jet p_{T} cut of 110 GeV and $E_{\mathrm{T}}^{\mathrm{miss}}$ cut of 200 GeV, so these remain unchanged.

- The monojet event selection is almost identical to that in the previous result. A small change was made in the criteria used to select electrons for the lepton veto. Previously, the multi variate analysis (MVA) cut was used to select particle flow (PF) electrons, however now the standard vector boson task force 80% working point (WP80) is used. Since the monojet sample is already depleted in electrons, this change has little effect.

- The method for calculating the $W_{l^{\pm}\nu} + jets$ background includes more details as compared to the previous analysis. We use the $W_{\mu^{\pm}\nu} + jets$ control sample and correct for the inefficiencies of the detector acceptance and lepton selection to obtain the number of remaining $W_{l^{\pm}\nu}+jets$ events where the electron or muon is 'lost'. Whereas the final $W_{l^{\pm}\nu}+jets$ estimate is the same as that using the method from the previous analysis, we have explicitly stated the (in)efficiency factors that are used in the calculation and included a breakdown of the estimated background in the electron and muon channels and into events in which the lepton is out of the acceptance or not reconstructed/isolated.

- The results have been interpreted in the context of the ADD model as before. In addition to these models, the results have also been interpreted in the context of dark matter models predicting the pair production of dark matter particles and the emission of a jet from the initial state.

4.1 Trigger and Data Samples

The data for this search was collected using `HLT_CentralJet80_MET80` for the earlier half of the year and `HLT_CentralJet80_MET95` for the 2011B running. The triggers require a Level 1 seed with $E_{\mathrm{T}}^{\mathrm{miss}}$ larger than 30 GeV (`L1_ETM30`).

At the high level trigger (HLT), the primary requirements for the $E_{\mathrm{T}}^{\mathrm{miss}}$ and leading jet (j_1) are as follows:

$$E_{\mathrm{T}}^{\mathrm{miss}} > 80,95GeV \tag{4.1}$$

$$p_{\mathrm{T}}(j_1) > 80GeV \tag{4.2}$$

$$|\eta(j_1)| < 2.6 \tag{4.3}$$

$$\mathrm{EMF}(j_1) > 0.01 \tag{4.4}$$

The trigger turn-on curves as a function of $E_{\mathrm{T}}^{\mathrm{miss}}$ and the p_{T} of the leading jet is shown in Figure 4.1. The trigger efficiency is calculated from an independent sample of events collected using the `HLT_Mu30` or `HLT_Mu40` trigger path (the latter unprescaled path was used when the former became prescaled). A two-dimensional plot of the trigger efficiency for `HLT_CentralJet80_MET80` is shown as a function

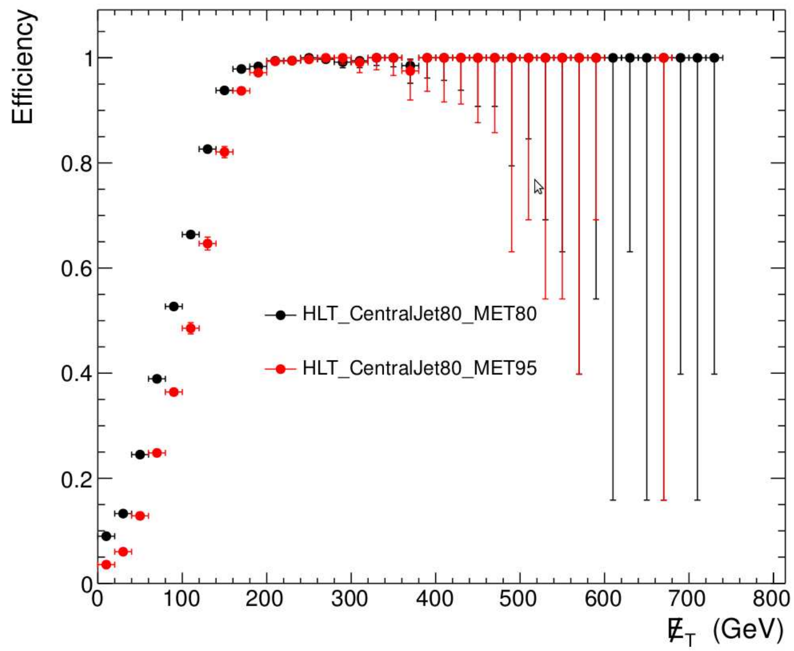

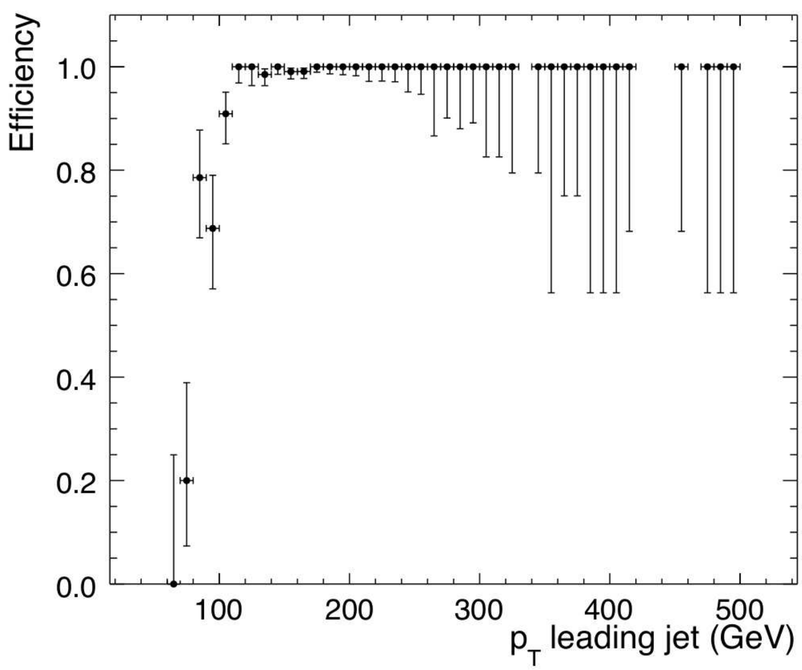

Figure 4.1 Trigger efficiency turn-on curve for `HLT_CentralJet80_MET80` and `HLT_CentralJet80_MET95` as a function of E_T^{miss} and p_T of the leading jet.

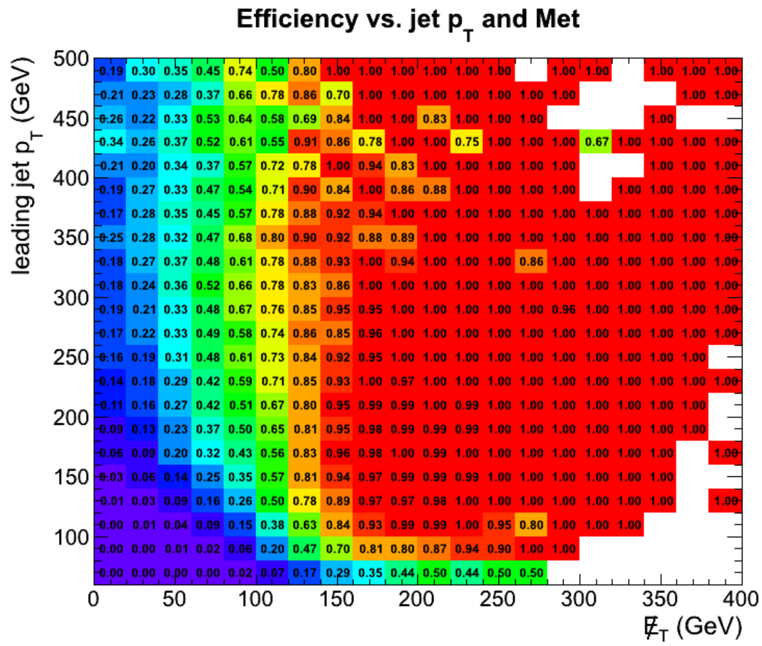

Figure 4.2 The trigger efficiency for `HLT_CentralJet80_MET80` as a function of the E_T^{miss} and p_T of the leading jet.

Table 4.1 Datasets used in this analysis, with integrated luminosity of 5.0 fb^{-1}.

Year	Run Range	DBS Location	Int. Lumi. [pb^{-1}]
2011A	160404 - 163869	/METBTag/Run2011A-May10ReReco-v1	230
2011A	165088 - 167913	/MET/Run2011A-PromptReco-v4	995
2011A	170249 - 172619	/MET/Run2011A-Aug05ReReco	396
2011A	172620 - 173692	/MET/Run2011A-PromptReco-v6	700
2011B	175832 - 179431	/MET/Run2011B-PromptReco-v1	2659

of the E_T^{miss} and leading jet p_T in Figure 4.2. The plots show that the triggerpaths becomes fully efficient at $\sim$110 GeV for $p_T(j_1)$ and $\sim$200 GeV for E_T^{miss}.

The data are reconstructed with the `CMSSW_4_2_8` release. The good-run list and luminosity have been obtained by using the JSON files listed in (JSON, 2011), with all subsystems marked “GOOD”.

The data is collected on a combination of METBTag and MET primary datasets, and the specific data reprocessing and luminosity used in this analysis is listed in Table 4.1.

4.2 Signal and Background MC Samples

The ADD-model signals are produced with the PYTHIA 8.130 Monte Carlo (MC) generator (SJOSTRAND, 2008). We use the current default PYTHIA8 tune (4C). The CTEQ-6.6 Parton Density Functions (PDF) (PUMPLIN, 2002) were used for ADD.

Details of the PYTHIA8 signal samples used for ADD are given in (APPENDIX A). The cross sections have $\hat{p}_T > 80\,\mathrm{GeV}$. The next-to-leading order QCD corrections to the graviton plus jet production are sizable (KARG, 2010) and dependent on the p_T of the recoiling parton. As a simple approach we choose K-factors of 1.5 for $\delta = 2,3$ and 1.4 for $\delta = 4,5,6$.

The dark matter signal samples were produced using MADGRAPH for vector couplings to up and down quarks (V-u, V-d) and axial-vector couplings to up and down quarks (AV-u, AV-d), for M_χ ranging between 0.01 and 1000 GeV. The details of this production are shown in (APPENDIX A).

The primary Standard Model processes considered include QCD, top quark pair production, and the production of W or Z in association with jets. MC simulation samples used in this analysis to model the backgrounds are listed in (APPENDIX B).

The $Z_{l^+l^-} + jets$ MADGRAPH sample contains only events where the Z boson decays into electrons, muons or taus. The $Z_{\nu\bar{\nu}} + jets$ MADGRAPH sample contains only events where the Z boson decays into the three generations of neutrinos. The hadronization and fragmentation of quarks and gluons (along with the underlying event) are performed using PYTHIA with the MLM shower matching prescription (HOUCHE, 2006) to avoid double counting due to the parton showering, and the PYTHIA Tune Z2 (WEB REF-1) is used for each sample, unless otherwise specified.

Pile-up effects have been included and the MC samples have been reweighted according to the 3D pileup reweighting scheme (CMS Twiki-3). The effect of the pileup reweighting can be seen in Figure 4.3 where a comparison is made after basic selection cuts ($E_{\mathrm{T}}^{\mathrm{miss}} > 350\,\mathrm{GeV}$, noise cleaning, $p_{\mathrm{T}}(j_1) > 110\,\mathrm{GeV}/c$,

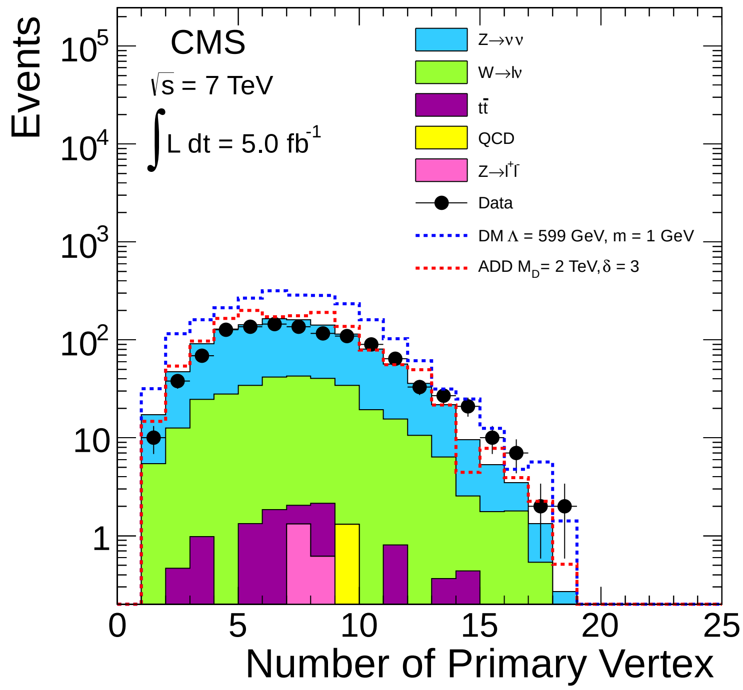

Figure 4.3 Effect of pile-up re-weighting scheme on MC simulation, compared with data.

$|\eta(j_1)| < 2.4$, $\mathrm{N_{Jets}} \leq 2$, $\Delta\Phi(j_1, j_2) < 2.5$, and no $p_T(e \text{ or } \mu) > 10\,\mathrm{GeV/c}$).

4.3 Event Selection

We describe below the set of criteria used to select monojet events.

The real data events passing the above mentioned trigger are required to pass a set of event cleaning cuts. Events are required to have at least one primary vertex (CMS TRK-10-005, 2010) reconstructed within a ± 24 cm window along the beam axis around the detector center, and a transverse distance from the beam axis of less than 2 cm. Signals in the calorimeter that are not associated with pp interactions are identified based either on energy sharing between neighboring channels or timing requirements and are excluded from further reconstruction (CMS JME-10-004, 2010).

To suppress the remaining instrumental and beam-related backgrounds, events are rejected if less than 20% of the energy of the highest p_{T} jet is carried by charged hadrons or more than 70% of this energy is carried by either neutral hadrons or pho-

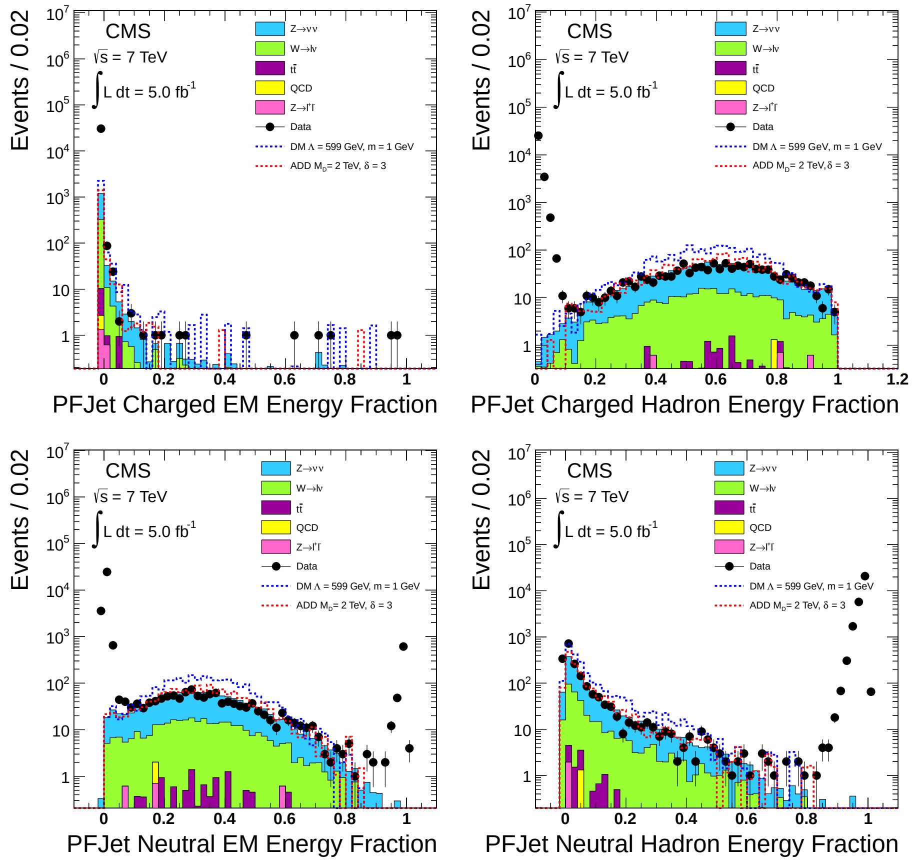

Figure 4.4 Hadronic and electromagnetic energy fractions from charged and neutral particles, before cleanup cuts on these quantities are applied, with SM normalised to the data. We require the charged hadronic fraction of the jet to be above 20% and the neutral hadronic, neutral electromagnetic and charged electromagnetic fractions to be below 70% of the total jet energy.

tons. Events are also rejected if more than 70% of the p_{T} of the second highest p_{T} jet is carried by neutral hadrons. Such spurious jets primarily arise from instrumental noise, where the energy deposition is limited to one sub-detector. Jets resulting from energy deposition by beam halo or cosmic-ray muons do not have associated tracks and are also rejected by these selections. All events passing these selection requirements and with $E_{\mathrm{T}}^{\mathrm{miss}} > 500$ GeV/c were visually inspected and found to be consistent with pp collision events. The distributions for the neutral and charged energy fractions of the leading jet before and after the cuts are shown in Figure 4.4 and Figure 4.5. The application of these data cleanup requirements would reject approximately 2% of the dark matter signal and 3% of the ADD signal. Detail of

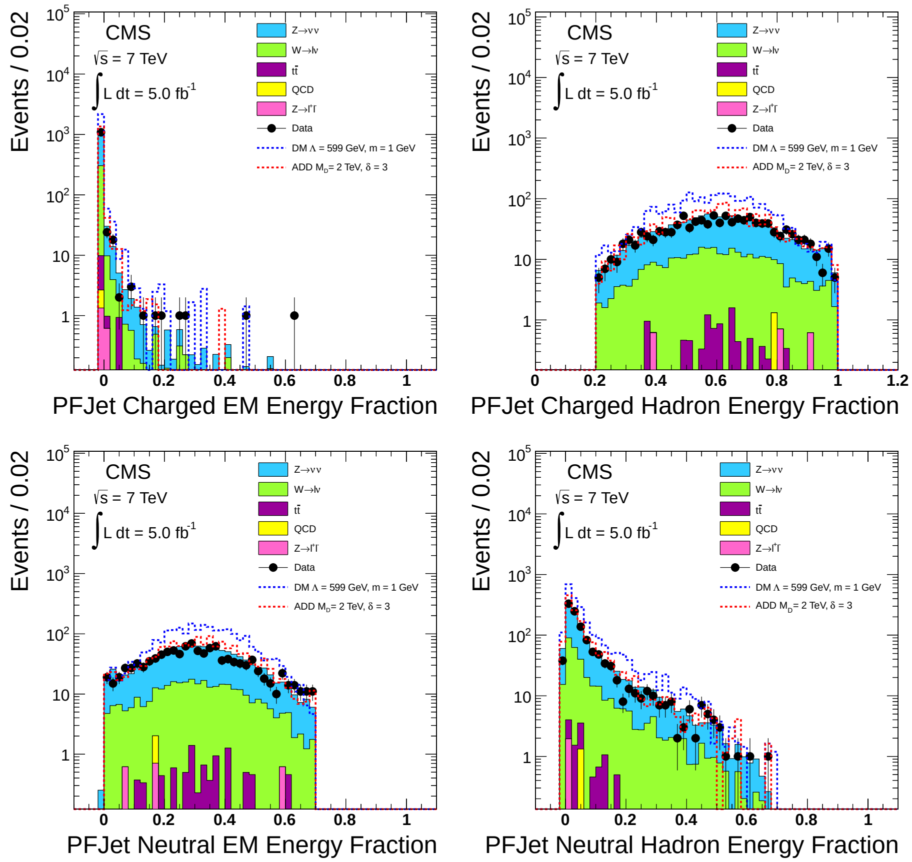

Figure 4.5 Hadronic and electromagnetic energy fractions from charged and neutral particles, after cleanup cuts on these quantities are applied, with SM normalised to the data.

rejection can be seen in Table 4.2 for each cut. Jets and $E_{\mathrm{T}}^{\mathrm{miss}}$ are reconstructed

Table 4.2 Cut Efficiency table for data, backgrounds and both ADD M_D=2 TeV, δ=3 and Dark Matter Λ=599 GeV, m=1 GeV signals.

	DATA(%)	Backgrounds(%)	ADD(%)	Dark Matter(%)
$E_{\mathrm{T}}^{\mathrm{miss}}>200$ GeV/c	88.9	85.3	58.6	93.1
Noise Clean	88.3	3.8	2.7	2.1
$p_{\mathrm{T}}(\mathrm{j}_1) > 110\,\mathrm{GeV/c}$	2.3	6.0	5.0	4.2
$N_{\mathrm{Jet}}(p_{\mathrm{T}} > 30\,\mathrm{GeV/c}) \leq 2$	32.2	32.8	32.4	30.7
$\Delta\phi(\mathrm{j}_1,\mathrm{j}_2) < 2.5$	34.3	42.2	10.1	7.5
Lepton Veto	13.6	10.7	5.5	5.6

using a particle flow technique (CMS PFT-09-001, 2009). The algorithm produces a unique list of particles in each event, using the combined information from all CMS subdetectors. This list is then used as input to the jet clustering, which reconstructs jets using the anti-k_{T} algorithm (CACCIARI, 2008) with a distance parameter of 0.5. The missing transverse energy vector is computed as the negative vector sum of the transverse momenta of all particles reconstructed in the event.

Jet energies are corrected to establish a uniform calorimeter response in η and an absolute response in p_T calibrated at the particle level. Jet-energy-scale corrections are derived from MC simulation, and a residual correction is derived from the data by measuring the p_T balance in dijet events (CMS JME-10-010, 2010).

The signal sample is selected by requiring $E_{\mathrm{T}}^{\mathrm{miss}} > 200$ GeV/c and the jet with the highest transverse momentum (j_1) to have $p_{\mathrm{T}}(\mathrm{j}_1) > 110$ GeV/c and $|\eta(\mathrm{j}_1)| < 2.4$. The triggers used to collect these data are fully efficient for events passing these selection cuts. Events with more than two jets ($N_{\mathrm{jets}} > 2$) with p_{T} below 30 GeV/c are discarded.

As signal events typically contain jets from initial- or final-state radiation, a second jet (j_2) is allowed, provided $\Delta\phi(\mathrm{j}_1,\mathrm{j}_2) < 2.5$. This angular requirement suppresses QCD dijet events. Approximately 60% of the selected events have two jets.

The $p_{\mathrm{T}}(j_1)$, $\eta(j_1)$, $\mathrm{N_{jets}}$ and $\Delta\phi(j_1, j_2)$ distributions are shown in Figure 4.6, for the signal region of $E_{\mathrm{T}}^{\mathrm{miss}} > 350\,\mathrm{GeV}$.

To reduce background from Z and W production and top-quark decays, lepton candidates (electron and muon) are required to have $p_{\mathrm{T}} > 10\,\mathrm{GeV/c}$, to originate within 2 mm of the beam axis in the transverse plane, and to be spatially separated from jets by at least $\Delta\mathrm{R} = \sqrt{(\Delta\eta)^2 + (\Delta\phi)^2} = 0.3$ in order to remove leptons faking jets. Here, $\Delta\eta$ and $\Delta\phi$ are the pseudorapidity and azimuthal angle difference between the lepton track and other reconstructed tracks (hits in the calorimeter), respectively.

Muon candidates within $|\eta| < 2.1$ and electron candidates within $|\eta| < 1.44$ or $1.56 < |\eta| < 2.5$ (to avoid poorly-instrumented regions) are identified with the particle flow technique (CMS PFT-09-001, 2009).

The lepton candidates are also required to be isolated and the relative combined isolation R is defined as the sum of the p_{T} of the charged hadrons, neutral hadrons and photon contributions computed in a cone of radius 0.4 around the lepton direction, divided by the lepton p_{T},

$$R = \frac{\Sigma_i[p_{Ti}(chargedHadron) + p_{Ti}(neutralHadron) + p_{Ti}(Photon)]}{p_T}. \tag{4.5}$$

Electron and muon candidates with R below 0.20 are considered isolated. An electron candidate is further identified using the standard Vector Boson Task Force WP80. A muon candidate is additionally required to satisfy the following criteria:

- Global and Tracker,
- χ^2/ndof < 10,
- Tracks associated to muons must satisfy:
  - at least one pixel hit,
  - at least ten total hits (strip + pixel),
  - at least two matches in the muon stations.

Remaining events with an isolated track are eliminated, as they come primarily from τ decays. To measure the isolation, a hollow cone $0.02 < \Delta\mathrm{R} < 0.3$ is defined around each track with $p_{\mathrm{T}} > 10\,\mathrm{GeV}$. The scalar sum of the p_T of all tracks with $p_{\mathrm{T}} > 1\,\mathrm{GeV}$ inside the cone is calculated and the event is vetoed if this sum is smaller than 1% of the p_T of the original track. The distribution of the track isolation veto (TIV) ratio is shown in Figure 4.7 for data, the SM backgrounds and a representative signal point for the ADD and dark matter models. The distribution of $E_{\mathrm{T}}^{\mathrm{miss}}$ for data and background after all selections is shown in Figure 4.8. We define the above described event selection with the $E_{\mathrm{T}}^{\mathrm{miss}}$ cut of 200 GeV as the baseline selection and subsequently apply tighter $E_{\mathrm{T}}^{\mathrm{miss}}$ selections of $E_{\mathrm{T}}^{\mathrm{miss}} = 250, 300, 350, 400$ to obtain our search regions. Optimisation studies have been performed for each of our signal samples to find the value of the $E_{\mathrm{T}}^{\mathrm{miss}}$ cut that gives the best expected limit. The study is documented in (APPENDIX C). For both the ADD and dark matter signal points, the optimal $E_{\mathrm{T}}^{\mathrm{miss}}$ cut is found to be 350 GeV.

Table 4.3 lists the numbers of data and SM background events at each step of the analysis. Efficiencies for representative dark matter and ADD models relative to

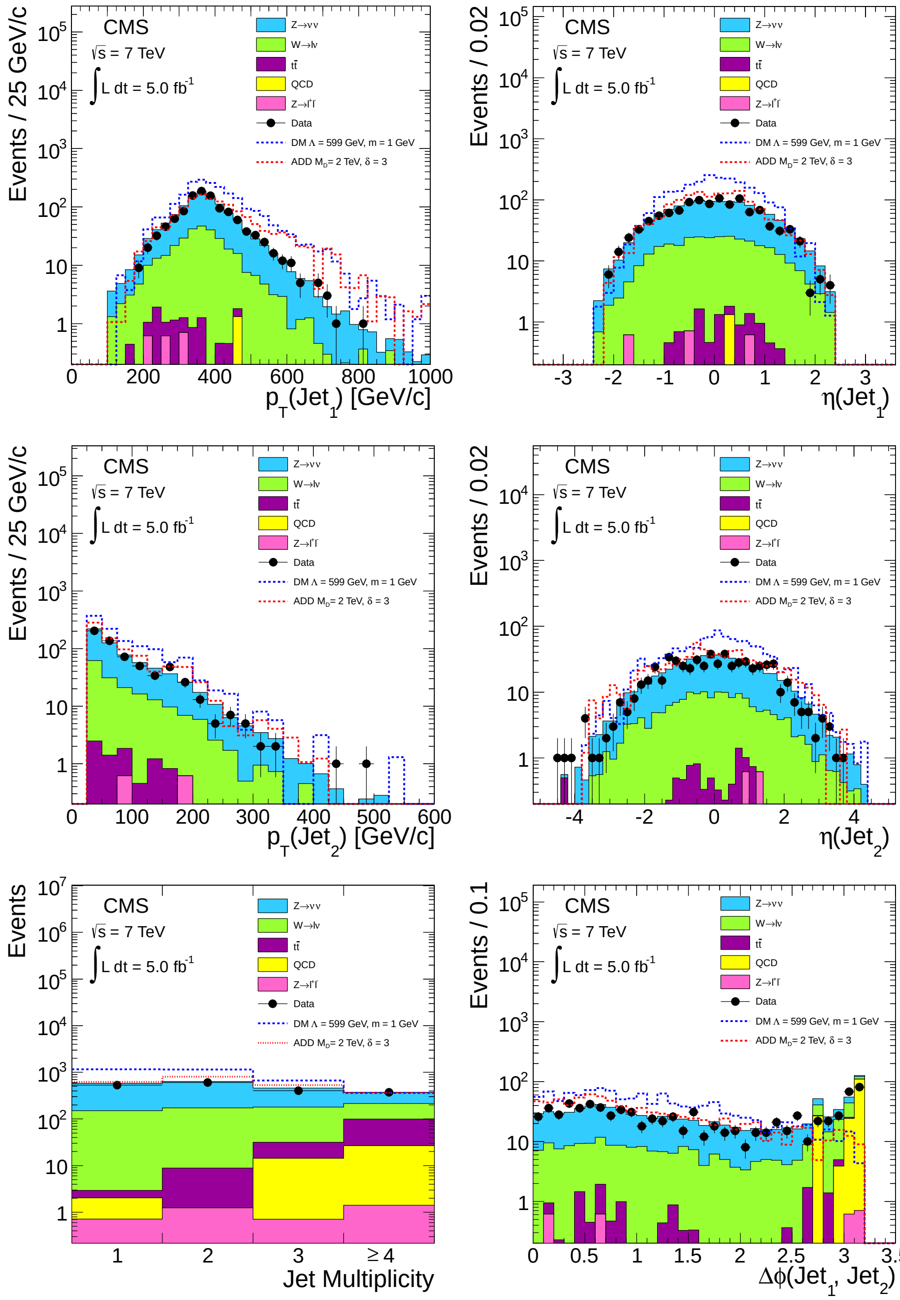

Figure 4.6 Plots of basic selection variables for jets. The figures are shown with all analysis cuts applied, and for $E_T^{miss} > 350\,\mathrm{GeV}$. SM backgrounds are normalised to data where available.

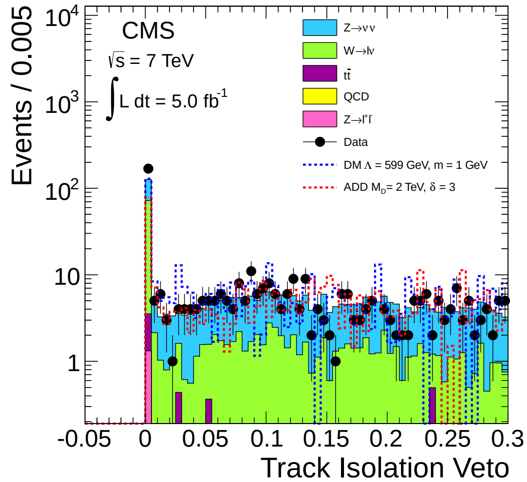

Figure 4.7 Additional cleanup variables investigated. We reject events with muons or electrons above 10 GeV and apply the TIV as described in the text.

the event yield passing $E_{\mathrm{T}}^{\mathrm{miss}} > 200\,\mathrm{GeV/c}$ selection are also shown. The dominant background is $Z_{\nu\bar{\nu}} + jets$ and the next largest source of background is $W_{\mu^{\pm}\nu} + jets$. The event yields for $E_{\mathrm{T}}^{\mathrm{miss}} > 250$, 300, 350, and 400 GeV/c are also shown.

The $E_{\mathrm{T}}^{\mathrm{miss}}$and $p_{\mathrm{T}}(\mathrm{j}_1)$ distributions are shown in Figure 4.8, where the $Z_{\nu\bar{\nu}} +$ $jets$ and $W_{\mu^{\pm}\nu} + jets$ backgrounds are normalized to the rate determined from data (data driven) and other backgrounds are normalized to the integrated luminosity.

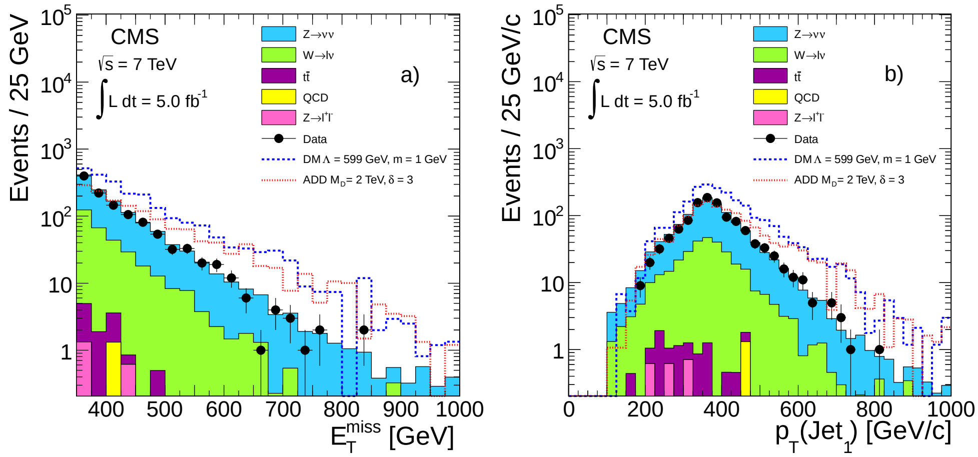

Figure 4.8 The distribution of (a) $E_{\mathrm{T}}^{\mathrm{miss}}$and (b) $p_{\mathrm{T}}(\mathrm{j}_1)$ for data (black full points with error bars) and simulation (histograms) for $E_{\mathrm{T}}^{\mathrm{miss}} > 350$ GeV/c after the full event selection criteria are applied. The $Z_{\nu\bar{\nu}} + jets$ and $W_{l^{\pm}\nu} + jets$ backgrounds are normalized to their estimates from data. An example of a dark matter signal (for axial-vector couplings and $M_{\chi} = 1\,\mathrm{GeV/c^2}$) is shown as a dashed blue histogram and an ADD signal (with $M_{\mathrm{D}} = 2\,\mathrm{TeV}$, $\delta = 3$) is shown as a dotted red histogram.

Table 4.3 Event yields at different stages of the event selection for (a) various SM processes from simulation, (b) sum of all SM processes, and the data, corresponding to an integrated luminosity of $5.0\,\mathrm{fb}^{-1}$. Only statistical uncertainties are shown, which in most cases are smaller than the associated systematic uncertainties. Lepton removal eliminates events with isolated electrons, muons, or tracks with $p_{\mathrm{T}} > 10\,\mathrm{GeV/c}$. Efficiencies for representative dark matter and ADD models relative to the event yield passing $E_{\mathrm{T}}^{\mathrm{miss}} > 200\,\mathrm{GeV/c}$ selection are also given.

(a)

Requirement	$Z(\nu\bar{\nu})$ $+jets$	$W(e\nu,\mu\nu,\tau\nu)$ $+jets$	$Z(\ell\ell)$ $+jets$	$t\bar{t}$	Single t	QCD Multijet
$E_{\mathrm{T}}^{\mathrm{miss}}$>200 GeV/c	$(324\pm1)\times10^2$	$(591\pm1)\times10^2$	5255 ± 47	$(133\pm1)\times10^2$	1165 ± 7	$(160\pm1)\times10^2$
$p_{\mathrm{T}}(\mathrm{j}_1) > 110\,\mathrm{GeV/c}$	$(302\pm1)\times10^2$	$(557\pm1)\times10^2$	4908 ± 45	$(119\pm1)\times10^2$	1035 ± 6	$(158\pm1)\times10^2$
$N_{\mathrm{Jet}}(p_{\mathrm{T}} > 30\,\mathrm{GeV/c}) \leq 2$	$(227\pm1)\times10^2$	$(397\pm1)\times10^2$	3453 ± 38	1587 ± 20	274 ± 3	5296 ± 14
$\Delta\phi(\mathrm{jet}_1,\mathrm{jet}_2)$ <2.5	$(211\pm1)\times10^2$	$(354\pm1)\times10^2$	3139 ± 36	1344 ± 19	237 ± 3	62 ± 5
Lepton Removal	$(198\pm1)\times10^2$	$(97\pm1)\times10^2$	81 ± 6	214 ± 7	35 ± 1	2 ± 1
$E_{\mathrm{T}}^{\mathrm{miss}}$>250 GeV/c	7306 ± 23	2951 ± 19	22 ± 3	70 ± 4	10 ± 0.5	2 ± 1
$E_{\mathrm{T}}^{\mathrm{miss}}$>300 GeV/c	2932 ± 14	967 ± 11	6 ± 1.7	23 ± 2	3 ± 0.2	1 ± 0.7
$E_{\mathrm{T}}^{\mathrm{miss}}$>350 GeV/c	1308 ± 9	362 ± 7	2 ± 0.9	9 ± 1.6	1 ± 0.2	1 ± 0.7
$E_{\mathrm{T}}^{\mathrm{miss}}$>400 GeV/c	628 ± 7	148 ± 4	1 ± 0.4	3 ± 0.8	0.4 ± 0.1	1 ± 0.7

(b)

Requirement	Total Simulated SM	Data	DM (%) $M_\chi = 1\,\mathrm{GeV/c^2}$	ADD (%) M_{D}=2 TeV/c^2,$\delta = 3$
$E_{\mathrm{T}}^{\mathrm{miss}}$>200 GeV/c	1273×10^2	1045×10^2	100.0	100.0
$p_{\mathrm{T}}(\mathrm{j}_1) > 110\,\mathrm{GeV/c}$	1195×10^2	1007×10^2	95.2 ± 0.71	92.8 ± 1.03
$N_{\mathrm{Jet}}(p_{\mathrm{T}} > 30\,\mathrm{GeV/c}) \leq 2$	730×10^2	624×10^2	69.8 ± 0.60	61.5 ± 0.84
$\Delta\phi(\mathrm{j}_1,\mathrm{j}_2)$ <2.5	613×10^2	538×10^2	66.8 ± 0.59	58.0 ± 0.81
Lepton Removal	298×10^2	238×10^2	63.7 ± 0.58	54.8 ± 0.79
$E_{\mathrm{T}}^{\mathrm{miss}}$>250 GeV/c	104×10^2	76×10^2	34.1 ± 0.42	32.5 ± 0.61
$E_{\mathrm{T}}^{\mathrm{miss}}$>300 GeV/c	3932	2774	18.9 ± 0.31	19.9 ± 0.48
$E_{\mathrm{T}}^{\mathrm{miss}}$>350 GeV/c	1683	1142	10.8 ± 0.24	12.5 ± 0.38
$E_{\mathrm{T}}^{\mathrm{miss}}$>400 GeV/c	782	522	6.4 ± 0.18	7.9 ± 0.30

4.4 Data Driven Background Estimation

Table 4.3 shows that the SM backgrounds remaining after the full event selection are dominated by the following processes: $Z_{\nu\bar{\nu}} + jets$ with the Z boson decaying into a pair of neutrinos and $W_{l^{\pm}\nu} + jets$ with the W boson decaying leptonically. These backgrounds are estimated from data utilizing a control sample of $\mu + jet$ events, where $Z_{\mu^+\mu^-} + jets$ events are used to estimate the $Z_{\nu\bar{\nu}} + jets$ background and $W_{\mu^{\pm}\nu} + jets$ events are used to estimate the remaining $W_{l^{\pm}\nu} + jets$ background. The control sample is derived from the same set of triggers as those used to collect the signal sample by applying the full event selection criteria except for the vetoes on electrons, muons, and isolated tracks. One or more isolated muons with $p_{\mathrm{T}} > 20$ GeV/c and $|\eta| < 2.1$ are required.

To obtain a sample of $Z_{\mu^+\mu^-} + jets$ events, two well reconstructed and isolated muons are required, with opposite sign charge and an invariant mass between 60 and 120 GeV. A sample of $W_{\mu^{\pm}\nu} + jets$ is similarly obtained by requiring one muon passing the selection criteria and with a reconstructed W transverse mass between 50 and 100 GeV.

Table 4.4 and Table 4.5 show the event yields and Figure 4.9, Figure 4.10, Figure 4.11 show the event distributions obtained for the $W_{\mu^{\pm}\nu} + jets$ and $Z_{\mu^+\mu^-} + jets$ control samples and the predicted backgrounds from MC.

Table 4.4 Event yields for the $Z_{\mu^+\mu^-} + jets$ data control samples and the backgrounds from MC.

	$Z_{l^+l^-} + jets$	$t\bar{t}$	Single t	All MC	Data
$E_{\mathrm{T}}^{\mathrm{miss}} > 200$	1803	15	2	1820	1537
$E_{\mathrm{T}}^{\mathrm{miss}} > 250$	707	5	1	713	593
$E_{\mathrm{T}}^{\mathrm{miss}} > 300$	318	2	0	320	235
$E_{\mathrm{T}}^{\mathrm{miss}} > 350$	135	0	0	135	111
$E_{\mathrm{T}}^{\mathrm{miss}} > 400$	68	0	0	68	56

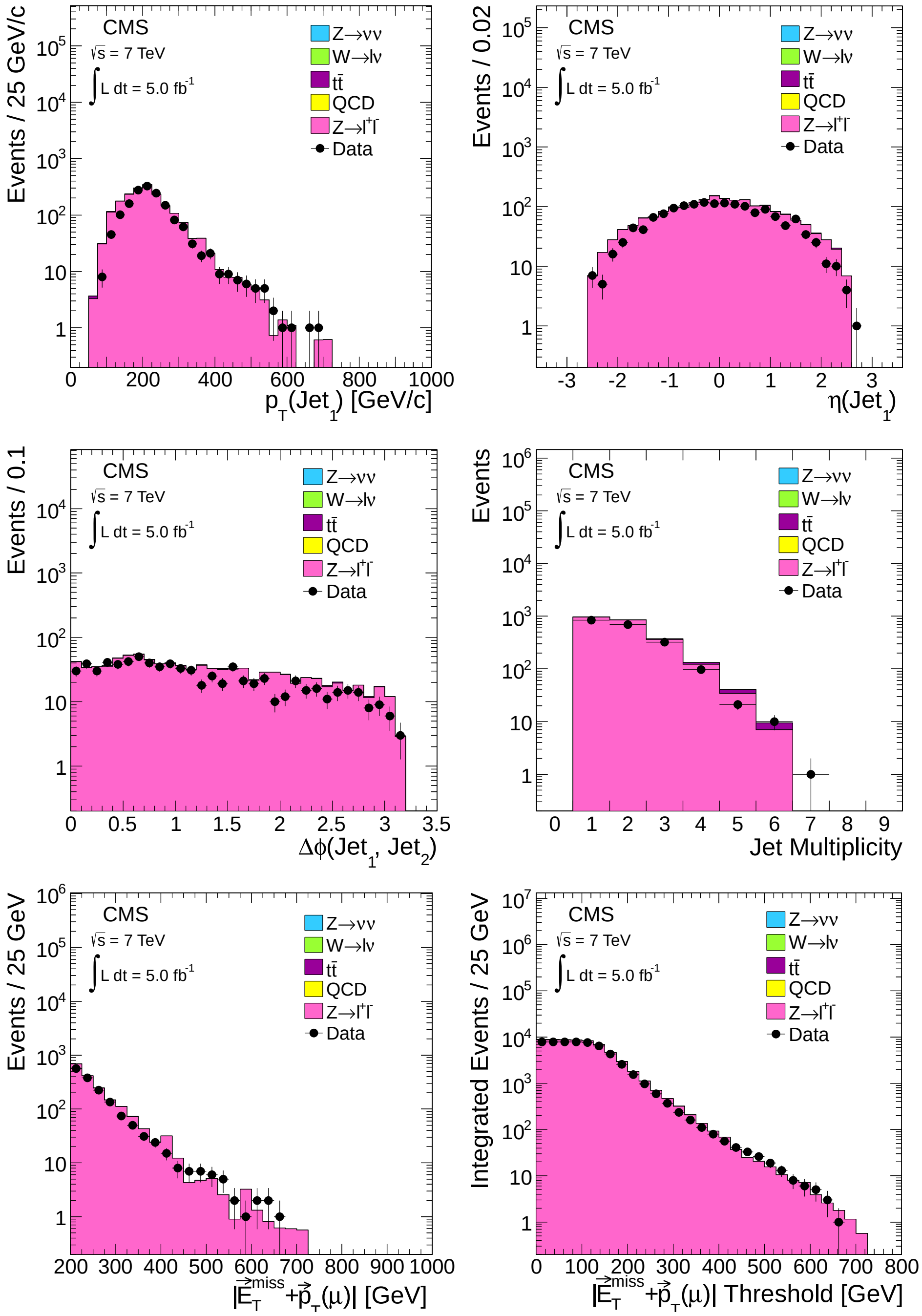

Figure 4.9 The shape and yield of the distributions observed in data are consistent with expectation from the SM $Z_{\mu^+\mu^-} + jets$ sample, proving the good understanding of the control sample.

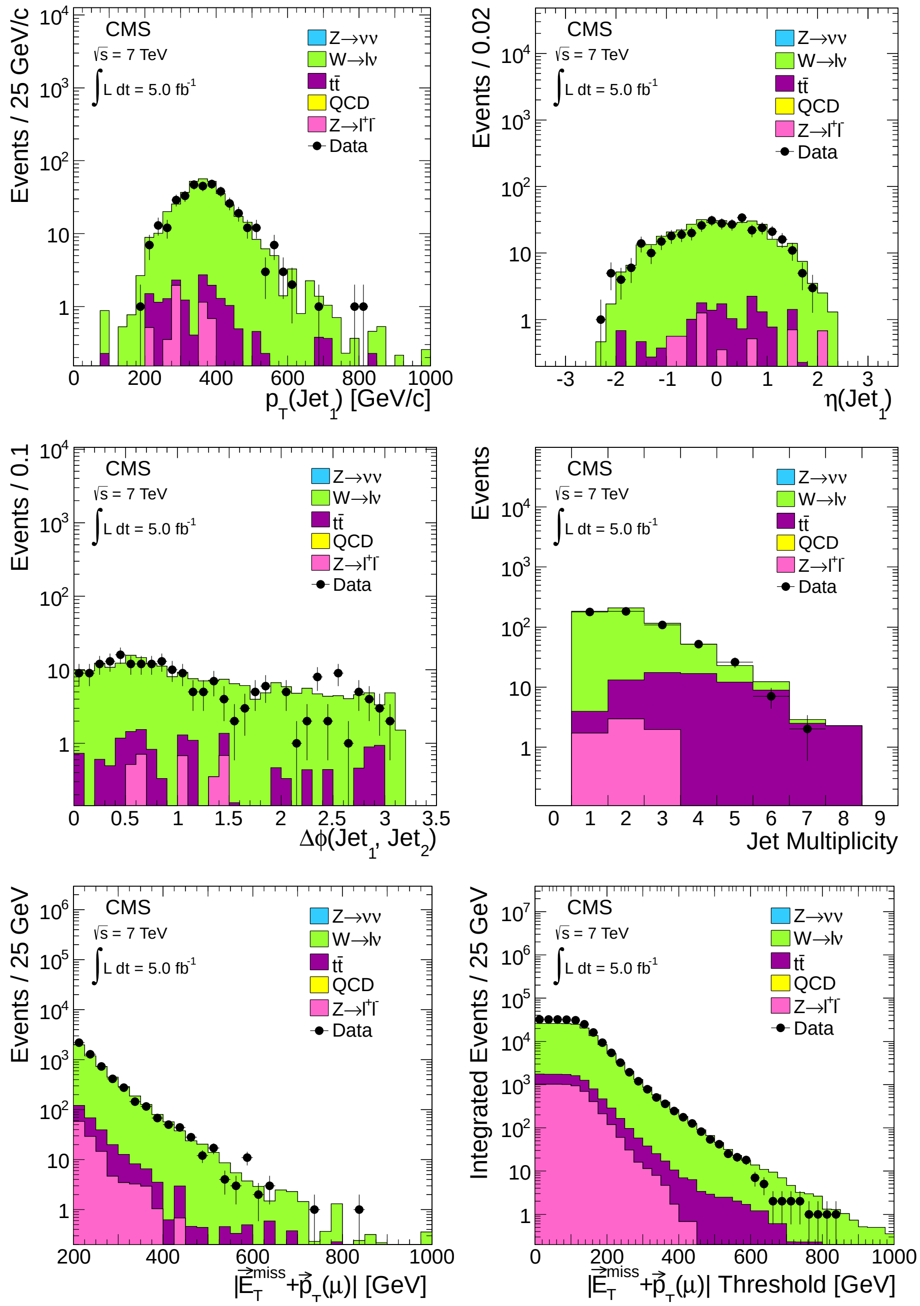

Figure 4.10 The shape and yield of the distributions observed in data are consistent with expectation from the SM $W_{\mu^+\nu} + jets$ sample, proving the good understanding of the control sample.

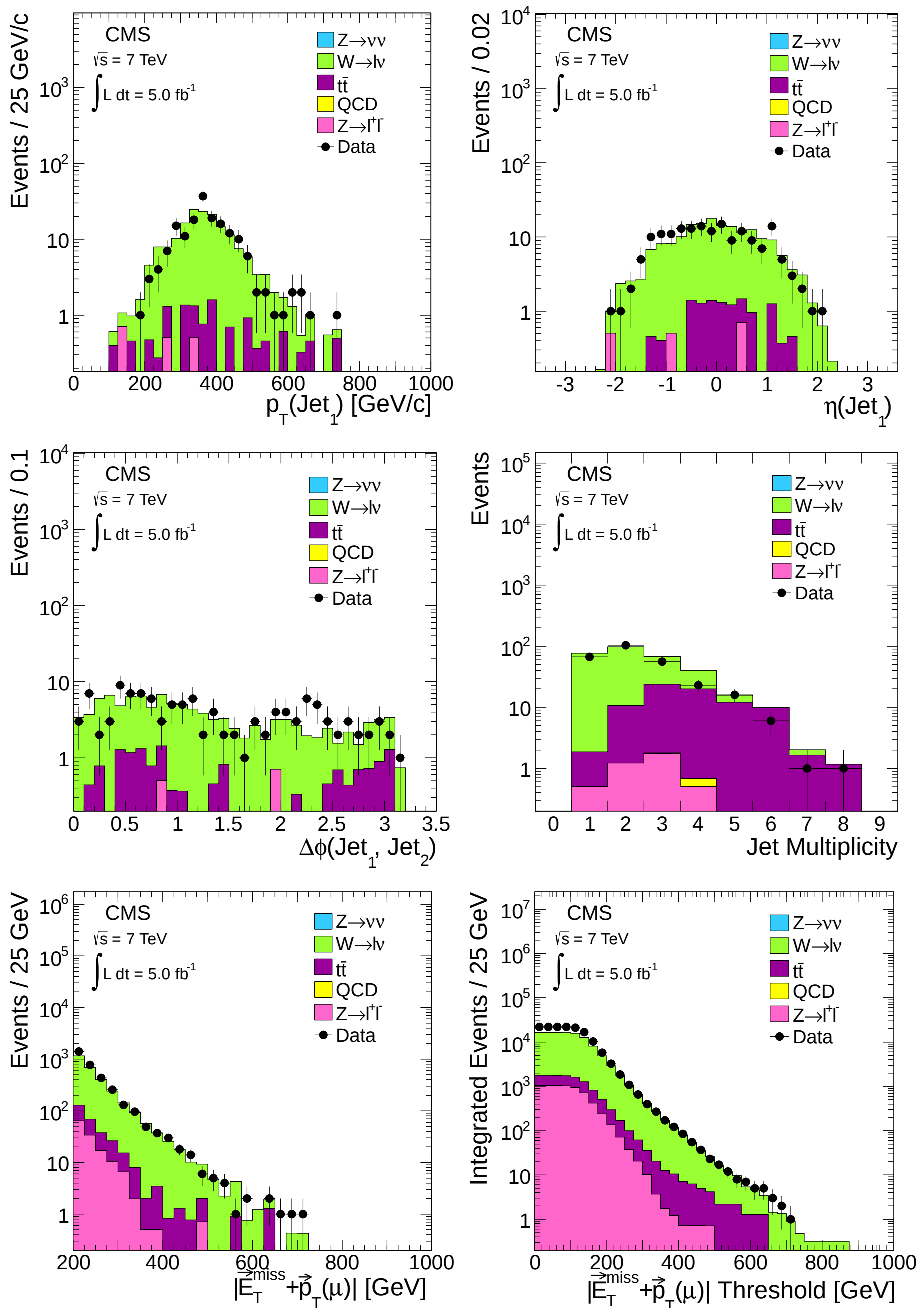

Figure 4.11 The shape and yield of the distributions observed in data are consistent with expectation from the SM $W_{\mu^- \nu} + jets$ sample, proving the good understanding of the control sample.

Table 4.5 Event yields for the $W_{\mu^{\pm}\nu} + jets$ data control samples and the backgrounds from MC.

	$W_{l^{\pm}\nu} + jets$	$Z_{l^{+}l^{-}} + jets$	$t\bar{t}$	Single t	All MC	Data
$E_{\mathrm{T}}^{\mathrm{miss}} > 200$	8165	253	332	60	8810	8666
$E_{\mathrm{T}}^{\mathrm{miss}} > 250$	3146	68	129	24	3367	3012
$E_{\mathrm{T}}^{\mathrm{miss}} > 300$	1304	22	52	11	1389	1179
$E_{\mathrm{T}}^{\mathrm{miss}} > 350$	580	6	23	4	613	531
$E_{\mathrm{T}}^{\mathrm{miss}} > 400$	271	1	13	2	287	261

4.4.1 Estimation of $Z_{\nu\bar{\nu}} + jets$ Background

The $Z_{\mu^{+}\mu^{-}} + jets$ and $Z_{\nu\bar{\nu}} + jets$ events share similar kinematic characteristics and by interpreting the pair of muons as missing energy, the topology of the process in which the Z boson decays to neutrinos can be reproduced. The missing transverse energy in the $Z_{\mu^{+}\mu^{-}} + jets$ event is redefined as the vector sum of the transverse momentum of the muons and the $E_{\mathrm{T}}^{\mathrm{miss}}$. The number of $Z_{\nu\bar{\nu}} + jets$ events can then be predicted using:

$$N(Z_{\nu\bar{\nu}}) = \frac{N^{obs} - N^{bgd}}{A * \varepsilon} \cdot R(\frac{Z_{\nu\bar{\nu}}}{Z_{l^{+}l^{-}}}) \tag{4.6}$$

where N^{obs} is the number of observed dimuon events, N^{bgd} is the number of estimated background events contributing to the dimuon sample, A is the fiducial and kinematic acceptance of the detector and the efficiency of the Z mass window cut, ε is the selection efficiency of the muon and R is the ratio of branching fractions for the Z decay to neutrinos and a pair of muons. These factors are determined as follows:

- N_{bgd} : The dimuon sample comprises predominantly of $Z_{\mu^{+}\mu^{-}} + jets$ events with less than 1% contamination from background. The backgrounds are estimated from MC and a 100% uncertainty is assigned to the number.

- A : The acceptance A is defined as the fraction of all generated events where the muons are reconstructed with $p_T > 20$ GeV and $|\eta| < 2.1$ and the invariant mass of the muons is within 60 GeV and 120 GeV. This is obtained from $Z_{\mu^{+}\mu^{-}} + jets$ MC using generator level information.

Table 4.6 Summary of the $Z_{\mu^+\mu^-} + jets$ event yields and the efficiency factors used to predict the $Z_{\nu\bar{\nu}} + jets$ background.

	$E_T^{miss} > 200$	$E_T^{miss} > 250$	$E_T^{miss} > 300$	$E_T^{miss} > 350$	$E_T^{miss} > 400$
N^{obs}	1537	593	235	111	56
N^{bgd}	17.5	6.3	2.2	0.2	0.2
Acceptance A	0.590	0.649	0.685	0.694	0.734
Efficiency ε	0.981	0.987	0.993	0.991	0.983
R	5.942	5.942	5.942	5.942	5.942
$N(Z_{\nu\bar{\nu}} + jets)$	15600	5442	2034	957	460
$N(Z_{\nu\bar{\nu}} + jets$ (after TIV))	14653	5102	1907	900	433

- ε : The muon selection efficiency ε is defined as the efficiency of selecting a muon passing all the identification and isolation criteria, given that it is within the detector acceptance. This efficiency has been studied using the Tag and Probe method by other groups for both data and MC and the data-MC scale factor is found to be very close to 1.0. We therefore estimate the selection efficiency using $Z_{l^+l^-} + jets$ MC and assign a systematic of 2% to cover the variation of the data-MC scale factor from 1.0, measured in (BERRYHILL, 2011).

- R : The ratio of the branching fraction R is obtained from (PDG, 2008) and is 5.942 ± 0.019 when $l = \mu$.

Table 4.6 shows the observed $Z_{\mu^+\mu^-} + jets$ event yields and the correction factors for the baseline selection with $E_T^{miss} > 200$ GeV and the search selections with higher E_T^{miss} cuts. Also shown is the predicted $Z_{\nu\bar{\nu}} + jets$ background before the TIV cut is applied. Since the control sample for this background estimation is obtained by relaxing the TIV, we estimate the TIV efficiency from MC for all the E_T^{miss} regions and apply this efficiency to obtain the final $Z_{\nu\bar{\nu}} + jets$ prediction.

A summary of the relative size of the contributing uncertainties to the $Z_{\nu\bar{\nu}} + jets$ estimation is shown in Table 4.7. The dominant systematic in all the E_T^{miss} regions is the size of the $Z_{\mu^+\mu^-} + jets$ control sample.

Figure 4.12 shows the invariant mass and transverse momentum distribution of the dimuon pair of the control sample compared to MC.

Table 4.7 Summary of the contributions to the total uncertainty on $Z_{\nu\bar{\nu}} + jets$ background from the various factors used in the data-driven estimation.

Source of Uncertainty	$E_T^{miss} > 200$	$E_T^{miss} > 250$	$E_T^{miss} > 300$	$E_T^{miss} > 350$	$E_T^{miss} > 400$
Statistics (N_{obs})	2.6%	4.1%	6.6%	9.5%	13.4%
Background (N_{bgd})	1.1%	1.0%	0.9%	0.2%	0.4%
Acceptance (A)	2.2%	2.5%	2.9%	3.7%	4.6%
Selection efficiency (ε)	2.1%	2.0%	2.0%	2.1%	2.3%
Ratio (R)	0.3%	0.3%	0.3%	0.3%	0.3%
Total	4.1%	5.3%	7.5%	10.4%	14.4%

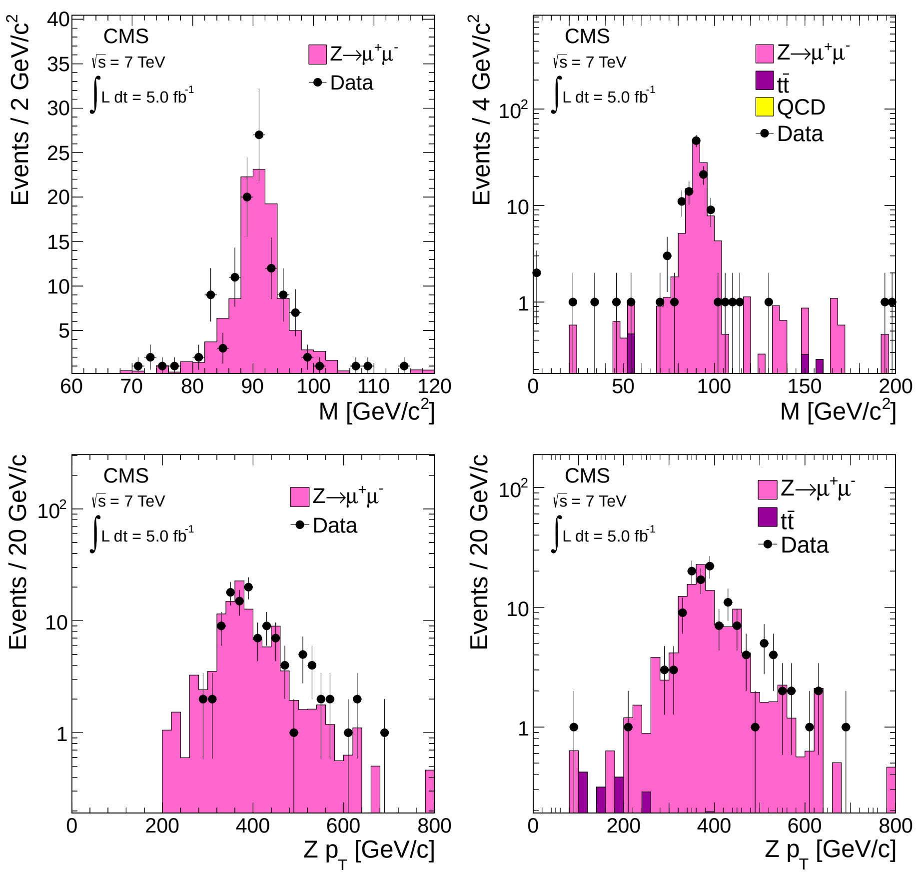

Figure 4.12 Invariant mass and transverse momentum of Z candidates in the dimuon sample, for $E_T^{miss} > 350$ GeV with mass windows 60,120 GeV/c and without mass window.

4.4.2 Estimation of $W_{l^{\pm}\nu} + jets$ Background

The second most dominant background arises from $W_{l^{\pm}\nu} + jets$ events that are not removed by the explicit lepton veto cut. These can come from taus which decay hadronically or events in which the lepton (electron or muon) is not identified, not isolated or not within the acceptance region. The latter of these events where the lepton is 'lost' are estimated by using the $W_{\mu^{\pm}\nu} + jets$ control sample. The data sample is first corrected for the acceptance (A') and efficiency of reconstructing the events (ε') in the detector to obtain the total number of generated events (N_{tot}). This is subsequently weighted by the inefficiency factors to obtain the predicted number of events that would not be rejected by the lepton veto and thus remain in the monojet sample.

The number of $W_{\mu^{\pm}\nu} + jets$ events that are out of the acceptance ($N_{!A}$) and not identified/isolated ($N_{!\varepsilon}$) can be written as:

$$N_{!A} = N_{tot} * (1 - A) \tag{4.7}$$

$$N_{!\varepsilon} = N_{tot} * A * (1 - \varepsilon) \tag{4.8}$$

where $N_{tot} = (N_{obs} - N_{bgd})/(A' * \varepsilon')$, A is the acceptance and ε is the selection efficiency of the muon selection used in the lepton veto definition. The total background from events where the muon is 'lost' is then given by,

$$N_{lost\mu} = N_{!A} + N_{!\varepsilon}. \tag{4.9}$$

Similarly, for an estimation of the 'lost' electron background, we start with the $W_{\mu^{\pm}\nu} + jets$ data sample, correct for the muon acceptance and selection efficiency to obtain the total number of generated $W_{\mu^{\pm}\nu} + jets$ events. The ratio of the generated $W_{\mu^{\pm}\nu} + jets$ and $W_{e^{\pm}\nu} + jets$ events is taken from MC and used to obtain N_{tot} for electrons. The same procedure as that outlined in the above equations is then followed to obtain the number of events where the electron is not reconstructed/isolated or out of the acceptance. The electron acceptance is obtained using generator level MC and the selection efficiency is also obtained from MC with

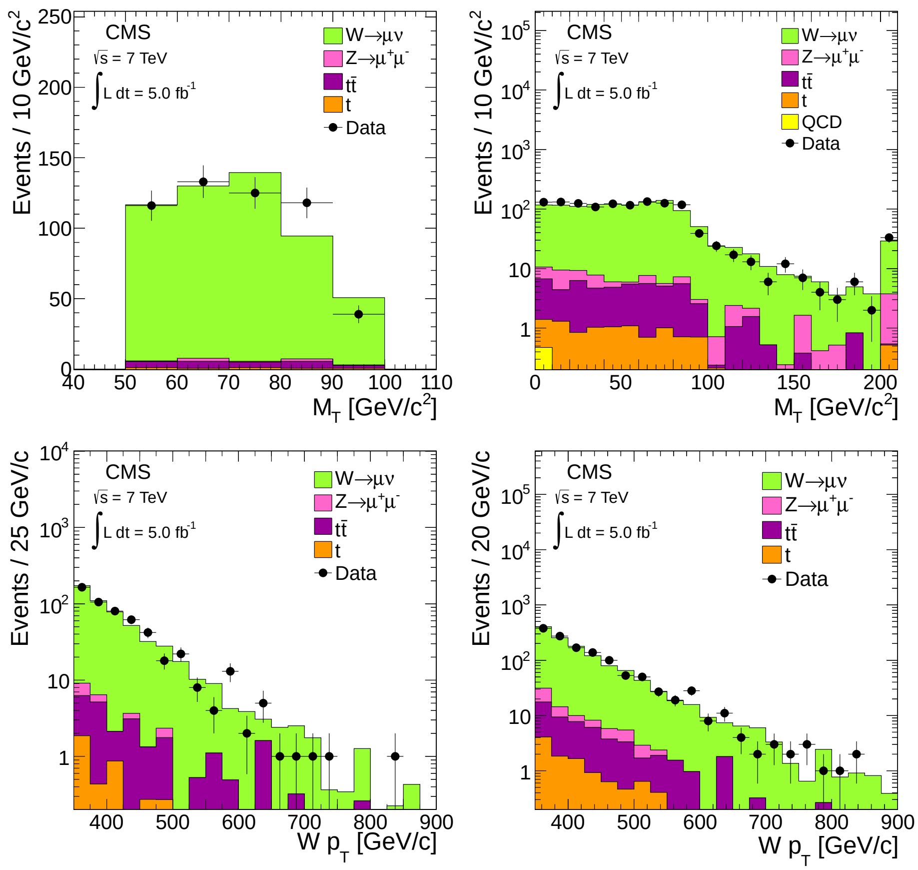

Figure 4.13 Transverse mass and momentum of $W_{\mu^{\pm}\nu} + jets$ candidates in the single-muon sample, for $E_{\mathrm{T}}^{\mathrm{miss}} > 350$ GeV.

an assigned systematic that covers the variation in efficiency between data and MC (BERRYHILL, 2011).

A comparison between data and MC for some of the kinematic distributions for the $W_{\mu^{\pm}\nu} + jets$ control sample are shown in Figure 4.13, where the missing transverse energy is redefined as the vector sum of the muon transverse momentum and missing transverse energy to emulate the missing energy in events where the lepton is lost. A summary of the estimated remaining $W_{l^{\pm}\nu} + jets$ events in the monojet sample, with a breakdown into those events where the leptons are not reconstructed and those in which the lepton is outside the acceptance is shown in Table 4.8. A more detailed version of this table showing the values of all the relevant factors that are used to estimate the $W_{l^{\pm}\nu} + jets$ background can be found in

Table 4.8 Estimation of the remaining $W_{l^{\pm}\nu} + jets$ background from the lost electron and muon contributions.

	$E_T^{miss} > 200$	$E_T^{miss} > 250$	$E_T^{miss} > 300$	$E_T^{miss} > 350$	$E_T^{miss} > 400$
$N^{\mu}_{!A}$	3168.4	835.4	238.2	84.0	35.4
$N^{\mu}_{!\varepsilon}$	587.4	153.7	45.2	17.4	7.2
$N_{lost\mu}$	3755.7	989.0	283.5	101.4	42.6
$N^{e}_{!A}$	2571.5	748.9	238.1	88.6	39.3
$N^{e}_{!\varepsilon}$	1272.3	322.7	105.9	45.3	18.3
N_{loste}	3843.8	1071.6	344.0	133.9	57.6
$N_{\text{hadronic}\,\tau}$	3807.6	1080.1	353.7	145.3	65.2
$N_{W_{l^{\pm}\nu}+jets}$	11407	3141	981	381	165
$N_{W_{l^{\pm}\nu}+jets}$ (after TIV)	9513	2619	812	310	134
Prediction from $W_{l^{\pm}\nu} + jets$ MC	9047.7	2759.5	904.7	338.5	138.5

Table 4.9 Summary of the contributions to the total uncertainty on $W_{l^{\pm}\nu} + jets$ background from the various factors used in the data-driven estimation.

Source of Uncertainty	$E_T^{miss} > 200$	$E_T^{miss} > 250$	$E_T^{miss} > 300$	$E_T^{miss} > 350$	$E_T^{miss} > 400$
Statistics (N_{obs})	0.8%	1.3%	2.0%	2.9%	4.0%
Background (N_{bgd})	5.0%	4.8%	4.6%	3.9%	3.7%
Acceptance (A)	4.8%	5.7%	6.7%	7.7%	8.7%
Selection efficiency (ε)	4.1%	4.9%	5.9%	6.8%	7.7%
Total	8.1%	9.0%	10.2%	11.3%	12.8%

(APPENDIX D). The remaining component of the $W_{l^{\pm}\nu} + jets$ background which is not accounted for by this method is that from hadronically decaying tau. This is taken from $W_{l^{\pm}\nu} + jets$ MC and corrected for the data/MC scale factor obtained from $W_{\mu^{\pm}\nu} + jets$ events.

Since the control sample for this background estimation is obtained by relaxing the TIV, we estimate the TIV efficiency from MC for all the E_T^{miss} regions and apply this efficiency to obtain the final $W_{l^{\pm}\nu} + jets$ prediction. The uncertainty on the $W_{l^{\pm}\nu} + jets$ estimation includes; the statistical uncertainty on the number of single-muon events in the data, a conservative 100% uncertainty on the background events obtained from MC, an acceptance uncertainty from parton density function (PDF) (2%) and MC statistics and an uncertainty on the selection efficiency ε from the variation in the data/MC scale factor and MC statistics.

A summary of the fractional contributions of these uncertainties to the total error on the $W_{l^{\pm}\nu} + jets$ background is shown in Table 4.9.

The remaining backgrounds to the monojet sample from $t\bar{t}$, QCD, single t and $Z_{l^+l^-} + jets$ events are found to be at the 1% level. These are taken from MC and assigned a 100% systematic uncertainty.

4.5 Systematic Uncertainties on Signal

The systematic uncertainties on the background event yields have been described in detail in the previous section. The sources of uncertainties contributing to the signal are:

1. The jet energy scale (JES) uncertainty, estimated by shifting the four-vectors of the jets by an η- and p_{T}-dependent factor (CMS JME-10-010, 2010), yielding a variation of 8–11% (8–13%) for the dark matter (ADD) signal. Detail of systematic errors from jet energy scale can be seen in Table 4.10 and Table 4.11 for dark matter and ADD models respectively.

2. The noise cleaning uncertainty, obtained by assigning the full effect of noise cleaning as systematic uncertainty, 2% (3%) for dark matter (ADD) signal.

3. PDF uncertainties evaluated using the PDF4LHC (BOTJE, 2011) prescription and resulting in a systematic uncertainty of 1–7% (1–4%) for the dark matter (ADD) signal. Detail of systematic errors from PDF can be seen in Table 4.10 and Table 4.11 for dark matter and ADD models.

4. The renormalization/factorization scale uncertainty, evaluated by varying the scale up and down by a factor of two, 5% for both dark matter and ADD signals.

5. ISR uncertainty, estimated by changing PYTHIA parameters, yielding a variation of 15% for both dark matter and ADD signals.

6. Uncertainty on the pileup simulation, 3% for both dark matter and ADD signals.

7. The limited statistics of the simulated sample yielding a variation of 2–5% (2–4%) on the dark matter (ADD) signal.

The total uncertainty on the signal for the DM (ADD) models for these sources of uncertainty is 20% (21%). In addition, a 2.2% uncertainty on the integrated luminosity measurement (CMS SMP-12-008, 2012) is included.

4.6 Results Interpretation and Exclusion Limits

The total number of events observed is compared with the total number of estimated background events in Table 4.12, together with the breakdown of this background into separate subprocesses. Contribution from $Z_{\nu\bar{\nu}} + jets$ and $W_{\mu^{\pm}\nu} + jets$ processes are determined from the data. Contributions from $t\bar{t}$, $Z_{l^{+}l^{-}} + jets$, single t, and QCD multijet processes are determined from simulation and are assumed to have 100% uncertainty. The number of events observed is consistent with the number of events expected from SM backgrounds. To interpret the consistency of the observed number of events with the background expectation in the context of a model, and also to facilitate comparison with previous results, we set exclusion limits for the ADD model and the dark matter models. The CLs method (MOHETA, 2010) is used for calculating the upper limits on the number of signal events, and systematic uncertainties are modeled by log-normal distributions.

In Figure 4.14 and Table 4.13 we show the expected limit on the cross-section as a function of M_D for the data and SM expectations along with the observed 95% CL in 1 and 2 σ, for different δ values. The signal processes, generated at Leading Order (LO) and corrected to Next-to-leading order (NLO) cross sections, are used to calculate the expected and observed exclusion curves. Systematic uncertainties on the NLO predictions due to the choice of the renormalisation and factorization scale have been taken into account. K-factors chosen are shown in Table 4.14 .

The 95% CL exclusion region comprises those values of M_D for which the cross-section is less than the 95% limit. Results for ADD are shown in Table 4.14 as a function of δ, with and without K-factors applied. We compare our current results

Table 4.10 Dark Matter Axial-Vector and Vector models Acceptance and Systematic Uncertainity on JES and PDF for $E_{\mathrm{T}}^{\mathrm{miss}} > 350$.

Signal	χ mass [GeV]	Acceptance %	JES %	PDF %
DM AV-d	0.01	2.518	-11.831 /10.143	-0.032 / 0.041
DM AV-d	0.1	2.551	-9.815 / 9.892	-0.053 / 0.051
DM AV-d	1	2.588	-10.887 / 9.662	-0.097 / 0.111
DM AV-d	10	2.583	-9.700 / 9.817	-0.121 / 0.133
DM AV-d	100	3.103	-10.024 / 9.751	-0.322 / 0.359
DM AV-d	200	3.731	-8.440 / 9.176	-0.734 / 0.804
DM AV-d	300	4.077	-9.260 / 9.087	-1.140 / 1.264
DM AV-d	400	4.251	-8.016 / 8.111	-1.448 / 1.627
DM AV-d	700	4.892	-7.210 / 7.603	-2.413 / 2.742
DM AV-d	1000	4.827	-9.031 / 7.679	-4.217 / 4.551
DM AV-u	0.01	3.049	-9.950 / 8.023	-0.061 / 0.043
DM AV-u	0.1	3.055	-10.197 / 9.648	-0.043 / 0.054
DM AV-u	1	3.076	-10.010 / 8.648	-0.096 / 0.111
DM AV-u	10	3.135	-9.521 / 9.358	-0.106 / 0.121
DM AV-u	100	3.664	-10.134 / 8.792	-0.255 / 0.300
DM AV-u	200	4.535	-7.631 / 7.634	-0.477 / 0.546
DM AV-u	300	5.019	-8.002 / 8.773	-0.728 / 0.794
DM AV-u	400	5.137	-8.609 / 8.247	-1.068 / 1.096
DM AV-u	700	5.637	-8.615 / 6.833	-1.886 / 2.011
DM AV-u	1000	5.807	-7.786 / 7.166	-3.039 / 3.276
DM V-d	0.01	3.131	-10.568 / 8.582	-0.088 / 0.083
DM V-d	0.1	2.988	-9.363 / 8.467	-0.091 / 0.092
DM V-d	1	3.047	-9.223 / 8.018	-0.115 / 0.121
DM V-d	10	3.066	-9.845 / 10.568	-0.114 / 0.126
DM V-d	100	3.504	-8.142 / 8.267	-0.262 / 0.288
DM V-d	200	4.021	-9.426 / 8.449	-0.529 / 0.581
DM V-d	300	4.500	-9.549 / 8.124	-0.856 / 0.952
DM V-d	400	4.954	-8.104 / 8.393	-1.141 / 1.271
DM V-d	700	5.755	-8.857 / 7.153	-2.193 / 2.465
DM V-d	1000	5.935	-7.883 / 8.314	-3.713 / 4.102
DM V-u	0.01	2.483	-11.027 / 8.991	-0.102 / 0.111
DM V-u	0.1	2.503	-11.203 / 8.806	-0.103 / 0.108
DM V-u	1	2.517	-9.186 / 9.379	-0.101 / 0.116
DM V-u	10	2.541	-10.404 / 9.982	-0.100 / 0.114
DM V-u	100	2.860	-9.945 / 10.581	-0.204 / 0.238
DM V-u	200	3.392	-9.072 / 9.714	-0.444 / 0.518
DM V-u	300	3.856	-8.312 / 7.906	-0.655 / 0.723
DM V-u	400	4.073	-9.758 / 9.038	-0.971 / 1.014
DM V-u	700	4.711	-7.991 / 8.726	-1.848 / 1.910
DM V-u	1000	4.925	-8.590 / 8.337	-2.875 / 3.127

with previous results from CMS, ATLAS, CDF and LEP in Figure 4.15. We can also interpret our results in the context of the dark matter models described in Section 3. In Figure 4.16 and Table 4.15 we show the expected cross-section limit as a function of M_{χ} for the data and SM expectations along with the observed

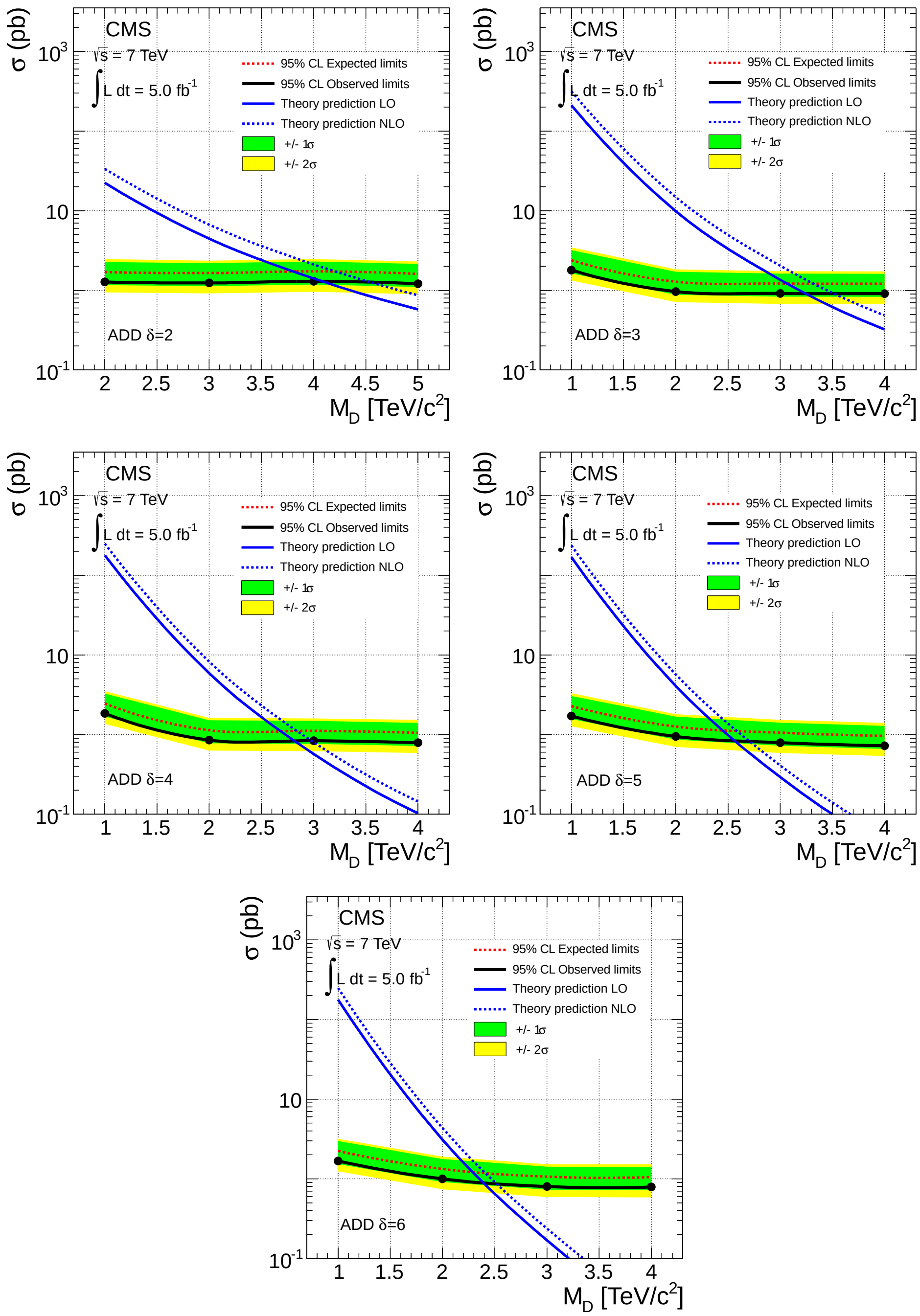

Figure 4.14 95% CL upper limits on the ADD production rate in pb. The median 1 and 2 σ values are obtained from the distribution of upper limits obtained in 1000 pseudo-experiments performed at each model point.

Table 4.11 ADD Models Acceptance and Systematic Uncertainity on JES and PDF for $E_{\mathrm{T}}^{\mathrm{miss}} > 350$.

Signal	Acceptance (%)	JES (%)	PDF(%)
$M_{\mathrm{D}} = 2, \delta = 2$	2.378	-10.846 /9.047	-6.073 / 7.585
$M_{\mathrm{D}} = 3, \delta = 2$	2.447	-12.737/ 7.353	-6.002 / 7.395
$M_{\mathrm{D}} = 4, \delta = 2$	2.330	-11.445/ 9.654	-6.981 / 8.821
$M_{\mathrm{D}} = 1, \delta = 3$	1.687	-13.58 / 9.238	-6.351 / 8.074
$M_{\mathrm{D}} = 2, \delta = 3$	3.139	-9.781 / 10.600	-4.395 / 5.585
$M_{\mathrm{D}} = 3, \delta = 3$	3.310	-9.271 / 10.877	-4.350 / 5.429
$M_{\mathrm{D}} = 4, \delta = 3$	3.324	-10.642/ 9.834	-5.170 / 6.582
$M_{\mathrm{D}} = 1, \delta = 4$	1.645	-13.686/ 15.536	-2.547 / 3.366
$M_{\mathrm{D}} = 2, \delta = 4$	3.555	-10.085/ 8.603	-2.601 / 3.087
$M_{\mathrm{D}} = 3, \delta = 4$	3.617	-10.315/ 9.180	-3.869 / 4.747
$M_{\mathrm{D}} = 4, \delta = 4$	3.825	-9.418 / 10.005	-3.346 / 4.025
$M_{\mathrm{D}} = 1, \delta = 5$	1.767	-13.418/ 9.285	-1.948 / 2.451
$M_{\mathrm{D}} = 2, \delta = 5$	3.202	-10.673/ 9.660	-2.440 / 2.263
$M_{\mathrm{D}} = 3, \delta = 5$	3.819	-8.647 / 8.676	-2.551 / 2.596
$M_{\mathrm{D}} = 4, \delta = 5$	4.175	-8.620 / 8.582	-2.988 / 2.847
$M_{\mathrm{D}} = 1, \delta = 6$	1.808	-6.560 / 10.805	-2.461 / 2.962
$M_{\mathrm{D}} = 2, \delta = 6$	3.039	-11.307/ 11.919	-2.669 / 2.555
$M_{\mathrm{D}} = 3, \delta = 6$	3.793	-8.660 / 9.676	-2.936 / 2.742

90% CL values in 1 and 2 σ, for the Vector (V) and Axial-Vector (AV) couplings to up and down quarks.

Since the upper limit on the cross-section depends on our specific event production criteria such as $\hat{p}_T$, we convert these limits into limits on the dark matter spin independent (SI) and spin dependent (SD) nucleon scattering cross section using the formulae outlined below. This can then be compared to the constraints from direct detection experiments.

$$\Lambda^4 = \Lambda_d^4 + \Lambda_u^4 \tag{4.10}$$

$$\sigma_{SI} = 9\frac{\mu^2}{\pi\Lambda^4} \tag{4.11}$$

$$\sigma_{SD} = 0.33\frac{\mu^2}{\pi\Lambda^4} \tag{4.12}$$

$$\mu = \frac{m_\chi m_p}{m_\chi + m_p} \tag{4.13}$$

where σ_{SI} is SI cross section, σ_{SD} is SD cross section and μ is reduced mass of dark matter and nucleon (proton) system. In the following reference (HARNIK, 2010),

Table 4.12 SM background predictions compared with data passing the selection requirements for various E_T^{miss} thresholds, corresponding to integrated luminosity of 5.0 fb^{-1}. The uncertainties include both statistical and systematic terms. In the last two rows, expected and observed 95% confidence level upper limits on possible contributions from new physics passing the selection requirements are given.

E_T^{miss}(GeV/c) $\rightarrow$	≥ 250	≥ 300	≥ 350	≥ 400
Process	Events			
$Z_{\nu\bar{\nu}} + jets$	5106 $\pm$ 271	1908 $\pm$ 143	900 $\pm$ 94	433 $\pm$ 62
$W_{l^{\pm}\nu} + jets$	2632 $\pm$ 237	816 $\pm$ 83	312 $\pm$ 35	135 $\pm$ 17
$t\bar{t}$	69.8 $\pm$ 69.8	22.6 $\pm$ 22.6	8.5 $\pm$ 8.5	3.0 $\pm$ 3.0
$Z_{l^+l^-} + jets$	22.3 $\pm$22.3	6.1 $\pm$ 6.1	2.0 $\pm$ 2.0	0.6 $\pm$ 0.6
Single t	10.2 $\pm$10.2	2.7 $\pm$ 2.7	1.1 $\pm$ 1.1	0.4 $\pm$ 0.4
QCD Multijets	2.2 $\pm$2.2	1.3 $\pm$1.3	1.3 $\pm$1.3	1.3 $\pm$1.3
Total SM	7842 $\pm$ 367	2757 $\pm$ 167	1225 $\pm$ 101	573$\pm$ 65
Data	7584	2774	1142	522
Expected upper limit non-SM	779	325	200	118
Observed upper limit non-SM	600	368	158	95

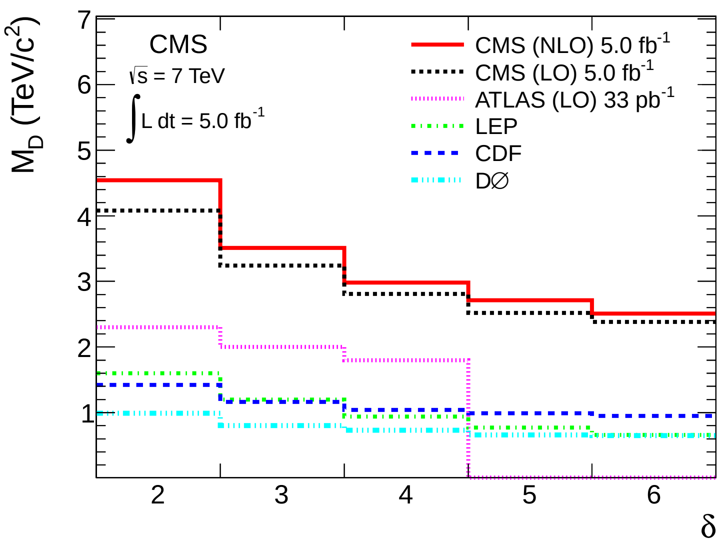

Figure 4.15 Comparison of lower limits on M_D versus the number of extra dimensions with ATLAS, LEP, CDF , and D0 .

Table 4.13 95% CL upper limits on the ADD production rate in pb. The median 1 and 2 σ values are obtained from the distribution of upper limits obtained in 1000 pseudo-experiments performed at each model point.

Signal	Obs. Limit	Exp. Limit	-1σ	+1σ	-2σ	+2σ
$M_D = 2, \delta = 2$	1.229	1.637	1.121	2.182	0.909	2.379
$M_D = 3, \delta = 2$	1.195	1.591	1.089	2.121	0.883	2.275
$M_D = 4, \delta = 2$	1.255	1.671	1.144	2.227	0.928	2.386
$M_D = 5, \delta = 2$	1.168	1.555	1.065	2.073	0.864	2.221
$M_D = 1, \delta = 3$	1.733	2.308	1.580	3.076	1.281	3.353
$M_D = 2, \delta = 3$	0.931	1.239	0.849	1.653	0.688	1.771
$M_D = 3, \delta = 3$	0.883	1.176	0.805	1.568	0.653	1.679
$M_D = 4, \delta = 3$	0.879	1.171	0.801	1.561	0.650	1.672
$M_D = 1, \delta = 4$	1.777	2.367	1.620	3.155	1.314	3.379
$M_D = 2, \delta = 4$	0.822	1.095	0.749	1.459	0.608	1.566
$M_D = 3, \delta = 4$	0.808	1.076	0.737	1.434	0.597	1.537
$M_D = 4, \delta = 4$	0.764	1.018	0.696	1.356	0.565	1.479
$M_D = 1, \delta = 5$	1.654	2.203	1.508	2.937	1.223	3.201
$M_D = 2, \delta = 5$	0.913	1.216	0.832	1.620	0.675	1.736
$M_D = 3, \delta = 5$	0.765	1.019	0.697	1.359	0.566	1.481
$M_D = 4, \delta = 5$	0.700	0.932	0.638	1.243	0.517	1.355
$M_D = 1, \delta = 6$	1.617	2.153	1.474	2.870	1.196	3.075
$M_D = 2, \delta = 6$	0.962	1.281	0.877	1.707	0.711	1.829
$M_D = 3, \delta = 6$	0.770	1.026	0.702	1.368	0.570	1.468
$M_D = 4, \delta = 6$	0.761	1.013	0.694	1.351	0.563	1.473

SI cross section corresponds to Vector model, and SD cross section corresponds to Axial-Vector model. In Figure 4.17 we compare SI and SD model limits in cm^2 with results from various direct and indirect detection experiments.

Table 4.14 Observed and expected 95% CL lower limits on the ADD model parameter M_D (in TeV/c^2) as a function of δ, with and without NLO K-factors applied.

δ	LO		NLO	
	Exp. Limit (TeV/c^2)	Obs. Limit (TeV/c^2)	Exp. Limit (TeV/c^2)	Obs. Limit (TeV/c^2)
2	3.81	4.08	4.20	4.54
3	3.06	3.24	3.32	3.51
4	2.69	2.81	2.84	2.98
5	2.44	2.52	2.59	2.71
6	2.28	2.38	2.40	2.51

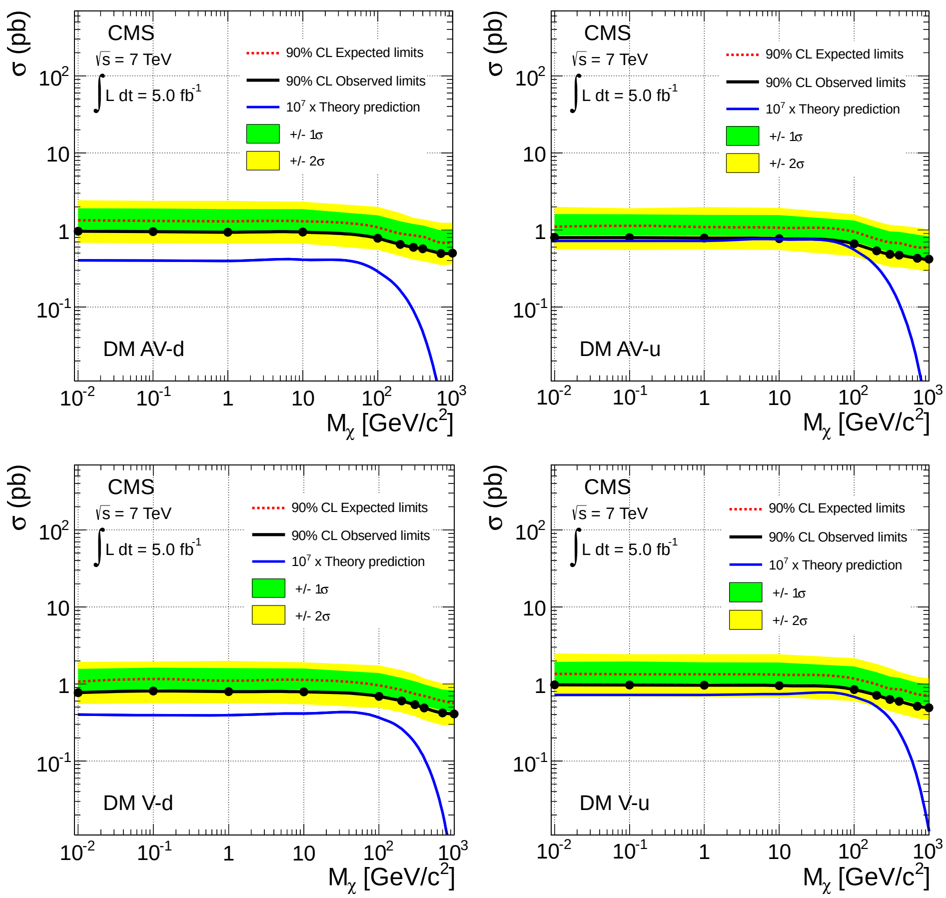

Figure 4.16 90% CL upper limits on the dark matter production rate in pb for 40 TeV Mediator mass. The median 1 and 2 σ values are obtained from the distribution of upper limits obtained in 1000 pseudo-experiments performed at each model point.

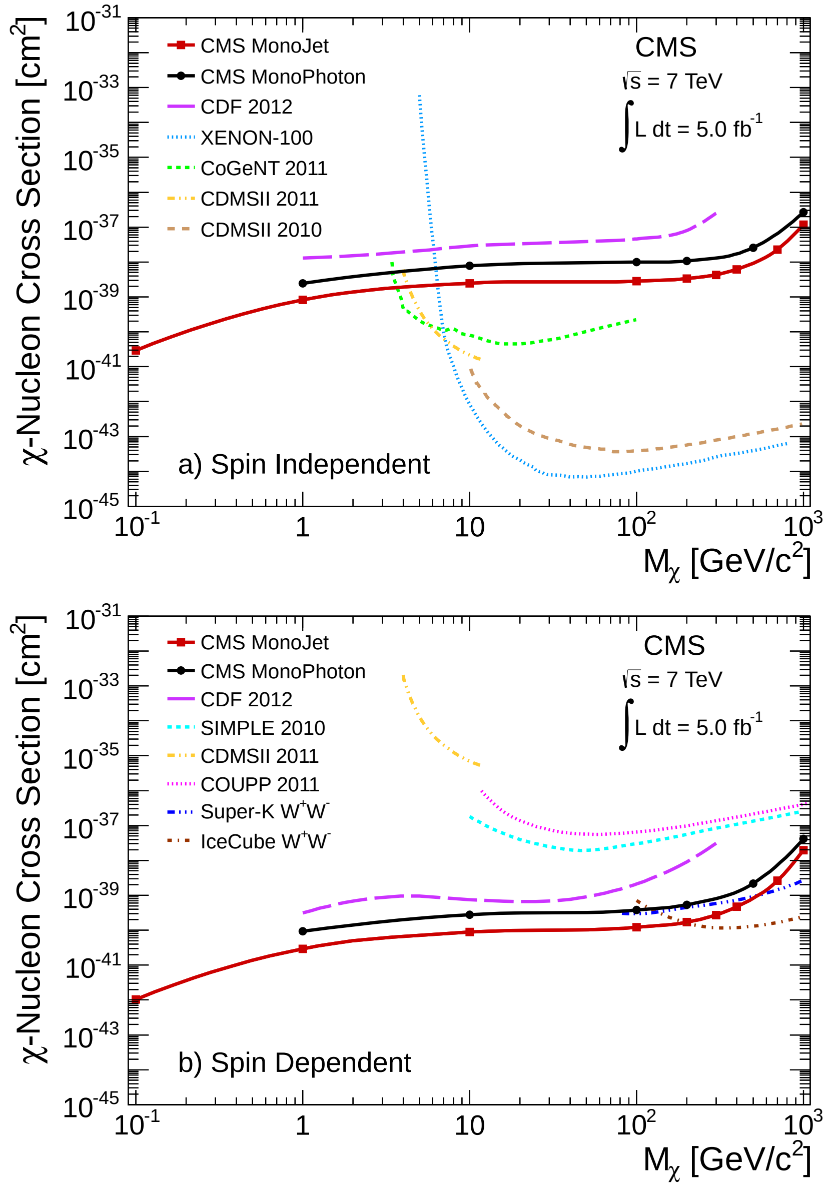

Figure 4.17 Comparison of the 90% CL upper limits on the dark matter-nucleon scattering cross section versus mass of dark matter particle for the spin-independent (top) and spin-dependent (bottom) models with results from CMS using monophoton signature, CDF, XENON100, CoGeNT, COUPP, CDMS II, SIMPLE, IceCube, and Super-K collaborations.

Table 4.15 90% CL upper limits on the dark matter production rate in pb for 40 TeV Mediator mass. The median 1 and 2 σ values are obtained from the distribution of upper limits obtained in 1000 pseudo-experiments performed at each model point.

Signal	χ mass [GeV]	Obs. Limit	Exp. Limit	-1σ	+1σ	-2σ	+2σ
DM AV-d	0.01	0.961	1.332	1.028	1.911	0.681	2.427
DM AV-d	0.1	0.949	1.314	0.962	1.900	0.673	2.389
DM AV-d	1	0.935	1.295	0.948	1.862	0.663	2.385
DM AV-d	10	0.937	1.298	0.950	1.865	0.664	2.323
DM AV-d	100	0.780	1.080	0.790	1.552	0.553	1.993
DM AV-d	200	0.649	0.898	0.657	1.291	0.460	1.657
DM AV-d	300	0.594	0.849	0.635	1.197	0.411	1.435
DM AV-d	400	0.570	0.815	0.609	1.147	0.394	1.376
DM AV-d	700	0.495	0.685	0.501	0.985	0.350	1.240
DM AV-d	1000	0.501	0.694	0.508	0.998	0.355	1.243
DM AV-u	0.01	0.794	1.100	0.849	1.604	0.563	1.989
DM AV-u	0.1	0.793	1.134	0.848	1.596	0.548	1.915
DM AV-u	1	0.787	1.090	0.842	1.568	0.558	1.987
DM AV-u	10	0.772	1.069	0.825	1.560	0.547	1.935
DM AV-u	100	0.661	0.945	0.707	1.326	0.457	1.597
DM AV-u	200	0.534	0.764	0.571	1.071	0.369	1.290
DM AV-u	300	0.483	0.690	0.516	0.957	0.334	1.165
DM AV-u	400	0.472	0.674	0.504	0.948	0.326	1.139
DM AV-u	700	0.429	0.595	0.429	0.867	0.304	1.076
DM AV-u	1000	0.417	0.596	0.446	0.827	0.288	1.007
DM V-d	0.01	0.773	1.071	0.774	1.565	0.548	1.937
DM V-d	0.1	0.811	1.159	0.867	1.626	0.561	1.958
DM V-d	1	0.794	1.100	0.795	1.605	0.563	1.991
DM V-d	10	0.790	1.130	0.845	1.585	0.546	1.908
DM V-d	100	0.691	0.957	0.700	1.390	0.489	1.739
DM V-d	200	0.602	0.834	0.602	1.198	0.426	1.508
DM V-d	300	0.538	0.745	0.545	1.086	0.381	1.348
DM V-d	400	0.489	0.699	0.523	0.986	0.338	1.181
DM V-d	700	0.421	0.602	0.450	0.844	0.291	1.016
DM V-d	1000	0.408	0.565	0.436	0.824	0.289	1.022
DM V-u	0.01	0.975	1.350	0.988	1.940	0.691	2.491
DM V-u	0.1	0.967	1.340	0.968	1.953	0.685	2.423
DM V-u	1	0.962	1.332	1.029	1.912	0.682	2.428
DM V-u	10	0.953	1.319	0.965	1.896	0.675	2.434
DM V-u	100	0.846	1.172	0.858	1.685	0.600	2.162
DM V-u	200	0.713	0.988	0.723	1.420	0.506	1.823
DM V-u	300	0.628	0.869	0.636	1.250	0.445	1.604
DM V-u	400	0.595	0.850	0.636	1.199	0.411	1.436
DM V-u	700	0.514	0.735	0.550	1.035	0.355	1.242
DM V-u	1000	0.492	0.703	0.526	0.991	0.340	1.188

4.7 Conclusions

A search has been performed for signatures of new physics yielding an excess of events in the monojet and $E_{\mathrm{T}}^{\mathrm{miss}}$channel. The results have been used to constrain

Table 4.16 Observed 90% CL limits on the dark matter-nucleon cross section and effective contact interaction scale Λ for the spin-dependent and spin-independent interactions.

	Spin Dependent		Spin Independent	
M_χ (GeV/c^2)	Λ (GeV)	$\sigma_{\chi N}$ (cm^2)	Λ (GeV)	$\sigma_{\chi N}$ (cm^2)
0.01	753	1.25×10^{-44}	753	3.39×10^{-43}
0.1	754	1.03×10^{-42}	749	2.90×10^{-41}
1	755	2.94×10^{-41}	751	8.21×10^{-40}
10	765	8.79×10^{-41}	760	2.47×10^{-39}
100	736	1.21×10^{-40}	764	2.83×10^{-39}
200	677	1.70×10^{-40}	736	3.31×10^{-39}
300	602	2.73×10^{-40}	690	4.30×10^{-39}
400	524	4.74×10^{-40}	631	6.15×10^{-39}
700	341	2.65×10^{-39}	455	2.28×10^{-38}
1000	206	1.98×10^{-38}	302	1.18×10^{-37}

the pair production of dark matter particles in models with a heavy mediator, and large extra dimensions in the context of the Arkani-Hamed, Dimopoulos, and Dvali model. The data sample corresponds to an integrated luminosity of $5.0\,\mathrm{fb}^{-1}$and includes events containing a jet with transverse momentum above 110 GeV/c and $E_{\mathrm{T}}^{\mathrm{miss}}$ above 350 GeV/c. Many standard model processes also have the same signature. The QCD multijet contribution is reduced by several orders of magnitude to a negligible level using topological selections. The dominant backgrounds, $Z_{\nu\bar{\nu}} + jets$ and $W_{l^{\pm}\nu} + jets$, are estimated from data samples enriched in $Z_{\mu^+\mu^-} + jets$ and $W_{\mu^{\pm}\nu} + jets$ events. The data are found to be in good agreement with the expected contributions from standard model processes.

A dark matter-nucleon scattering cross section in the framework of an effective theory is excluded above 1.03×10^{-42} (1.21×10^{-40}) cm^2 and 2.90×10^{-41} (2.83×10^{-39}) cm^2 for a dark matter particle with mass 0.1 (100) GeV/c^2 at the 90% CL for the spin dependent and spin independent models, respectively. For the spin independent model, these are the best limits for dark matter particles with mass below 3.5 GeV/c^2, a region as yet unexplored by the direct detection experiments. For the spin dependent model, these limits represent the most stringent constraints over the 0.1–200 GeV/c^2 mass range.

Values for the large extra dimensions ADD model parameter M_{D} smaller than

4.54, 3.51, 2.98, 2.71, and 2.51 TeV/c^2 are excluded for a number of extra dimensions δ =2, 3, 4, 5, and 6, respectively, representing a significant improvement (1 TeV/c^2) over the previous limits.

REFERENCES

AAD G. et al., 2011 Search for new phenomena with the monojet and missing transverse momentum signature using the ATLAS detector in $\sqrt(s)$ = 7 TeV proton-proton collisions., Phys. Lett. B 705 294, doi:10.1016/j.physletb.2011.10.006, arXiv:1106.5327.

AALTONEN T. et al., 2008. Search for large extra dimensions in final states containing one photon or jet and large missing transverse energy produced in p-pbar collisions at $\sqrt{s}$ = 1.96 TeV, Phys. Rev. Lett. 101 181602, arXiv:hep-ex/0807.3132v1.

ABAZOV V.M. et al.,, 2008. Search for Large Extra Dimensions via Single Photon plus Missing Energy Final States at $\sqrt{s}$ = 1.96 TeV, Phys. Rev. Lett. 101 011601

ABBASI R.,2012 IceCube Collaboration, .Multi-year search for dark matter annihilations in the Sun with the AMANDA-II and IceCube detectors., Phys. Rev. D 85 042002.

ALWALL J. et al., 2007. MadGraph/MadEvent v4: The New Web Generation, JHEP 09 028, arXiv:0706.2334.

AN-2009-048, 2009. Parton Distribution Uncertainty Determination within CMSSW, AN-2009-048.

ARKANI-HAMED N., DIMOPOULOS S., and MARC-RUSSELL J.,1998 Stabilization of Sub-Millimeter Dimensions: The New Guise of the Hierarchy Problem hep-th/9809124.

ARKANI-HAMED N., DIMOPOULOS S., DVALI G.,1998 The hierarchy. problem and new dimensions at a millimeter. Phys. Lett. B 429 263

BAYATIAN G.L. et al.,2006 CMS Physics Technical Design Report Volume-I.

BEAUDETTE F. et al., Electron Reconstruction within the Particle Flow Algorithm, CMS Analysis Note AN-10-034.

BEAUDETTE F. et al., Fake missing transverse momentum in the RA2 analysis, CMS Analysis Note AN-10-383.

BEGEMAN, K. G., BROEILS, A. H., SANDERSs, R. H. 1991, Mon. Not. R. astr. Soc., 249, 523

BELTRAN M., HOOPER D., KOLB E. W. et al., 2010 Maverick dark matter at colliders., JHEP 09 037, doi:10.1007/JHEP09 037, arXiv:1002.4137

BENVENUTI A. et al., 1975 Observation of New-Particle Production by High-Energy Neutrinos and Antineutrinos. Phys. Rev. Lett. 34, 419.422.

BERTONE, G., HOOPER D. SILK J.,2005 Particle dark matter: evidence, candidates and constraints. Phys. Rep. 405, 279390.

BERTRAM I. et. al., A recipe for construction of confidence limits, FERMILAB-TM-2104.

BRESSI G., CARUGNO G., ONOFRIO R., and RUOSO G. , 2002. Measurement of the casimir force between parallel metallic surfaces. Physical Review Letters, 88:041804, 2002.

CACCIARI M., SALAM G.P. and SOYEZ G., 2008. The anti-kt jet clustering algorithm, JHEP 0804:063, doi:10.1088/1126-6708/2008/04/063.

CHATRCHYAN S. et al.,2008 The CMS experiment at the CERN LHC.

CMS Analysis Notes AN-10-116, AN-10-345.

CMS Collaboration, 2010. Jet Energy Corrections determination at 7 TeV, CMS Physics Analysis Summary JME-10-010.

CMS Collaboration, 2009. Particle-Flow Event Reconstruction in CMS, CMS Physics Analysis Summary PFT-09-001.

CMS Collaboration, 2010. Performance of muon identification in pp collisions at $\sqrt{s}$=7 TeV, CMS Physics Analysis Summary MUO-10-002.

CMS Collaboration, 2010. Electron reconstruction and identifications at $\sqrt{s}$=7 TeV, CMS Physics Analysis Summary EGM-10-004.

CMS Collaboration, 2010. Measurement of the W !en + jets to Z !e+e + jets ratio in proton-proton collisions at ps=7 TeV, CMS Physics Analysis Summary AN-10-425v3.

CMS Collaboration, 2011. Jet Energy Resolution in CMS at ps = 7 TeV, CMS Physics Analysis Summary JME-10-014.

CMS Collaboration, 2010. Measurements of CMS Luminosity, CMS Physics Analysis Summary EWK-10-004.

CMS Collaboration, 2008. Search for Mono-Jet Final States from ADD Extra Dimensions, CMS Physics Analysis Summary EXO-08-011.

CMS Collaboration, 2009. Search for Mono-Jet Final States from ADD Extra-Dimensions at $\sqrt{s}$=10 TeV, CMS Physics Analysis Summary EXO-09-013.

CMS Collaboration, 2008. The CMS experiment at the CERN LHC, JINST 0803 S08004, doi:10.1088/1748-0221/3/08/S08004.

CMS Collaboration, 2010. Tracking and Primary Vertex Results in First 7 TeV Collisions, CMS Physics Analysis Summary TRK-10-005.

CMS Collaboration, 2010. Tranverse momentum and pseudorapidty distributions of charged hadrons in pp collisions at $\sqrt{s}$=0.9 and 2.36 TeV, JHEP 02 041, doi:10.1007/JHEP02 041.

CMS Collaboration, 2011. Measurements of Inclusive W and Z Cross Sections in pp Collisions at $\sqrt{s}$ = 7 TeV, CMS Physics Analysis Summary JHEP01 080,arXiv:1012.2466.

CMS Collaboration, Search for a heavy gauge boson W0 in the final state with an electron and large missing transverse energy in pp collisions at ps = 7 TeV, arXiv:1012.5945v2.

CMS EXPERIMENT 2008, The CMS experiment at the CERN LHC.

CMS Twiki-1 https://twiki.cern.ch/ twiki/ bin/ view/ CMSPublic/ WorkBookCMSExperiment

CMS Twiki-2 https://twiki.cern.ch/ twiki/ bin/ view/CMS/ ProductionReProcessingSpring10 and https://twiki.cern.ch/ twiki/bin/ view/CMS/ ProductionFall2010

DØ Collaboration, 2004. Search for large extra spatial dimensions in Jets + $E_{\mathrm{T}}^{\mathrm{miss}}$ topologies, DCONF 4400

DELGADO A. and STRASSLER M., 2009. A Simple-Minded Unitarity Constraint and an Application to Unparticles, http:// arxiv.org/abs/0912.2348

DELPHI Collaboration, 2005. Photon Events with Missing Energy in e+e- Collisions at $\sqrt{s}$ = 130 to 209 GeV Eur. Phys. J. C 38 395.

DIENES K.R., DUDAS E., and GHERGHETTA T.. 1998. Extra spacetime dimensions and unification. Physics Letters B, 436:55.

DIENES K.R., DUDAS E., and GHERGHETTA T., 1999. Grand unification at intermediate mass scales through extra dimensions. Nuclear Physics B, 537:47.

DONOGHUE J.F., 1995. Introduction to the Effective Field Theory Description of Gravity. arXiv:gr-qc/9512024v1.

DVALI G. and SHIFMAN M., 1997. Domain walls in strongly coupled theories. Phys.Lett. B, 407:452.

For details, see http://home.thep.lu.se/ torbjorn/ php8135/ Welcome.php

FRIXIONE S., WEBBER B.R., 2002. Matching NLO QCD computations and parton shower simulations, JHEP 0206 029.

GABADADZE G., 2002. ICTP Lectures on Large Extra Dimensions.

GEORGI H., 2007. Unparticle Physics. Phys. Rev. Lett. 98 221601

GIUDICE G.F., RATTAZZI R. and WELLS J.D., 2000. Quantum Gravity and Extra Dimensions at High-Energy Colliders, CERN-TH/98-354 hep-ph/9811291

GRIEST K., KAMIONKOWSKI M.,2000 Supersymmetric dark matter.

GUBSER S.S., KLEBANOV I.R. and TSEYTLIN A.A., 1997. Nucl. Phys. B 499, 217.

HANNESTAD S., RAFFELT G.G., 2001. New Supernova Limit on Large Extra Dimensions: Bounds on Kaluza-Klein Graviton ProductionPhys. Rev. Lett. 87, 051301.

HASHIMOTO A. and KLEBANOV I.R., 1996. Phys. Lett. B 381, 437.

HEISTER A.,ALEPH Collaboration, 2003. Single- and multi-photon production in e+e- collisions at s up to 209 gev. European Physics Journal, 28:1.

HOSKINS J.K., NEWMAN R.D., SPERO R., and SCHULTZ J., 1985. Experimental tests of the gravitational inverse-square law for mass separations from 2 to 105 cm. Phys. Rev. D, 32(12):30843095.

HOUCHE S. et al., Matching parton showers and matrix elements arXiv:hepph/0602031.

INDICO-1, 2010 http://indico.cern.ch/ getFile.py/ access?resId=1 materialId = slidesconfId=102650

JACKIW R. and REBBI C.,1976 Solitons with fermion number 1/2. Phys. Rev. D, 13(12):33983409

J. PUMPLIN J. et al., 2002. New generation of parton distributions with uncertainties from global QCD analysis,JHEP 07 (2002) 012 arXiv:hep-ph/0201195.

JSON file Cert 136033-149442 7TeV Nov4ReReco Collisions10 JSON.txt, for details see https://hypernews.cern.ch/ HyperNews/ CMS/get/ physicsvalidation/ 1025.html

JUNGMAN G., 1994 Neutrinos From Particle Decay in the Sun and Earth. arxiv:9407351

KARG S., KRAMER M. et al, 2010. NLO QCD corrections to graviton production at hadron colliders, Phys. Rev. D81 (2010), arXiv:0911.5095v2.

KLEBANOV I.R., 1997. Nucl. Phys. B 496, 231

KRUTELYOV V., 2008. Searches for large extra dimensions at the tevatron.

LONG J.C., CHAN H.W., and PRICE J.C., 1999. Experimental status of gravitational-strength forces in the subcentimeter regime. Nuclear Physics B, 539:23.

LONG J.C. and Price J.C., 2003. Current short-range tests of the gravitational inverse square law. Comptes Rendus Physique, 4:337.

LYKKEN J., 1996. Phys. Rev. D 54, 3693.

MIJAKOWSKI P., Direct and Indirect Search for Dark Matter 2011.

NASA-1 http://www.nasa.gov/ mission pages/ chandra/ multimedia/ photos08-111.html

NASM http://airandspace.si.edu/ exhibitions/ gal111/ universe/ kiosks/ lensing/ lensing.htm

Particle Data Group Collaboration, 2008. Review of Particle Physics - Section 32.3.1: The Bayesian approach, Phys. Lett. B667 1.

Particle Data Group Collaboration, 2008. Review of Particle Physics - Gauge and Higgs Bosons, Phys. Lett. B667 1.

REID M.J., 1993 The distance to the center of the galaxy. Annu. Rev. Astro. Astrophys. 1993.31:345-372.

SAAB T.,2012 An Introduction to Dark Matter Direct Detection Searches Techniques.

SAKUMA T.,2012 CMS Document 11514-v1.

SAOULIDOU N., ISILDAK B., KOUSOURIS K., RABBERTZ K, 2011. Measurement of the Inclusive Dijet Production Rate, as a Function of the Dijet Invariant Mass, with the CMS Detector in p-p Collisions at ps=7 TeV, CMS Analysis Note AN-10-278.

SJOSTRAND T., MRENNA S. and SKANDS P.Z., 2006. PYTHIA 6.4 Physics and Manual; v6.420, tune D6T, JHEP 05 (2006) 026, arXiv:hep-ph/0603175.

TANAKA T.,2011 Super-Kamiokande Collaboration, .An Indirect Search for WIMPs in the Sun using 3109.6 Days of Upward-going Muons in Super-Kamiokande., Astrophys. J. 742 78.

TAUOLA the library for lepton decay, and KKMC/KORALB/KORALZ, 2001. Nuclear Physics B, Volume 98, Issues 1-3, Pages 96-102, arXiv:hepph/0011305v1.

TAYLOR T.R., VENEZIANO G.. 1988. Strings and d=4. Physics Letters B, 212:147.

The ALEPH DELPHI L3 OPAL 2004. Collaborations and the LEP Exotica Working Group. Combination of lep results on direct searches for large extra dimensions. LEP Exotica WG, 03:1.

The DELPHI Collaboration, 2005. Photon events with missing energy in e+e collisions at $\sqrt{s} = 130$ to 209 gev. European Physical Journal C, 38:395.

The L3 Collaboration and P. Achard. 2004. Single- and multi-photon events with missing energy in e+e- collisions at lep. Physics Letters B, 587:16.

TRIMBLE V., 1987 Existence and nature of dark matter in the universe. Annu. Rev. Astro. Astrophys. 1987.25:425-472.

T. SJOSTRAND T., S. MRENNA S. and SKANDS P.Z., 2008. A Brief Introdcution to PYTHIA 8.1 Comput. Phys. Commun. 178 852, doi:10.1016/j.cpc.2008.01.036.

ZACEK V., 2007 Dark matter. arXiv:0707.0472v1.

CURRICULUM VITAE

Name Surname: Mehmet Vergili

Date of Birth: 05.03.1977

Place of Birth: Adana

Nationality: Turkish

Gender: Male

Marrital Status: Married

Contact: vergili@cern.ch

Education:

PhD, Physics Cukurova University, Adana, Turkey 2012

seacrh for dark matter and large extra dimensions in monojet events in pp collisions at $\sqrt{s} = 7$ TeV

M.S, Physics Cukurova University, Adana, Turkey 2006

Jet Calibration Studies

B.S, Physics, Cukurova University, Adana, Turkey 2001

APPENDIXS

1. APPENDIX-A

1.1 ADD and Dark Matter Models Cross Section and Number of Events

Table 1.1 Signal datasets used for ADD signal, with $\hat{p}_T > 80\,\text{GeV}$ and Tune 4C from PYTHIA8 at LO.

δ	M_D [TeV]	σ [pb]	# Events
2	2	22.37 ± 0.04	53536
2	3	4.456 ± 0.009	54085
2	4	1.411± 0.003	53902
2	5	0.5779± 0.0011	101572
3	1	210.5± 0.5	10676
3	2	9.894 ± 0.052	53719
3	3	1.356 ± 0.005	53090
3	4	0.3241 ± 0.0012	101572
4	1	178.4 ± 0.6	54085
4	2	5.889 ± 0.030	53719
4	3	0.5719 ± 0.0027	106983
4	4	0.1032 ± 0.0005	102528
5	1	169.2 ± 1.0	48910
5	2	4.081 ± 0.018	53719
5	3	0.2928 ± 0.0014	105992
5	4	0.04003 ± 0.00019	102879
6	1	177.5 ± 1.1	10784
6	2	3.107 ± 0.012	52987
6	3	0.1693 ± 0.0008	95726
6	4	0.01778 ± 0.00006	14616

Table 1.2 Signal datasets used for Dark Matter signal, from MADGRAPH at LO.

Model	M_χ [GeV]	σ [pb]	Number of Events
AV-d	0.1	0.402E-7 +/- 3.2e-11	100000
AV-d	1	0.396E-7 +/- 3.1e-11	100000
AV-d	10	0.411E-7 +/- 2.9e-11	100000
AV-d	100	0.289E-7 +/- 2.3e-11	100000
AV-d	200	0.164E-7 +/- 2.4e-11	100000
AV-d	300	0.897E-8 +/- 2.1e-11	100000
AV-d	400	0.476E-8 +/- 2.9e-12	100000
AV-d	700	0.609E-9 +/- 4.0e-13	100000
AV-d	1000	0.600E-10 +/-3.9e-14	100000
AV-u	0.1	0.719E-7 +/- 4.9e-11	100000
AV-u	1	0.719E-7 +/- 5.4e-11	100000
AV-u	10	0.755E-7 +/- 5.3e-11	100000
AV-u	100	0.552E-7 +/- 3.6e-11	100000
AV-u	200	0.333E-7 +/- 3.7e-11	100000
AV-u	300	0.194E-7 +/- 3.9e-11	100000
AV-u	400	0.111E-7 +/- 7.4e-12	100000
AV-u	700	0.192E-8 +/- 1.2e-12	100000
AV-u	1000	0.284E-9 +/- 2.8e-13	100000
V-d	0.1	0.393E-7 +/- 2.4e-13	100000
V-d	1	0.394E-7 +/- 2.7e-11	100000
V-d	10	0.414E-7 +/- 2.8e-11	100000
V-d	100	0.365E-7 +/- 2.0e-11	100000
V-d	200	0.261E-7 +/- 2.0e-11	100000
V-d	300	0.173E-7 +/- 2.0e-11	100000
V-d	400	0.109E-7 +/- 6.2e-12	100000
V-d	700	0.215E-8 +/- 1.1e-12	100000
V-d	1000	0.305E-9 +/- 3.7e-13	100000
V-u	0.1	0.720E-7 +/- 4.5e-11	100000
V-u	1	0.719E-7 +/- 4.6e-11	100000
V-u	10	0.740E-7 +/- 4.6e-11	100000
V-u	100	0.680E-7 +/- 4.6e-11	100000
V-u	200	0.509E-7 +/- 3.3e-11	100000
V-u	300	0.354E-7 +/- 2.1e-11	100000
V-u	400	0.237E-7 +/- 1.1e-11	100000
V-u	700	0.600E-8 +/- 3.0e-12	100000
V-u	1000	0.123E-8 +/- 5.7e-13	100000

2. APPENDIX-B

2.1 Monte Carlo Background Simulation Samples

Table 2.1 Standard Model Monte Carlo simulation samples. Each sample is from "Summer11" production and uses PYTHIA6 for showering. The cross-sections quoted are at LO for QCD and LO/NLO for the other processes.

Dataset	Details	LO σ [fb]	NLO σ [fb]
$Z_{\nu\bar{\nu}} + jets, 50 > H_T > 100$	MADGRAPH	0.3095	0.4124
$Z_{\nu\bar{\nu}} + jets, 100 > H_T > 200$	MADGRAPH	0.1252	0.1668
$Z_{\nu\bar{\nu}} + jets, H_T > 200$	MADGRAPH	0.03292	0.04386
$W_{l^{\pm}\nu} + jets$	MADGRAPH	24.640	31.634
$Z_{l^+l^-} + jets$	MADGRAPH	2.321	3.093
$t\bar{t}$	MADGRAPH	0.121	0.203
QCD, $170 > H_{\mathrm{T}} > 300$	PYTHIA	0.255	
QCD, $300 > H_{\mathrm{T}} > 470$	PYTHIA	5.495	
QCD, $470 > H_{\mathrm{T}} > 600$	PYTHIA	56.82	
QCD, $600 > H_{\mathrm{T}} > 800$	PYTHIA	273.0	
QCD, $800 > H_{\mathrm{T}} > 1000$	PYTHIA	2193	
QCD, $1000 > H_{\mathrm{T}} > 1400$	PYTHIA	6302	
QCD, $1400 > H_{\mathrm{T}} > 1800$	PYTHIA	202042	
QCD, $1800 > H_{\mathrm{T}} > \infty$	PYTHIA	818355	

3. APPENDIX-C

3.1 Optimisation of MET Cut for Limit Setting

Table 3.1 Optimisation of $E_{\mathrm{T}}^{\mathrm{miss}}$ cut for various ADD models limits in pb^{-1}.

$E_{\mathrm{T}}^{\mathrm{miss}}$ GeV	$M_{\mathrm{D}} = 4, \delta = 2$	$M_{\mathrm{D}} = 2, \delta = 3$
200	3.89	3.90
250	2.59	2.21
300	1.71	1.37
350	1.86	1.38
400	1.92	1.39

Table 3.2 Optimisation of $E_{\mathrm{T}}^{\mathrm{miss}}$ cut for various DM models limits in pb^{-1}.

$E_{\mathrm{T}}^{\mathrm{miss}}$ GeV	Avd 10	AVd 400	AVu 400	Vd 400	Vu 400
200	4.03	3.11	2.93	3.33	3.02
225	3.19	2.36	1.94	2.39	2.17
250	2.61	1.87	1.66	1.96	1.72
275	2.18	1.51	1.30	1.59	1.38
300	1.86	1.26	1.06	1.32	1.13
325	1.86	1.23	1.02	1.30	1.08
350	1.88	1.20	0.95	1.26	1.02
375	2.03	1.23	0.98	1.35	1.03
400	2.21	1.25	0.97	1.38	1.01
425	2.38	1.32	1.00	1.47	1.05
450	2.47	1.32	0.97	1.44	1.05
475	2.51	1.33	0.94	1.46	1.01
500	2.72	1.36	0.94	1.52	1.00
525	2.90	1.52	1.01	1.62	1.06
550	3.01	1.58	1.01	1.61	1.04
575	3.06	1.58	1.04	1.60	1.03

4. APPENDIX-D

4.1 $W_{l^{\pm}\nu} + jets$ Estimation

Table 4.1 Estimation of the remaining $W_{l^{\pm}\nu} + jets$ background from the lost electron and muon contributions.

	$E_T^{miss} > 200$	$E_T^{miss} > 250$	$E_T^{miss} > 300$	$E_T^{miss} > 350$	$E_T^{miss} > 400$
N_{obs}	8666	3012	1179	531	261
N_{bgd}	616.2	205.8	78.1	31.3	14.9
A'	0.786	0.824	0.853	0.873	0.890
ε'	0.435	0.415	0.429	0.450	0.414
N_{tot}	23556	8219	3009	1271	667
A	0.851	0.878	0.906	0.928	0.938
ε	0.972	0.980	0.981	0.975	0.969
$N^{\mu}_{!A}$	3168.4	835.4	238.2	84.0	35.4
$N^{\mu}_{!\varepsilon}$	587.4	153.7	45.2	17.4	7.2
$N_{lost\mu}$	3755.7	989.0	283.5	101.4	42.6
A^e	0.509	0.476	0.475	0.495	0.518
ε^e	0.546	0.546	0.555	0.975	0.507
$N^{e}_{!A}$	2571.5	748.9	238.1	88.6	39.3
$N^{e}_{!\varepsilon}$	1272.3	322.7	105.9	45.3	18.3
N_{loste}	3843.8	1071.6	344.0	133.9	57.6
$N_{\mathrm{hadronic}\ \tau}$	3807.6	1080.1	353.7	145.3	65.2
$N_{W_{l^{\pm}\nu}+jets}$	11407	3141	981	381	165
$N_{W_{l^{\pm}\nu}+jets}$ (after TIV)	9513	2619	812	310	134
Prediction from $W_{l^{\pm}\nu} + jets$ MC	9047.7	2759.5	904.7	338.5	138.5